Active Electronic Loads for Radiometric Calibration

Von der Fakultät für Informatik, Elektrotechnik und Informationstechnik der Universität Stuttgart zur Erlangung der Würde eines Doktor-Ingenieurs (Dr.-Ing.) genehmigte Abhandlung

Vorgelegt von

Ernst Weissbrodt

geboren in Moskau, Russland

Hauptberichter:	**Prof. Dr. Ingmar Kallfass**
Mitberichter:	**Prof. Dr. Gilles Dambrine**

Tag der mündlichen Prüfung: 06.12.2016

Institut für Robuste Leistungshalbleitersysteme der Universität Stuttgart

2017

To my parents

Executive Summary

Although radiometer systems are widely applied in very different fields, they all have one important requirement in common: They require a thorough radiometric calibration. Various conventional calibration references are well established, but their bulkiness, high power consumption, and complexity are limiting the expanding fields of application. Since novel industrial applications such as passive millimeter-wave imaging emerge, the requirements for calibration references have increased drastically. But also in scientific fields like radio astronomy, cosmology or environmental monitoring, modern remote sensing radiometers do not rely only on conventional references anymore.
In this work, millimeter-wave monolithic integrated circuits (MMICs) based on metamorphic high electron mobility transistors (mHEMT) were designed to be used as active electronic loads for radiometric calibration. These novel references have not only the outstanding property, that they can be directly integrated on chip-level into the radiometer front-end, but also, that they can exhibit cold as well as hot reference noise temperatures. Since this is achieved without any physical cooling or heating, the power consumption is notably reduced. By monolithic integration of field effect transistor (FET) switches, theses multiple references can internally be routed to the receiver input without any mechanical wear. As a result, laborious external references can be omitted and the repetition rate of the calibration procedure increased, which results in a higher radiometric accuracy and allows a more compact and cost-effective design of modern radiometer systems. This work presents the first radiometric calibration front-end that allows to internally switch between active electronic cold and active electronic hot loads, as well as a passive ambient load. All components are integrated on a single MMIC, and a patent was granted for this innovation.
To predict the achievable noise temperatures of active cold loads (ACLs), different simulation approaches were previously published. This work evaluates and adapts these existing approaches to design and manufacture several W-band loads. But the required design-flow was found to be very time-consuming because multiple iterations are necessary to successively design and optimize the input- and output matching networks, and to finally achieve the desired low noise temperature. Therefore, a novel simulation approach is introduced that makes efficiently use of modern optimization algorithms and the very accurate model library of the mHEMT technology and the passive structures. With this novel simulation method, the first active hot loads (AHLs) were designed as well as state-of-the-art ACLs up to $140\,\mathrm{GHz}$.
However, the characterization of low-noise one-port devices is particularly challenging, especially at such high frequencies. Hence, a substantial part of this work is to investigate the reliability of different noise measurement setups and the repeatability of noise temperature results. Dedicated setups in W- and D-band are used to characterize all manufactured active loads and some selected results are cross-checked by measuring the same circuits with independently designed measurement systems of other research facilities. The discrepant results are discussed, concluding that high variations in measured one-port noise temperature

do not allow to rely on one single measurement setup. At the same time, this thorough investigation and comparison permits to establish an accuracy range within which the results of the manufactured active electronic loads are reliable, whereas other previously published ACLs are typically only measured with one measurement setup.

Zusammenfassung

Obwohl Radiometer Systeme in unterschiedlichsten Anwendungsgebieten weit verbreitet sind, haben alle eine wichtige gemeinsame Anforderung: Sie benötigen eine sorgfältige radiometrische Kalibration. Verschiedene konventionelle Kalibrationsreferenzen sind zwar bewährt, doch ihre Sperrigkeit, Komplexität und die hohe Leistungsaufnahme schränken die sich stetig erweiternden Anwendungsmöglichkeiten ein. Seit neuartige industrielle Anwendungen wie passive Millimeterwellen-Kameras z.B. bei Sicherheitskontrollen aufkommen, haben sich auch die Anforderungen an die notwenigen Kalibrationsreferenzen drastisch erhöht. Aber auch in wissenschaftlichen Anwendungsgebieten wie der Radioastronomie, der Kosmologie oder der Umweltbeobachtung beschränken sich moderne Fernerkundungs-Radiometer nicht mehr nur auf konventionelle Kalibrationsreferenzen.

Im Rahmen dieser Arbeit wurden monolithisch integrierte Millimeterwellen-Schaltkreise (MMICs), basierend auf einer metamorphen Transistor-Technologie mit hoher Elektronenbeweglichkeit (mHEMT) entwickelt, die als aktive elektronische Referenz-Last zur radiometrischen Kalibration dienen. Diese neuartigen Referenz-Lasten haben nicht nur die herausragende Eigenschaft direkt auf Halbleiter-Bauteilebene mit dem Radiometereingang integriert werden zu können, sondern können außerdem sowohl niedrige („kalte“) als auch hohe („heiße“) Referenz-Rauschtemperaturen erzeugen. Da dies ohne physikalische Kühlung oder Erhitzung erreicht wird, ist die Leistungsaufnahme besonders gering. Durch die monolithische Integration von Feldeffekttransistor-Schaltern können diese Referenz-Lasten elektronisch intern auf den Empfängereingang geschaltet werden, ohne dass mechanische Schalt- oder Bewegungsvorgänge notwendig sind. Infolgedessen sind aufwändige externe Referenzen nicht mehr zwingend notwendig, so dass ein kompaktes, kostengünstiges und modernes Radiometer-System ermöglicht wird. Außerdem kann die Wiederholrate der Kalibrationsprozedur erhöht werden, was sich in einer erhöhten radiometrischen Genauigkeit auswirkt. Diese Arbeit präsentiert die erste radiometrische Kalibrationseinrichtung, die es ermöglicht intern zwischen aktiven elektronischen kalten und heißen Referenz-Lasten, sowie einer passiven Referenz-Last auf Umgebungstemperatur umzuschalten. Alle notwendigen Bauteile sind monolithisch auf einem Millimeterwellen-Schaltkreis integriert, worauf ein Patent erteilt wurde.

Um die erreichbare Rauschtemperatur aktiver kalter Referenzlasten vorherzusagen, wurden in der Vergangenheit verschiedene Ansätze veröffentlicht. In dieser Arbeit wurden diese Ansätze bewertet und angewandt um mehrere Referenzlasten im W-Band zu entwickeln und herzustellen. Der notwendige Design-Flow stellte sich jedoch als sehr zeitaufwändig heraus, da mehrere Iterationen notwendig sind, um sukzessiv die Eingangs- und Ausgangs-Anpassnetzwerke zu entwerfen und zu optimieren, um letztlich die gewünschte Rauschtemperatur zu erreichen. Daher wurde im Rahmen dieser Arbeit eine neuartige Simulationsmethode eingeführt, die sich die Möglichkeiten moderner Optimierungs-Algorithmen und sehr genauer Modell-Bibliotheken der verwendeten Halbleitertechnologie und der passiven Komponenten zu Nutze macht. Mit dieser Methode wurden die erste aktive heiße Referenzlast, sowie eine den neusten Stand der Technik definierende kalte Referenzlast bei $140\,\mathrm{GHz}$ entwickelt.

Allerdings ist die messtechnische Charakterisierung eines so rauscharmen Eintor-Bauteils, wie es die kalte Referenzlast ist, besonders herausfordernd - vor allem bei solch hohen Frequenzen. Daher besteht ein wesentlicher Teil dieser Arbeit darin, die Zuverlässigkeit von Rauschmess-Einrichtungen und die Reproduzierbarkeit von Rauschtemperatur-Ergebnissen zu untersuchen. Hierfür wurden spezielle Rauschmessplätze im W-Band und D-Band entworfen und zunächst sämtliche Schaltungen damit charakterisiert. Anschließend wurden ausgewählte Schaltungen und Module zu anderen Forschungseinrichtungen geschickt, wo sie mit deren unabhängig entworfenen Rauschmess-Einrichtungen untersucht wurden. Die diskrepanten Ergebnisse lassen darauf schließen, dass die starke Variation der gemessenen Rauschtemperaturen es nicht erlaubt, diese mit nur einem Messsystem zu bestimmen. Gleichzeitig jedoch, ermöglichte der Vergleich der Ergebnisse verschiedener Rauschmess-Einrichtungen, eine Genauigkeitsspanne zu bestimmen innerhalb welcher die Ergebnisse der in dieser Arbeit entwickelten aktiven elektronischen Referenzlasten aussagekräftig und zuverlässig sind. Während in anderen Publikationen typischerweise lediglich ein Messsystem zum Einsatz kommt.

Contents

Symbols

B	bandwidth
B_n	noise bandwidth
c	speed of light
Δf	bandwidth
ΔG	gain fluctuation
ΔT	radiometric resolution
ΔT_C	calibration noise contribution to radiometric resolution
ΔT_G	contribution of gain fluctuations to radiometric resolution
ΔT_S	system noise contribution to radiometric resolution
F	noise factor
f	frequency
$\frac{1}{f}$	flicker noise
F_{min}	minimum noise figure
F_{sys}	system noise figure
f_T	transit frequency
Γ	reflection coefficient
Γ_1	reflection coefficient at source terminal
Γ_2	reflection coefficient at load terminal
Γ_{in}	reflection coefficient at transistor input
Γ_L	load reflection coefficient
Γ_{opt}	source reflection coefficient for minimum noise
Γ_{out}	reflection coefficient at transistor output
Γ_S	source reflection coefficient
G	gain
G_a	available gain
G_{ij}	available power gains of transistor
$G_{ij,ti}$	terminal invariant gains
G_{opt}	conductance for minimum noise
$g_{m,max}$	maximum extrinsic transconductance
G_{tot}	total noise conductance
h	Planck constant
I_{cor}	noise current correlation matrix
I_d	drain current
i_{tot}	equivalent noise current of an otherwise noiseless device
k	Boltzmann constant

L_A	ohmic losses of the antenna and the antenna feed
L_f	spectral brightness density
L_{lin}	linear loss
μ_0	electron mobility
N	number of calibrations
N_a	added noise
n_e	electron density
N_i	input noise power
N_o	output noise power
NF_{min}	minimum noise figure for optimum reflection coefficient
P	power
R_n	noise resistance
R_{tot}	total noise resistance
S	scattering parameter matrix
S_i	input signal power
S_o	output signal power
S_{opt}	scattering parameter for minimum noise
τ_C	calibration integration time
τ_S	scene integration time
T_0	defined temperature of $290\,\mathrm{K}$
T_1	noise temperature at source terminal
T_2	noise temperature at load terminal
T_A	antenna temperature
T_a	alternative noise parameter
T_B	brightness temperature
T_b	alternative noise parameter
T_c	cold reference temperature
T_h	hot reference temperature
T_k	alternative noise parameter
T_L	load terminal
T_n	noise temperature
T_{phys}	physical temperature
T_{Rec}	receiver noise temperature
T'_{Rec}	receiver noise temperature at the antenna input reference plane
T'_{Ref}	reference load noise temperature at the antenna input reference plane
T_S	source terminal
T_{s1}	generated noise temperature at active cold load output
$T_{s1,limit}$	theoretical lower limit of noise temperature at transistor output
T_{Sys}	system noise temperature
V_g	gate voltage
V_d	drain voltage
V_{sw}	switch voltage
Y	admittance parameter matrix
Z	impedance parameter matrix

Abbreviations

2DEG	Two-Dimensional Electron Gas
ABCS	Antimonide Based Compound Semiconductor
ACL	Active Cold Load
ACSS	Active Calibration Sub-System
ADS	Advanced Design System by Keysight Technologies
AHCL	Active Hot-Cold Load
AHL	Active Hot Load
AWVR	Advanced Water Vapor Radiometer
BJT	Bipolar Junction Transistor
CAD	Computer Aided Design
CAS	Calibration Subsystem
CBR	Cosmic Background Radiation
CMB	Cosmic Microwave Background
COBE	Cosmic Background Explorer
DC	Direct Current
DLR	National Aeronautics and Space Research Centre
DSP	Digital Signal Processor
DUT	Device under Test
ENR	Excess Noise Ratio
EPW	EUMETSAT Polar System
ESA	European Space Agency
ESTEC	European Space Research and Technology Centre
FET	Field Effect Transistor
FOM	Figure of Merit
GaAs	Gallium Arsenide
GCPW	Grounded Coplanar Waveguide
HAMSR	High-Altitude MMIC Sounding Radiometer
HBT	Heterojunction Bipolar Transistor
HEMT	High Electron Mobility Transistor
HF	High Frequency
HSB	Humidity Sounder for Brazil
IAF	Fraunhofer Institute for Applied Solid-State Physics
IEC	International Electrotechnical Commission
IMN	Input Matching Network
In	Indium

InAlAs	Indium Aluminum Arsenide
InGaAs	Indium Gallium Arsenide
InP	Indium Phosphide
ISO	International Organization for Standardization
ISS	Impedance Standard Substrate
JMR	Jason Microwave Radiometer
JUICE	Jupiter Icy Moons Explorer
LN	Liquid Nitrogen
LNA	Low-Noise Amplifier
LO	Local Oscillator
MBE	Molecular Beam Epitaxy
MEMS	Microelectromechanical System
MESFET	Metal-Semiconductor Field Effect Transistor
mHEMT	Metamorphic High Electron Mobility Transistor
MIM	Metal-Insulator-Metal
MIRAS	Microwave Imaging Radiometer using Aperture Synthesis
ML	Matched Load
MMIC	Millimeter-Wave Monolithic Integrated Circuit
MMW	Millimeter-Wave
MSMR	Multifrequency Scanning Microwave Radiometer
MWR	Microwave Radiometer
NASA	National Aeronautics and Space Administration
ND	Noise Diode
NF	Noise Figure
NFA	Noise Figure Analyzer
NiCr	Nickel-Chromium
NIR	Noise Injection Radiometer
NIST	National Institute of Standards and Technology
NTC	Negative Temperature Coefficient
OMN	Output Matching Network
PCB	Printed Circuit Board
pHEMT	Pseudomorphic High Electron Mobility Transistor
PIN	Semiconductor with a p-type / intrinsic / n-type region
PMMW	Passive Millimeter-Wave
PSR	Polarimetric Scanning Radiometer
PTB	Physikalisch-Technische Bundesanstalt
RADAR	Radio Detection and Ranging
RF	Radio Frequency
RPG	Radiometer Physics GmbH
S-parameter	Scattering Parameter
SCFE	Switching Calibration Front-End
SiGe	Silicon Germanium
SMB	Subminiature Type B connector
SMMR	Scanning Multichannel Microwave Radiometer
SMOS	Soil Moisture and Ocean Salinity

SNR	Signal-to-Noise Ratio
SP3T	Single-Pole Triple-Throw
SP5T	Single-Pole Five-Throw
SPDT	Single-Pole Double-Throw
SPST	Single-Pole Single-Throw
SWI	Submillimeter Wave Instrument
TMR	Topex/Poseidon Microwave Radiometer
UAV	Unmanned Aerial Vehicle
VNA	Vector Network Analyzer
VSWR	Voltage Standing Wave Ratio
VTS	Variable Temperature Source
WMAP	Wilkinson Microwave Anisotropy Probe

1 Introduction

1.1 Radiometer Systems

A radiometer is a device for measuring the electromagnetic radiation of a noise-like character in a certain frequency range. In the context of this work only *microwave* and *millimeter-wave* (MMW) radiometers will be considered. At these frequencies, radiometer systems are similar to receiver architectures known from communication applications. But while in communications, the information is contained in a modulated and coded signal on a narrow-band carrier with a distinct signal-to-noise-ratio (SNR), in radiometry it is the noise itself which is the signal of interest [1]. This, however, demands very sensitive receivers, because the signal power level e.g. in radio astronomy receivers is in the order of $10^{-15} - 10^{-20}$ W and does not differ in its statistical properties from the noise originating in the receiver itself or from the background noise [2].
There exists comprehensive literature on radiometry and radiometer systems [3], [4], [5], where the physical fundamentals are explained and the assets and drawbacks of different architectures are discussed. Therefore, this work will not elaborate on these fundamentals in general, but only where it is necessary in the context of this work.

1.2 Application Area of Radiometer Systems

The physical quantities measured by radiometers and its terminology will be introduced in the next chapter, whereas this section gives an overview of the application area of such systems.
The key feature of a radiometer is that it is a *passive* instrument, which means that - unlike RADAR[1] - it does not emit radiation of any kind. Instead, it *collects* the electromagnetic radiation of objects, which can be a combination of naturally emitted, scattered and penetrated radiation[2].
Depending on the application, objects of interest can be anything between an oscillating molecule in our atmosphere and a remote galaxy in space. Similar to the observation of objects with optical telescopes, this allows to detect objects and to derive some of their physical properties from a distance by measuring the amount or characteristic of the radiation. This is called *remote sensing*.
In general, remote sensing radiometers can be divided into ground-based and space-based instruments. Examples for the former are zenith-pointed radiometers, observing earth's atmosphere for meteorological and environmental sensing [6], [7]. Another example are radiometers used in astronomy, often arranged into large arrays, looking into deep space to detect

[1] RADAR: RAdio Detection And Ranging
[2] In radiometry the black body model is more common, which means that technically speaking a body does not scatter radiation from other sources, but absorbs and emits it partially

distant stars and galaxies [8]. Even in cosmology this technique already played an important role: for the detection and measurement of the cosmic background radiation (CBR) with a highly sensitive ground-based radiometer, Arno Penzias and Robert Wilson were awarded the Nobel prize for physics in 1978 [9]. Space-based radiometers allow to take this one step further. Instruments on board of satellites can observe earth's surface and atmosphere on a large scale and the gathered data is used in meteorology, climatology, oceanography, glaciology, just to name a few applications in the field of geoscience. For astronomic applications satellite-based systems have the advantage that the observed extraterrestrial radiation is not attenuated or otherwise influenced by earth's atmosphere [10]. Also, radiometers are common instruments on board of space probes, exploring other planetary bodies while orbiting or flying by.

An emerging field which is not referred to as remote sensing but still allows contact-free detection of objects, is the application in security-screening portals and stand-off detection at check-points [11], [12], [13]. This field is in fierce competition with RADAR technology and the advantages and disadvantages of both are intensively debated in the scientific community. In addition to technical arguments, radiometry with its passive nature benefits from superior social acceptance, since it does not expose the human body to electromagnetic radiation. The goal to detect concealed dangerous objects from a distance is based on the principle that both - the human body and the carried objects - emit natural radiation which penetrates fabric such as clothing or packaging. The contrast of different amounts of measured radiation generates an image in which suspicious objects can be identified. This is called *passive millimeter-wave imaging* (PMMW) [14], [15], [16], [17]. The quality of the image substantially depends on the radiometric resolution of the system, i.e. the smallest difference in radiation which can still be distinguished by the radiometer. To improve the radiometric resolution and accuracy, a crucial procedure before and during operation is the calibration of the radiometer.

1.3 Calibration of Radiometers

The terms "calibration" and "standard" have to be used with particular caution! In metrology[3], the definition of calibration involves national and international *standards*, whereas the active loads presented later on in this work are merely *references*, not claiming to be standards in the scientific sense. (Primary) standards are objects, systems or experiments defined by national metrological authorities like the National Institute of Standards and Technology (NIST) in the United States or the Physikalisch-Technische Bundesanstalt (PTB) in Germany. They are used to calibrate instruments (or secondary standards) in specified laboratory conditions with the goal that afterwards the instrument will return a *measurement result* instead of just some output quantity. The formal definitions of measurement, calibration and standard can be found in the *International vocabulary of metrology* [18], a document published by a joint committee of institutions like the International Organization for Standardization (ISO) or the International Electrotechnical Commission (IEC).
In this work the term calibration will be used much less restrictively. For example, the adjustment of the radiometer to an instrumental drift (a change over time), as well as the use of references for this repeated procedure (instead of standards) will also be referred to

[3]Metrology is the science of measurement - not to be confused with meteorology, the scientific study of physical and chemical effects in earth's atmosphere.

as *calibration*.

To explain the basic procedure of radiometer calibration, a Dicke radiometer [1] as shown in Figure 1.1(a) is considered. Its antenna receives a certain amount of radiation and returns a voltage at the output of its detector which can easily be digitized and treated by a digital signal processor (DSP). As previously mentioned, the received radiation can not be distinguished from the radiometer inherent noise, so the displayed result is the sum of the received radiation and the system noise. To overcome this, the radiometer input is switched from the antenna to a termination (a passive impedance-matched load), which allows to determine the system-noise. Subtracting this from the previously measured total power returns a voltage corresponding to the received radiation. Since this procedure theoretically eliminates the varying noise contribution of the instrument itself and allows to compare independent observations, it is referred to as *relative* calibration. At this point, however, one still cannot conclude the *absolute* amount of received radiation. For that it is necessary to observe at least two known sources of radiation and assign the voltage values to the respective known amount of radiation. Assuming a linear behavior of the radiometer, two references are sufficient to produce a generic calibration-curve, which in this case is a straight line thru the two reference points as can be seen in Figure 1.1(b). This procedure is thus called *two-point calibration* or also *absolute* calibration. It is only now, by the unambiguous assignment of input radiation to output voltage with the calibration-curve, that the calibrated radiometer can *measure* the received radiation in terms of quantity and unit.

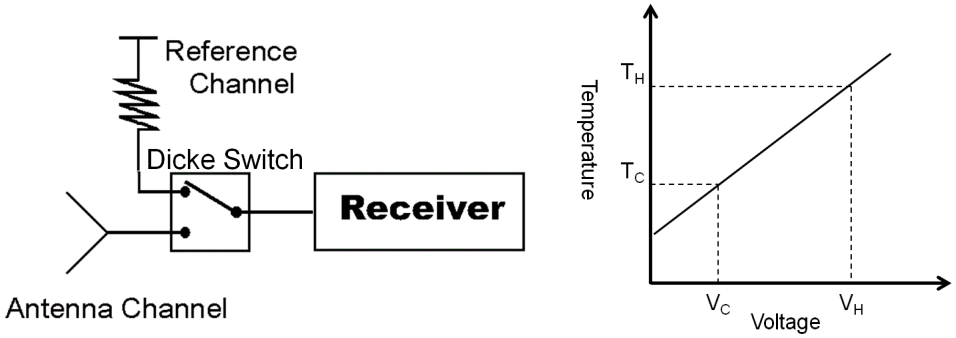

(a) Dicke radiometer (b) Two-point calibration

Figure 1.1: Calibration of radiometers.

1.4 Motivation and Outline

The previous sections have shown, that radiometric calibration is essential for operating radiometer systems in any field. While the principle procedure is straightforward, real radiometers do not always operate linearly and the choice and number of suitable references influences the measurement range and accuracy. To reduce interpolation and extrapolation errors, multiple references are beneficial. Furthermore, references whose levels are in the vicinity of the expected targets improve the radiometric resolution, as will be explained in

Section 2.3.
The highest requirements for the *accuracy* of the radiometric calibration are still in the field of scientific applications such as radio astronomy or environmental monitoring. The latter is particularly important for climate change observations, weather predictions, and early warning systems for disaster risk reduction. In the previously mentioned emerging field of PMMW imaging in industrial and commercial applications, the main focus is on the *repetition rate* of the calibration procedure. Novel techniques generate real-time images, which demand a calibration and processing of the data in video-rate. Also, high resolution multi-channel systems demand calibration references for the pixel normalization. These applications necessitate not only compact and reliable references, but especially a front-end to switch extremely fast between the references and several signal channels. Since these applications target a mass market, it is needless to say, that such references and switches must be cost-effective, very compact and lightweight, and require low maintenance and low power consumption. Except for the cost, these are the same factors that are critical in satellite missions. The lack of such references motivated this work, since conventional references up to now are still bulky and complex and mostly limited to laboratory or scientific instruments. The novel active loads with integrated switches, presented in this work, however, meet all of the above mentioned requirements.
After presenting the state of the art of conventional calibration references and switches, the active electronic loads will be introduced in the next chapter. Chapter 3 will guide the reader thru the entire designing process of the developed loads, from choosing the technology and simulating the noise temperature, to the description of the designed circuits and layouts. Furthermore, a novel noise temperature simulation method, that significantly simplifies the design-flow will be introduced in that chapter. The challenging task of characterizing the resulting circuits will be the topic of chapter 4, where different dedicated noise measurement setups will be elaborated and the critical components will be discussed. Finally, Chapter 5 and Chapter 6 will present and discuss the results of the W-band and D-band circuits, respectively, before Chapter 7 ends this work with a conclusion.

2 State of the Art

This chapter will introduce the theoretical basics necessary for the understanding and further discussion of this work. After presenting the conventional loads in general, it will mainly focus on the advantages of active electronic loads in space-based instruments, since part of this work was supported by the European Space Agency (ESA), specifically for the investigation of Active Cold Loads in Post-EPS[1] / MetOp-SG[2] mission context [19], [20]. Furthermore, an overview of switches will be given, which are essential parts to integrate internal calibration references in a radiometer front-end.

2.1 Theoretical Background of Radiometry

For the sake of consistency, the *Recommended Terminology for Microwave Radiometry*, as described in [21] by the NIST will be used, unless otherwise noted.
All matter above a physical temperature of $0\,\mathrm{K}$ (*absolute zero*) emits natural thermal electromagnetic radiation, which is caused by atomic and molecular state transitions. It is a broadband non-polarized non-coherent random radiation (noise). To describe this physical phenomenon, the theoretical model of a *black body* was introduced in 1860 by Gustav Kirchhoff. It is a perfect absorber and emits the radiation with a spectral brightness density L_f described by the Planck formula

$$L_f = \frac{2hf^3}{c^2}\,\frac{1}{e^{hf/kT}-1} \tag{2.1}$$

where c is the speed of light, f is the frequency, h and k are the Planck and Boltzmann constants respectively and T is the temperature. In the microwave regime, where $hf/kT \ll 1$ (which is considered for frequencies below $300\,\mathrm{GHz}$), this formula can be approximated with the Rayleigh-Jeans formula

$$L_f \approx \frac{2kf^2}{c^2}\,T \tag{2.2}$$

which results in a linear relationship between the spectral brightness density and the physical temperature. This, and the fact that the physical temperature of the observed scene is typically the quantity of interest in microwave remote sensing, leads to the common use of the term *brightness temperature* T_B, which in theory is only valid for the black body [22]. Within the Rayleigh-Jeans limit, the microwave power received by a radiometer is $P = kBT_B$, where B is the bandwidth of the radiometer. Because of its analogy to the *Johnson noise* (thermal noise) generated in an electrical resistor, the physical temperature of a resistor T_{phys} which would deliver the same power to the radiometer as the received brightness, is

[1] EPS: EUMETSAT Polar System, EUMETSAT: European Organisation for the Exploitation of Meteorological Satellites
[2] MetOp-SG: MetOp Second Generation, the space segment of the Post-EPS

called *noise temperature* T_n. Again, in the microwave regime the approximation $T_{phys} \approx T_n$ is valid [21]. Since this term obviously describes a quantity *inside* the radiometer, where every component adds noise, it is mandatory to always refer to a *reference plane* within the microwave circuit or system when using this term.
Before explaining the difference between internal and external references in the next section, it is important to understand, that the interface between *outside* and *inside* the radiometer - the antenna - also contributes to the measured noise temperature, just like any other component within the system. At its aperture (which in radiometry is always the antenna *input*) it receives the incident brightness temperature T_B, weighted by its directivity pattern. At its *output* it delivers the noise received at its aperture, attenuated by its ohmic efficiency *and* the thermal noise added by its own ohmic losses, depending on its physical temperature. This emphasizes the importance of defining reference planes and will be further discussed in Chapter 4.

2.2 Conventional Calibration References

2.2.1 Passive Loads

After the preceding explanations, two possible references for calibration become evident, because their physical temperature is easily determined and interrelated to brightness temperature:

- An object outside the radiometer and its antenna which has properties *similar* to a black body
- An impedance-matched resistive load within the radiometer.

These two generic examples at the same time classify typical references into *external* and *internal* calibration types. A practical example of the first type would be a microwave absorbing material just like used in anechoic chambers. Similar to the antenna which transforms the characteristic impedance of the waveguide to the free space impedance, the typically pyramidal form of the microwave absorber transforms the free space impedance of the electromagnetic wave into an ideally fully resistive load. Hence as much as possible energy of the incident wave is transformed into heat within the material. In reverse, by knowing the physical temperature of the absorber and accepting all the previously discussed restrictions, the emitted radiation of the absorber can be used for radiometer calibration. This method will also be used and further discussed in Chapter 4. Such an absorber is sometimes referred to as an *artificial black body*. In practical application, microwave absorber is either cooled by liquid gases like nitrogen or helium or heated to have *cold* and *hot* calibration targets respectively.
For an internal impedance-matched resistive load the relation between physical temperature and noise temperature is straightforward. But again, the return loss of the resistor is the crucial parameter just as for the absorber. If it is not "perfectly" matched to the characteristic impedance of its surrounding electrical network, the emitted noise temperature will not equal its physical temperature.

2.2.2 Targets with Known Brightness Temperature

Further external references can be targets whose brightness temperatures have been previously exactly measured and which are known to be constant for the duration of the mission. Especially for space-based instruments, such targets can be for example the sun or the *cold sky*. For the latter, either the whole satellite, the antenna of the radiometer or a reflective mirror are oriented towards a region in space which is known to have few natural radiation sources. Hence, measuring the previously mentioned, very accurately known background radiation of approximately $2.7\,\mathrm{K}$ [23]. This, however, necessitates orbital maneuvers of the satellite or moving mechanical parts at the instrument and is critical in terms of time consumption, mechanical wear, and reliability. For ground-based instruments, another external calibration routine can be performed: During the *tipping-curve* calibration the radiometer points towards the atmosphere at different zenith angles, measuring at frequencies where the opacity of the atmosphere is low. This method relies on the known relationship between the tipping angles of the radiometer and the atmospheric opacity at those angles [24], [25].

The previously described calibration methods with external targets are accurate and well established, but are limiting the speed of calibration and reducing system sensitivity because the calibration time goes at the expense of integration time (while observing the target). Additional complex mechanics are necessary and are increasing mass and size of the radiometer system. Orbital maneuvers consume auxiliary propellant. Furthermore, liquid gases for cooling and additional power for heating the cold and hot calibration targets respectively need to be held available. These factors are especially a disadvantage for air- or space-based instruments, where payload and power consumption are critical parameters. This is why in recent years, the feasibility of internal calibration targets for future satellite missions is investigated [26]. In addition to the associated cost savings and the reduction of vulnerable mechanic components, they promise performance improvements because internal calibration can typically be performed faster and more frequently. This increases observation time and reduces rapid gain fluctuations. Furthermore, internal targets can be better shielded against influence from external radiation. Possible internal references can for example be the previously mentioned passive matched load or a noise diode, which is described in the next paragraph.

2.2.3 Noise Diodes

A noise diode is an active internal calibration target, providing a hot calibration point if the level of excess noise is known. In general avalanche diodes are used, which are small, reliable and relatively stable. However, their performance is frequency dependent and while they exhibit an excess noise ratio (ENR) of $20-35\,\mathrm{dB}$ at frequencies below $100\,\mathrm{GHz}$, their output noise level degrades to below $10\,\mathrm{dB}$ for higher frequencies. Nevertheless, their output power level typically exceeds the dynamic range of the highly sensitive radiometers. This leads to the mandatory use of additional attenuators or intentionally lossy couplers when routing the signal to the radiometer. Furthermore, since the power level of the reference noise diode is higher than the one of the target by several orders of magnitudes, this approach necessarily leads to high extrapolation errors. In any case, it is preferable to have reference targets with

noise temperatures, that encompass the expected dynamic range of the observed targets, which is explained in the next section.

2.3 Active Electronic Loads

Active Electronic Loads are novel devices, typically consisting of a transistor with surrounding circuitry, which can also be used as internal calibration references. Hot loads function similar to noise diodes, generating a high noise level that results in a noise temperature far above the measurement range. Contrary to noise diodes, however, the output power level is bias dependent and allows to generate several different warm/hot reference levels. This facilitates to adapt the reference level to the dynamic range of the radiometer. In this work these hot loads will be referred to as *Active Hot Loads* (AHL). Previous thorough characterization of the load and a high stability are of course mandatory in this application. Cold loads have the notable property, that they, unlike passive or typical active devices, can exhibit a noise temperature that is *below* the physical temperature of the device $T_n \leq T_{phys}$. In this work they will be referred to as *Active Cold Loads* (ACL). The theory of such an active cold noise source was first published in [27], where the resultant circuit was called *COLFET*. The principal functionality is described as followed: "The input impedance of the FET (Field Effect Transistor) is predominantly capacitive (there is a small series resistance) with the result that an inductance added to the source circuit is transformed to appear as a noiseless resistor in the gate circuit. This phenomenon allows the development of FET amplifiers with low-input VSWR (Voltage Standing Wave Ratio). Another consequence of the impedance transformation at the input is that only part of the total input resistance contributes noise to the circuit, that portion due to the source inductance being noiseless. This offers the possibility that the input impedance of such an amplifier may be resistive with the apparent temperature of the resistance being much less than ambient and in fact comparable with the noise of the circuit when used as an amplifier." For the typical two-point calibration this offers the following advantages: Using an ACL as the *cold* reference, the ambient load becomes the *hot* reference. No absorber or other load needs to be physically heated, which reduces the power consumption and avoids all problems related to thermal flux. Furthermore, the calibration references encompass the temperature to be observed, which significantly reduces the extrapolation error and avoids an excess of the dynamic range. Especially, the ACL offers significant advantages compared to conventional cold loads such as liquid gas (which is an expensive additional payload) or cold sky (which necessitates additional mechanics). But also in the application as a Dicke-load in an unbalanced switching radiometer, the ACL has notable advantages. Compared to an ambient reference load, the radiometric resolution of the radiometer improves, if an ACL is used instead - especially for targets with low brightness temperatures. This can be explained with the help of the following equations [26]. The radiometric resolution ΔT of an unbalanced Dicke switching radiometer is composed of the contributions due to system noise ΔT_S, gain fluctuations ΔT_G, and calibration noise ΔT_C.

$$\Delta T = \sqrt{\Delta T_S^2 + \Delta T_C^2 + \Delta T_G^2} \tag{2.3}$$

Where ΔT_S, in turn, is defined by

$$\Delta T_S = \sqrt{\frac{2T_{Sys}^2 + 2(T'_{Ref} + T'_{Rec})^2}{B_n \cdot \tau_S}} \tag{2.4}$$

with

$$T'_{Ref} = L_A \cdot T_{Ref} \tag{2.5}$$

and

$$T'_{Rec} = L_A \cdot T_{Rec} \tag{2.6}$$

B_n is the noise bandwidth and τ_S the scene integration time. T'_{Ref} and T'_{Rec} are the noise temperature of the reference load and the receiver noise temperature, respectively, at the antenna *input* reference plane and L_A the ohmic losses of the antenna and the antenna feed. Not surprisingly, the radiometric resolution can be improved with a low system noise temperature T_{Sys} and a low receiver noise T_{Rec}. But obviously, also the physical temperature of the reference load T_{Ref} - or in the case of an active electronic load - its noise temperature play an important role. The lower the reference noise temperature is, the better the system noise dependent radiometric resolution. The same correlation is observed with

$$\Delta T_C = \sqrt{\frac{2T_{Sys}^2 + 2(T'_{Ref} + T'_{Rec})^2}{B_n \cdot N \cdot \tau_C}} \tag{2.7}$$

with the difference, that the radiometric resolution can be further improved by the number of calibrations N, that are included in the calibration averaging. τ_C the calibration integration time. For unbalanced Dicke switching radiometers, this number can be greatly increased due to the improved stability compared to a total power radiometer.

$$\Delta T_G = |T_A - T'_{Ref}| \cdot \left(\frac{\Delta G}{G}\right) \tag{2.8}$$

Finally, Equation 2.8 shows, that the radiometric resolution is best, if the reference temperature at antenna input is close to the antenna temperature T_A (which is the noise temperature at antenna input while the target is observed). In this case the influence of the gain fluctuation ΔG will be minimal. This means that for typical observation scenes and especially for scenes with a low brightness temperatures, cold references are advantageous for the radiometric resolution. But also for the radiometric stability the temperature difference between observed target and the reference is important. Pseudocorrelation radiometers have been reported to have $\frac{1}{f}$ knee-frequencies in the order of few mHz when their internal reference is stable, and the observed brightness temperature is close to the reference [26].

An overview of published ACLs is presented in Table 2.1. Please note, that the W-band ACLs in [28] and [29] are pre-published results of this work.

2.4 Front-End Switches

No matter which of the previously described calibration references is used, a front-end switch is necessary to switch between the reference and the desired input signal of the radiometer.

Table 2.1: State-of-the-art of ACLs realized in different technologies and at different frequencies.

Cit., year	Technology	Frequency [GHz]	Noise Temp. [K]
[27], 1981	GaAs MESFET	1.4	50
[30], 1997	InP HEMT	18	105
[31], 2000	GaAs mHEMT	$2-10$	90
		10-26	125
[32], 2008	GaAs pHEMT	$4-8$	100
[33], 2009	GaAs pHEMT	10.69	56
			77
[34], 2010	SiGe HBT	1.4	65
[35], 2010	GaAs mHEMT	23.8	72
[28], 2012	GaAs mHEMT	$87-110$	155
[29], 2015	GaAs mHEMT	31.4	75
[29], 2015	GaAs mHEMT	52.0	141
[29], 2015	GaAs mHEMT	89.0	170

Even though in laboratory conditions it is possible to disconnect and and connect several front-ends such as an antenna or different loads to the same radiometer to perform calibration measurements, this is not practical in a typical operation mode. Depending on the type of radiometer, a maximum calibration interval needs to be maintained, for example $<$10 s for total power radiometers [26]. For switches used in PMMW imaging, especially at video-rate or in multi-channel systems, even much faster switching is required.

2.4.1 Mechanical Waveguide Switches

The most mature technology for radio frequency (RF) and microwave switches are mechanical or electromechanical waveguide switches. The latter can be controlled by an electrical signal and both have the best performance in terms of insertion loss and isolation. However, their major drawback is a limited reliability due to mechanical wear. If thousands of switching procedures are necessary, degradation and failure are imminent. While acceptable in laboratory conditions or with accessibility for maintenance or replacement, they are not used for radiometer calibration on board of satellites or space probes [36]. On such vehicles they are merely used for one time operation, for example to switch to redundant systems in case of an instrument defect. Likewise, they are not suited for the application in PMMW imaging systems, due to the limited switching speed.

2.4.2 MEMS Switches

An emerging technology are Microelectromechanical System (MEMS) switches, which are superior to the established electromechanical switches in terms of size, weight, cost, and power consumption. Due to the physical separation or contacting of the conducting structure, the performance of MEMS switches is remarkable in terms of isolation and insertion loss, respectively. However, their performance is typically demonstrated in a stand-alone configuration i.e. as a Single-Pole Single-Throw (SPST) switch with simple on/off capability. Applications in a SPDT, SP3T, etc. which are based on a topology with impedance

transforming lossy transmission lines to a common star point are rare. In this respect, a performance comparison to other switch types is often biased. Furthermore, the technology is also not yet considered to be mature enough for reliable implementation in critical systems such as satellite instruments.

2.4.3 FET Switches

"Solid state switches are more reliable and exhibit a longer lifetime than their electromechanical counterparts due to their superior resistance to shock, vibration and mechanical wear. They also offer a faster switching time. However, the higher innate *ON* resistance of the of the solid state switches gives them higher insertion loss than electromechanical switches. Therefore solid state switches are preferred in systems where fast switching and long lifetime are essential." [37] There are two main types of solid state switches: PIN diode (a semiconductor with a p-type, an intrinsic, and a n-type region) switches and FET switches, as well as combination of both (hybrid). While PIN diodes are current-controlled, the conductivity of the channel in the FET is depending on the electric field which is voltage-controlled, hence, FET switches having the lower current consumption. On the other hand, PIN diode switches achieve even faster switching speeds and exhibit a lower insertion loss than FET switches. However, the focus of this work will be on FET switches because it is possible to implement them in the same technology as the presented active electronic loads and to combine them to an integrated switching calibration front-end (SCFE).

2.5 Overview of Calibration Concepts

An exemplary overview of past, on-going and future air- or space-based vehicles, their onboard instruments and its calibration method are summarized in Table 2.2. For most past and on-going satellite missions, conventional external references such as the cold sky and an external black body are still widely spread and well established. Some spaceborn microwave remote sensing radiometers replace the external hot reference by an internal matched load at ambient temperature, still relying on the cold sky as a cold reference. In recent satellite radiometers, noise diodes have been applied as a hot reference, allowing to use the internal matched load as a cold reference. By that, the radiometer does not rely on external targets for the calibration of the instrument itself (i.e. instrumental drift or gain and noise variations). However, it should be noted that these internal calibration procedures do not include the influence of the antenna and feeding networks. To include these factors into the calibration loop, a complementary calibration with external references is necessary. Since these other factors, however, do not fluctuate as fast as the instrument, much longer calibration intervals are possible. For airborne or ground-based radiometers, the requirements for the calibration procedures might be less strict, depending on the application. Typical data acquisition flights of unmanned aerial vehicles (UAVs) or aircrafts are very limited in time, compared to space flights. And ground based instruments do normally not have a limitation of payload or power consumption, thus even more extensive procedures as cooling or heating artificial black bodies or other loads are possible. In conclusion, the appropriate calibration concept needs to be chosen with regard to the planned mission profile and often a combination of different references is chosen. The pixel normalization as it is necessary for PMMW imaging

was not taken into account in this overview, because typically this application requires no *absolute* calibration.

2.6 Low-Noise Amplifiers

Low-noise amplifiers (LNAs) are elementary components of every radiometer system. To amplify the very weak signals, relevant in radiometry and radio astronomy, a high gain is as important as the low-noise performance. Equally, LNAs are most important for noise measurement systems, as will be seen in Chapter 4. Since this work does not focus on the design of LNAs in general, a state of the art overview is omitted at this point. However, a custom-designed broadband D-band LNA was part of this work, as it was necessary for the characterization of the D-band ACLs and no commercially available LNAs did satisfy the necessary requirements. Therefore, a comparison of the developped D-band LNA to the state of the art will be presented in Chapter 6.

Summary and Conclusion

After a short introduction into radiometry, conventional calibration references and active electronic loads were introduced. Different front-end switch types were evaluated and an overview of common calibration concepts, used in scientific instruments, was given. Up to now, loads and switches were separate components in internal calibration systems.
The following chapter will now focus on the design of Millimeter-Wave Monolithic Integrated Circuits (MMICc), that will allow a *novel* calibration concept in the future. The MMICs will incorporate the front-end switch together with active loads into a complete internal calibration front-end.

Table 2.2: Vehicle, radiometer instruments and applied calibration references.

Cit.	Vehicle	Instrument	Cold Ref.	Hot Ref.
Earth Observation				
[38]	SMOS	CAS / MIRAS	Cold Sky	Noise Diode
[39]		NIR		
[40]	Aqua	HSB	Cold Sky	External Black Body
[41]	OceanSat-1	MSMR	Cold Sky	External Black Body
[42]	SeaSat	SMMR	Cold Sky	Matched Load
[43]	Topex / Poseidon	TMR	Cold Sky	Matched Load
[44]	Jason-1	JMR	Mached Load	Noise Diode
Space Probes				
[45]	Juno	MWR	Matched Load	Noise Diode
Airborne				
[46]	Global Hawk	HAMSR	External Black Body	External Black Body
[47]	NASA Aircraft	PSR	External Black Body	External Black Body & Noise Diode
Ground Based				
[48]	-	AWVR	Matched Load	Noise Diode

3 Active Load Integrated Circuit Design

For the design of active electronic loads, several circuit properties need to be taken into account. Beside the main goal to achieve the lowest possible noise temperature, further emphasis must be placed on circuit stability, sensitivity, reliability and the possibility to integrate the loads with other components such as switches or LNAs. These factors rely on a trade-off in the choice of technology and circuit topology, available simulation models, and of course careful choice of circuit design parameters, which will be discussed in this chapter.

3.1 Operating Frequency

The choice of frequencies for the circuits presented in this work is based on two considerations. The atmospheric microwave and millimeter-wave attenuation is frequency dependent and increases with higher frequency. Furthermore, it has local maximums, that are caused by the resonance frequencies of the O_2 and H_2O molecules contained in our atmosphere. These maximums limit the usable range in the electromagnetic spectrum. Between these maximums however, so called *atmospheric windows* allow the penetration of electromagnetic waves through the atmosphere. Such windows are located around the frequencies of 90 GHz and 140 GHz and are highlighted in blue in Figure 3.1. Therefore, the W-band ($75-110$ GHz) and the D-band ($110 - 170$ GHz) are the targeted frequency bands for applications in remote sensing and imaging, where a trade-off between high geometrical resolution (i.e. high frequency) and low attenuation is desired. Another motivation is the previously mentioned intended application of ACLs in the calibration of radiometers for PostEPS / MetOp SG missions. Within the scope of [19], circuits at 31.4 GHz, $50 - 54$ GHz and 89 GHz where developed and manufactured, of which some of the W-band activity will be presented in this work and compared to alternative approaches.

3.2 Technology

In a rough initial approximation, the lowest achievable noise temperature of a well designed ACL is limited by the minimum noise temperature of its internal amplifier [26]. Hence, the choice of a low-noise transistor technology is most important. In a dedicated ACL technology trade-off study from 2005, several transistor technologies have been evaluated, based on existing literature and ACL publications [49]. In this study, Indium Phosphide (InP) High Electron Mobility Transistors (HEMTs) or InP pseudomorphic HEMTs (pHEMTs) were still considered too immature and too exotic for the robustness needs of an ACL used as a calibration load. However, availability and technological maturity of some of the investigated manufacturing processes have significantly changed since then. Also, the targeted frequency

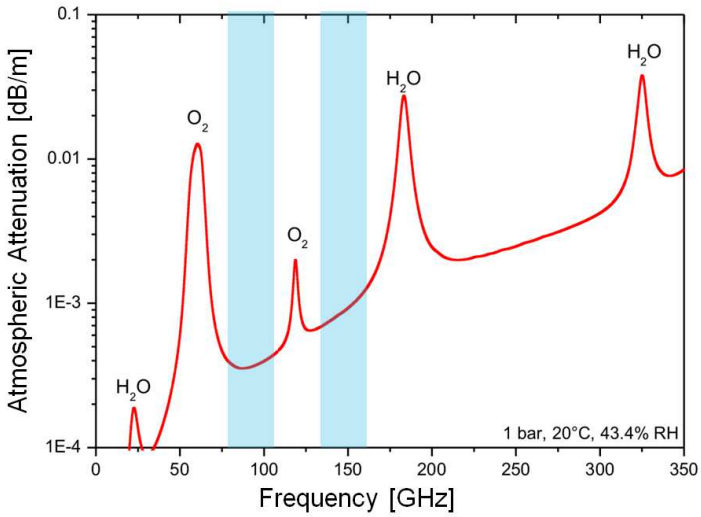

Figure 3.1: Atmospheric attenuation.

range ($f \leq 10\,\text{GHz}$) of the mentioned study differs from the circuits presented in this work. Table 3.1 summarizes the considerations of the report with regard to recent semiconductor technology developments and the frequency requirements of this work. FET technologies unlike Bipolar Junction Transistors (BJTs) and Heterojunction Bipolar Transistors (HBTs), suffer from $\frac{1}{f}$-noise due to surface and interface (trapping) effects of the semiconductor. However, [49] states, that $\frac{1}{f}$-noise is not the relevant parameter for ACLs. Furthermore, especially at higher frequencies, the benefit from high electron mobility and velocity favors the use of HEMT technology. This is supported by the fact that all ACLs above $2\,\text{GHz}$ listed in Table 2.1 are manufactured either in HEMT, pHEMT or metamorphic HEMT (mHEMT) technology. A more recent study from 2010 also compares the simulation results of ACLs with different types of transistors [50]. In the investigated frequency bands around $23.8\,\text{GHz}$ and $36.5\,\text{GHz}$ it clearly comes to the conclusion, that - compared to Silicon Germanium (SiGe) HBTs and pHEMTs - the lowest noise temperature can be achieved with mHEMT transistors. It should be noted, that InP HEMTs were not investigated in this study. While the limitation of SiGe HBT technology already becomes evident around $23\,\text{GHz}$, where no noise temperature below $210\,\text{K}$ can be achieved, the report states, that to achieve noise temperatures below $180\,\text{K}$, mHEMT technology is believed to be suitable even at frequencies much higher than the investigated $36.5\,\text{GHz}$.

3.2.1 MMIC Technology

While most of the previously published loads had to fall back on discrete packaged transistors in a hybrid design with external feed- and matching networks, this work benefits from the advancement in MMIC technology. This allows not only a very compact design of the active loads, especially at higher frequencies, but also the integration with a switch for an *Active Calibration Sub-System* (ACSS) or even with the radiometer front-end. Furthermore, MMIC technology facilitates mass production with repeatable performance and can be qualified for space application [50].

Table 3.1: Transistor technology trade-off in regard of suitability for ACL design.

Technology	**Characteristics**
BJT	+ current flow perpendicular to semiconductor surface and therefore considerable lower $\frac{1}{f}$-noise than FETs − high noise figure
HBT (InP, GaAs, SiGe)	− in general III/V HBTs have inferior noise performance at high frequencies than III/V FETs + InP HBTs are suitable for ultra-low power applications + GaAs HBTs have better noise performance than InP HBTs − SiGe HBTs have comparable noise performance to GaAs MESFETs and GaAs HEMTS but only at low frequencies
GaAs MESFET	− compared to other recent FET technologies the highest minimum noise figure
GaAs HEMT	+ 2-DEG creates high concentration and mobility of electrons thus, higher maximum operating frequency and lower noise figure than GaAs FETs
GaAs pHEMT	+ better noise figure than GaAs HEMT + better frequency performance than GaAs HEMT
GaAs mHEMT	+ even higher doping levels possible than in pure InP HEMTs + equivalent performance as InP HEMTs + lower cost than InP and larger wafer size
InP HEMT	+ best III/V FETs for microwave applications in terms of operating frequency and noise figure − fragile substrate, structures like vias are difficult to manufacture − lower process yield, limited wafer size

Prediction of Achievable Noise Temperature

To estimate the achievable ACL noise temperature in W-band with the above mentioned rough approximation, some published MMIC LNAs with their respective manufacturing technology shall be shortly reviewed. [51] and [52], report on InP-based HEMT amplifiers with noise figures of 2.7 dB (100 nm gate) and 2.5 dB (50 nm gate) at 94 GHz, respectively. In [53], an antimonide based compound semiconductor (ABCS) amplifier with InAs channel is presented, exhibiting a noise figure of 2.5 dB at 90 GHz. The conversion between noise figure in dB (NF (dB)) to noise temperature (T_n) is performed by applying Equation 3.1, where T_0 is per definition always 290 K.

$$T_n = T_0 \cdot \left(10^{\frac{NF(dB)}{10}} - 1\right) \tag{3.1}$$

The achieved NF (dB) in the cited work of 2.5 dB thus corresponds to a T_n of 226 K. In [54], an InP HEMT LNA with 35 nm gate length is presented, which even achieves a measured T_n in a waveguide package of 200 K. With IAF's 50 nm mHEMT technology which is presented in the next subsection, an LNA with T_n of 160 K was published in [55]. This confirms the suitability of HEMT based MMIC technology for the design of low noise circuits and gives an estimation of the expected achievable T_n for ACLs. Further evidence is presented in [26], where noise temperatures of 160 K and 180 K on MMIC level are predicted at 89 GHz and 100 GHz , respectively. This report also states, that MMIC-based ACLs up to 101 GHz are realistic for the use in Post-EPS context. However, it should be pointed out that these estimations, based on published LNA performances, are only rough approximations. The MMIC matching- and feed networks of LNAs contribute to the noise of the amplifier and are different in topology than for active loads. The main difference is, that an LNA is an *amplifying* two port device, typically consisting of multiple transistor stages, where the matching at the output port has very little influence on the noise generated in the first transistor stage. Whereas active loads are typically one-stage, one-port devices where the noise temperature on *gate* side of the transistor is of interest and very sensitive to reflections on the drain side. A detailed discussion of the simulated noise temperature of active loads and the influence of matching networks is presented in Section 3.3.

3.2.2 IAF's mHEMT Process

For the design of the presented MMICs in this work, IAF's in-house mHEMT technology was used. Indium Gallium Arsenide/Indium Aluminum Arsenide heterostructures (InGaAs/InAlAs) with high In-content in the electron transport channel are grown on 4 inch semi-isolating GaAs wafers by molecular beam epitaxy (MBE). This approach allows to process highly integrated ultra low noise circuits on cost-efficient GaAs wafers. To adapt the lattice constants of the heterostructure and the substrate, a metamorphic buffer layer is grown in between. Parasitic substrate modes are supressed, by applying a backside process to the wafer, where it is thinned down to a final thickness of $50\,\mu$m. Subsequently, through-substrate vias with $20\,\mu$m contact diameter to the front side are processed by dry etching and finally, the wafer backside is gold plated.

Passive Components

In addition to the active devices, metal-insulator-metal (MIM) capacitors, NiCr thin film resistors and airbridge technology are provided for circuit layout, as well as grounded coplanar waveguides (GCPW) as transmission lines. With these passive components, input matching networks (IMN) and output matching networks (OMN) can be realized, as well as DC bias and RF blocking structures. IAF's mHEMT process features gate lengths from $20\,\text{nm}$ to $100\,\text{nm}$, which differ in their technological properties. Details can be found in [55] ($100\,\text{nm}$ and $50\,\text{nm}$), [56] ($50\,\text{nm}$ and $35\,\text{nm}$), [57] ($35\,\text{nm}$) and [58] ($20\,\text{nm}$). Different gate-lengths were chosen for the active loads, switches and LNA and will be stated in the respective section.

Small-Signal Model

To chose the ideal transistor size and bias point for optimum noise performance (and gain in the case of LNA), a versatile small-signal model of the used transistors was available [59]. It consists of an intrinsic part and a parasitic shell, is bias dependent, and features the prediction of noise parameters. It is parametrized, so that different gate widths and number of gate fingers can be simulated. The characterization of active and passive test structures, as well as the modeling itself is done in-house. Hence, an extensive IAF proprietary model library was available for designing and optimizing the MMICs, using the computer aided design (CAD) software *Advanced Design System* (ADS) by *Keysight Technologies*.

3.2.3 Long-Term Stability

If ACLs are intended to be used as calibration references in radiometer systems, especially on board of satellites, not only the short-term, but also the long-term stability of the noise temperature is most crucial. Similar to the gain stability of (low-noise) amplifiers in radiometers, the noise stability of active electronic loads is dependent on the utilized manufacturing technology of the device. For existing ACLs, few investigations have been published, proving the feasibility of active loads in different technologies.

In [60], [61], and [62], the short-term and intermediate-term stability of a SiGe HBT based ACL at $1.4\,\text{GHz}$ was investigated. Over a duration of one week, the noise temperature varied less than $40\,\text{mK}$. During a four month period of continuous operation the maximum variation of the ACL is reported to be $0.35\,\text{K}$ and assuming a linear drift versus time, a value of less than $1\,\text{K/year}$ is extrapolated. In [63] the results of the SiGe HBT ACL were compared to a GaAs pHEMT ACL at the same frequency, showing a similar performance with a variation of $0.26\,\text{K}$ during two and a half months. [64] investigated the stability of a $18\,\text{GHz}$ noise source, which is referred to as a *variable temperature source* (VTS). Presumably, this is the InP HEMT based ACL presented in [30]. On a short-term period, they report a slope of $0.05\,\text{K/day}$ around a mean noise temperature of $127.2\,\text{K}$ and a measured long-term increase of the noise temperature of $2\,\text{K/year}$ around a mean noise temperature of $126.1\,\text{K}$. In [65] the noise temperature of a GaAs pHEMT ACL at $10.69\,\text{GHz}$ was monitored in a temperature stabilized test-bed over a time period of one year. Around a mean noise temperature of $77\,\text{K}$, a drift rate in the order of $1.5\,\text{K/year}$ during the first eight months of operation were observed and around $2\,\text{K/year}$ over the entire measurement period. The only studies

found, analyzing the noise stability of a GaAs mHEMT ACL were [35] and [50]. However, the investigated $23.8\,\text{GHz}$ ACL was also at a much higher operating frequency than any of the listed above, that were investigated over a longer time period in a stabilized test-bed. [50] reports a variation of the noise temperature of less than $0.5\,\text{K}$ around $72\,\text{K}$ during one month. In conclusion, the utilized GaAs mHEMT technology for the circuits developed in this work is believed to satisfy the necessary requirements for the stability of the active loads. Especially, since all of the previously published ACLs above $20\,\text{GHz}$ were manufactured in this technology.

3.3 Stand-alone Active Loads

Even though a limited set of active *cold* loads was previously published (see Table 2.1), there exist no standard guidelines for the design of active loads. The primary design goals are evidently to obtain the lowest possible noise temperature for cold loads and a high noise temperature for hot loads at the *output* of the load, while achieving a very high return loss in the frequency range of interest. In this work several active hot and cold loads, as well as integrated hot-cold loads were developed, using different simulation and design approaches, which will be presented in the following.

3.3.1 ACL Topology

As explained in Section 2.3, the principle functionality of an ACL is based on an impedance transformation of the capacitive input impedance of the FET with an inductive source, so that the resistive portion of the source inductance appears noiseless and the total input resistance appears to generate less noise. This is a similar approach as for the design of LNAs and as generally known, the challenge in LNA design is to achieve a simultaneous noise and power matching at the input. The common methods to modify the transistor's input impedance without modifying its optimum source reflection coefficient for low-noise are either feedback circuits or a deliberate output mismatch. The latter, however, is not an option for ACL design: Any mismatch at the output would cause to reflect the generated noise on drain side back thru the transistor to the input and increase the ACL's noise temperature. Therefore, as will be explained in the next section, some of the simplified noise temperature simulation approaches even assume a perfect match on drain side and/or a minimum backward gain of the transistor.
As stated in [50] and [66], two different topologies for the design of active loads are possible, to achieve the above mentioned design goals: an inductive or a parallel feedback, as illustrated in Figure 3.2. The latter, however, would not be suitable in a hybrid circuit, because to achieve a specific transconductance value for optimum input matching, the gate dimensions of the transistor have to be varied. In all the presented circuits in this work, exactly that was investigated, to achieve optimum performance. Nevertheless, the inductive feedback topology was chosen, just as in most previously published work, because the possible variation of the feedback inductance gives an additional degree of freedom in the design of the circuits. This simplifies to simultaneously achieve the different design goals.

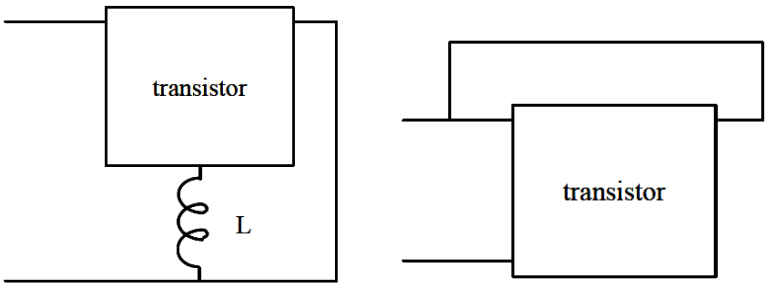

(a) Inductive feedback (b) Parallel feedback

Figure 3.2: Different topologies for the active load design as described in [50].

3.3.2 Simulation of Noise Temperature

For the description of the circuits and the simulation process, standard terminology of scattering parameters (S-parameters), gain G, and reflection coefficients Γ, as described in [67], [68], and [69] will be used. The noise characteristics of noisy two-port are described by its noise parameters, the noise resistance R_n, the minimum noise figure F_{min} and the real and imaginary value of the source impedance for minimum noise, which typically is described by the source reflection coefficient Γ_{opt} [70]. With the available small-signal model of the transistor, ADS calculates the network parameter matrices S, Z, and Y, as well as the noise parameters R_n, S_{opt}, NF, NF_{min}, T_e, and the noise current correlation matrix I_{cor}. The latter is particularly important for the novel approach in this work and will be further explained in Section 3.3.4. With these parameters available, different approaches are possible to design active electronic loads with the desired noise level and the appropriate matching networks, yielding optimum return loss at the output port. Three different simulation methods were used to design the circuits presented in the following sections:

- The general approach of *Weatherspoon* and *Dunleavy* which is described in [71], is valid for an arbitrary non-matched output and was utilized to design the active loads in the framework of the ESA project *Calload* [19]. By subsequently designing output- and input matching networks , the noise temperature calculation can be further simplified. The practical design flow and the discrepancy in the simulation results is presented in this work on the basis of the $89\,\mathrm{GHz}$ ACLs for the Active Calibration Sub-System.

- The simplified approach by *Wait* and *Engen* [72] assumes perfect match on drain side of the transistor and was utilized to design the ACL in the integrated hot-cold noise source published in [73]. By similarly designing an input network for optimum noise matching on gate side, this approach results in a noise temperature simulation very similar to the above.

- A novel, further simplified numerical method, derived from standard noise power calculation, using noise-model parameters and ADS optimization algorithms to design AHLs and ACLs in W-band [28], [74], and ACLs in D-band.

Since the nomenclature of the previously introduced noise parameters used by ADS and common literature are somewhat different, Table 3.2 compares the equivalent denotations.

Table 3.2: Denotation of noise related parameters in literature and in ADS.

Literature	ADS parameters and functions
Γ_{opt}	S_{opt}
G_{opt}	$real\left(\frac{1}{Z_0} \cdot \frac{S_{opt}-1}{-1-S_{opt}}\right)$
$T_{e,min}$	$T_0 \cdot \left(10^{\frac{NF_{min}}{10}} - 1\right)$

In the following description of the noise calculations throughout this work, the standard nomenclature which is common in literature will be used. Further ADS specific parameters like I_{cor}, which will be necessary for the explanation of the novel numerical simulation method, will be introduced in the accordant sections.

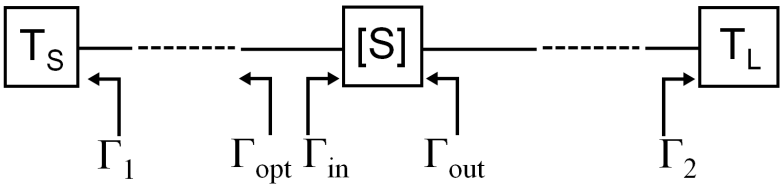

Figure 3.3: The transistor described by its S-parameters in a standard two-port noise representation with the accordant reflection coefficients and the external terminals.

In general, an active load is a one-port device which provides the wanted noise temperature, depending on its internal circuitry. The internal circuitry consists of an active device, typically a transistor, some kind of In Figure 3.3 the core element of the active load, the transistor, is described by its S-parameters and connected to external terminals. Since this representation is based on the design of low-noise *amplifiers*, the orientation of the source on the left side (T_S) and the load on the right side (T_L) will be maintained throughout this work. Likewise, matching networks on the source side will be labeled as input matching networks (IMN) and on the load side output matching networks (OMN), as shown in Figure 3.4. However, in the case of active loads, the relevant terminal for the calculation of the noise temperature is T_S. Without any matching networks, the generated noise temperature $T_{s,1}$ depends only on the transistor parameters and the reflection coefficients and can be calculated by

$$T_{s1} = T_b + \left(\left(T_1\left(1-|\Gamma_1|^2\right)+T_a\right)G_{21}|\Gamma_2|^2 + T_2\left(1-|\Gamma_2|^2\right)\right)G_{12} \tag{3.2}$$

where T_k, T_a and T_b are *alternative noise parameters* as introduced in [71]:

$$T_k = 4 \cdot T_0 \cdot R_n \cdot G_{opt} \tag{3.3}$$

$$T_a = T_{e,min} + \frac{T_k \cdot |\Gamma'_{opt}|^2}{1-|\Gamma'_{opt}|^2} \tag{3.4}$$

$$T_b = \frac{T_k}{1-|\Gamma'_{opt}|^2} - T_{e,min} \tag{3.5}$$

and Γ'_{opt} is given by

$$\Gamma'_{opt} = \frac{S_{11}^* - \Gamma_{opt}}{\Gamma_{opt} S_{11} - 1} \tag{3.6}$$

T_1 and T_2 are the noise temperatures at the terminals T_S and T_L, respectively. The available power gains G_{12} and G_{21} of the transistor are per definition [75] also dependent on the matching between itself and the external terminals. They can be expressed by the S-parameters of the transistor and the reflection coefficients:

$$G_{12} = \frac{|S_{12}|^2}{|\,(1 - S_{22}\Gamma_2)\,|^2 \cdot\ (1 - |\Gamma_{in}|^2)} \tag{3.7}$$

$$G_{21} = \frac{|S_{21}|^2}{|\,(1 - S_{11}\Gamma_1)\,|^2 \cdot\ (1 - |\Gamma_{out}|^2)} \tag{3.8}$$

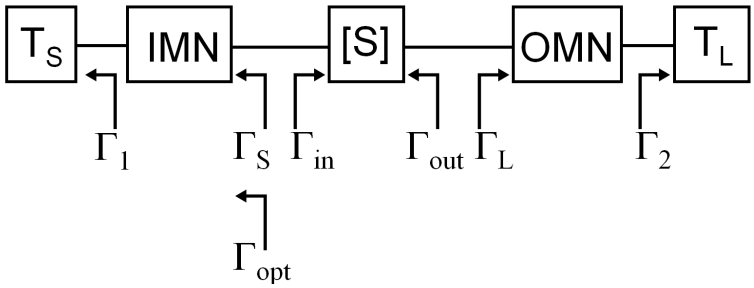

Figure 3.4: Design schematic of the transistor with appropriate matching networks to the external terminals.

So far, the noise calculation is valid for a general not necessarily matched circuit. Obviously, appropriate matching networks will reduce the noise temperature. An estimation of the lowest achievable temperature with a theoretically perfect matching is presented later on. Moreover, assuming proper matching networks the above introduced available power gains can be described independent of the external terminals. An accordant schematic is depicted in Figure 3.4. Parameters referring to this *terminal invariant* gain will have the subscript $_{ti}$ in the following. With $\Gamma_1 = 0$ and $\Gamma_2 = 0$, equations 3.7 and 3.8 can be written as:

$$G_{12,ti|\Gamma_2=0} = \frac{|S_{12}|^2}{1 - |\Gamma_{in}|^2} \tag{3.9}$$

$$G_{21,ti|\Gamma_1=0} = \frac{|S_{21}|^2}{1 - |\Gamma_{out}|^2} \tag{3.10}$$

Simultaneously, the general definitions of Γ_{in} and Γ_{out}

$$\Gamma_{in} = S_{11} + \frac{S_{21} S_{12} \Gamma_2}{1 - S_{22}\Gamma_2} \tag{3.11}$$

$$\Gamma_{out} = S_{22} + \frac{S_{12} S_{21} \Gamma_1}{1 - S_{11}\Gamma_1} \tag{3.12}$$

being simplified to

$$\Gamma_{in|\Gamma_2=0} = S_{11} \tag{3.13}$$

$$\Gamma_{out|\Gamma_1=0} = S_{22} \tag{3.14}$$

Now, Equations 3.9 and 3.10 can be written as

$$G_{12,ti|\Gamma_2=0} = \frac{|S_{12}|^2}{1-|S_{11}|^2} \tag{3.15}$$

$$G_{21,ti|\Gamma_1=0} = \frac{|S_{21}|^2}{1-|S_{22}|^2} \tag{3.16}$$

modifying 3.2 to

$$T_{s1,ti} = T_b + \left(\left(T_1\left(1-|\Gamma_1|^2\right)+T_a\right)G_{21,ti}|\Gamma_2|^2 + T_2\left(1-|\Gamma_2|^2\right)\right)G_{12,ti} \tag{3.17}$$

Based on Equation 3.17, the *theoretical lower limit* of the noise temperature can be estimated, which can be achieved with a certain transistor technology. Since for a properly designed amplifier, the backward gain G_{12} can be assumed to be minimal, the estimation $T_{s1,ti} \geq T_b$ is valid. Furthermore, a good matching network means that $|\Gamma'_{opt}|^2 \leq 1$, so that in Equation 3.5 the estimation $T_b \geq T_k - T_{e,min}$ is allowed. This leads to the concluding estimation

$$T_{s1,ti} \geq T_b \geq T_k - T_{e,min} \tag{3.18}$$

The *theoretical lower limit* is now only dependent on the noise parameters of the transistor and can therefore be calculated as

$$T_{s1,limit} = 4 \cdot T_0 \cdot R_n \cdot G_{opt} - T_{e,min} \tag{3.19}$$

To recapitulate, this theoretical lower limit of the achievable noise level is what the transistor gate exhibits if it would be simultaneously perfectly noise matched, input power matched, and load matched to its external terminals, which is of course not possible. Even physical networks that would perfectly provide the necessary impedance would add noise depending on their physical temperature, due to their own resistive losses.

If the assumption $\Gamma_1 = 0$ and $\Gamma_2 = 0$ is not only applied to the available gains, but also to the noise temperature calculation 3.17, a further simplified expression of 3.2 can be written as

$$T_{s1|\Gamma_{1,2}=0} = T_b + T_2 \cdot G_{12,ti} \tag{3.20}$$

This equation was used to simulate the noise temperatures for the $89\,\mathrm{GHz}$ ACLs within the *Calload* project [19]. It was found to be a reasonable compromise, because it accounts for the not negligible backward gain of the transistor and the not perfect noise match at the transistor gate, but assumes negligible reflections at the external ports due to the matching networks. While the practical design flow for these matching circuits is presented in the

following section on the basis of the $89\,\text{GHz}$ ACL, the discrepancy of noise temperatures calculated with the different simulation methods shall be presented beforehand. Figure 3.5 shows the different simulated noise temperatures of a $89\,\text{GHz}$ ACL, consisting of a single transistor with inductive source feedback and input and output matching networks. Obviously, the ACL was optimized to exhibit its lowest noise temperature in the vicinity of $89\,\text{GHz}$. The noise parameter $T_{e,min}$ and $T_{s1,limit}$, calculated using Equation 3.19, represent the upper and lower limit of the achievable noise temperature and enclose the other three calculation methods over a wide frequency range (Figure 3.5(a)). In Figure 3.5(b) the relevant frequency range is enlarged. While there is a difference of around $100\,\text{K}$ between the upper and lower limit, T_{s1}, $T_{s1,ti}$, and $T_{s1|\Gamma_{1,2}=0}$ only differ by around $10\,\text{K}$ at $89\,\text{GHz}$. Three conclusions are worth emphasizing:

- The curves confirm, that it is a valid approximation and a good compromise to use $T_{s1|\Gamma_{1,2}=0}$ for the simulation of noise temperature, if an error of around 5% is acceptable.
- Despite the matching networks, the backward gain of the transistor is not entirely independent of the external terminals.
- Even for properly designed matching networks the reflection coefficients at the external terminals have an influence on the generated noise temperature at the transistor gate.

3.3.3 Practical Design Flow

Following the design flowchart in Figure 3.6, the S-parameter matrix and Γ_{opt} of the bare transistor device with inductive source feedback are determined. With this information the optimum load reflection coefficient Γ_L can be calculated using Equation 3.21. The value of Γ_L strongly depends on the transistor dimension (number of gate fingers, gate length) and the length of the inductive source feedback line. While in general smaller transistors yield a lower noise temperature, they complicate the realization of the matching networks, because the optimum reflection coefficient moves closer to the edge of the Smith chart. This introduces higher losses for the matching network and increases the final noise temperature. Depending on these parameters a trade-off has to be found between minimum achievable noise temperature, realization of the matching network and stability of the device. The stability of the circuit is determined using the μ-factor as defined in [76] and is taken into account for the investigation of optimal transistor dimension and source line length.

$$\Gamma_L = \frac{\Gamma_{opt}^* - S_{11}}{S_{12}S_{21} + S_{22}\left(\Gamma_{opt}^* - S_{11}\right)} \tag{3.21}$$

In the following, Γ_L, the noise temperature and the stability of the device is analyzed at $89\,\text{GHz}$ for different transistor dimensions and different source line lengths. With regard to the optimum load reflection coefficient at this frequency, all chosen devices facilitate designing an appropriate output matching network. Table 3.3 summarizes the investigated transistor dimensions and the simulation results.

While the 4-finger transistors demonstrate lowest noise temperature with no source line at all, they demonstrate strongly increasing noise temperature with increasing source line length. This complicates the stabilization of the device which requires some inductive source

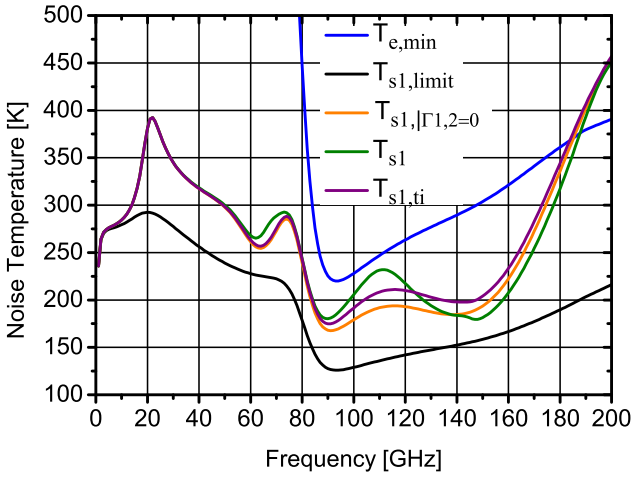

(a) Simulation results for 89 GHz ACL.

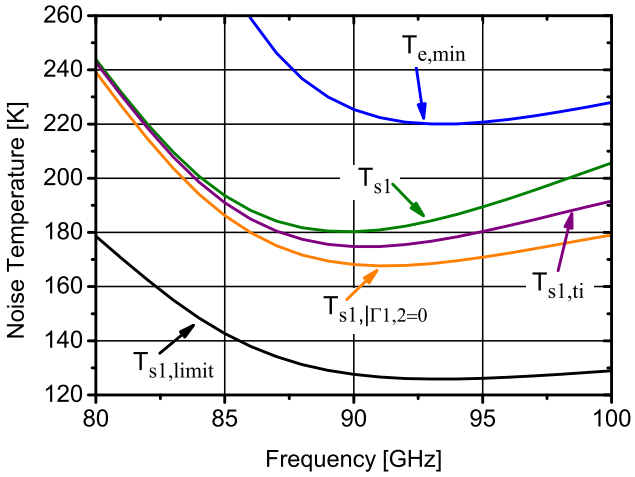

(b) Noise temperatures in the relevant frequency range.

Figure 3.5: Comparison of differently simulated noise temperatures.

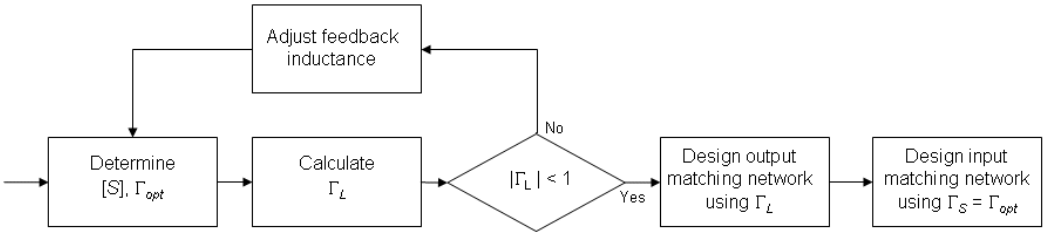

Figure 3.6: Design flow as described in [71].

Table 3.3: Best achievable results at 89 GHz for different transistor dimensions at different source line lengths.

Transistor size	Minimum $\lvert\Gamma_L\rvert$	Minimum $T_{s1\lvert\Gamma_{1,2}=0}$	Maximum μ-factor
$2 \times 10\,\mu m$	0.268 @ $75\,\mu m$	$89.413\,K$ @ $45\,\mu m$	0.997 @ $100\,\mu m$
$2 \times 15\,\mu m$	0.087 @ $35\,\mu m$	$97.308\,K$ @ $30\,\mu m$	1.013 @ $75\,\mu m$
$2 \times 20\,\mu m$	0.096 @ $30\,\mu m$	$107.014\,K$ @ $23\,\mu m$	1.036 @ $45\,\mu m$
$2 \times 30\,\mu m$	0.066 @ $30\,\mu m$	$128.797\,K$ @ $18\,\mu m$	1.108 @ $20\,\mu m$
$4 \times 10\,\mu m$	0.186 @ $7\,\mu m$	$101.895\,K$ @ $0\,\mu m$	0.988 @ $45\,\mu m$
$4 \times 15\,\mu m$	0.147 @ $5\,\mu m$	$118.626\,K$ @ $0\,\mu m$	0.991 @ $40\,\mu m$
$4 \times 20\,\mu m$	0.107 @ $10\,\mu m$	$136.519\,K$ @ $0\,\mu m$	0.999 @ $25\,\mu m$
$4 \times 30\,\mu m$	0.064 @ $27\,\mu m$	$171.031\,K$ @ $0\,\mu m$	1.023 @ $17\,\mu m$

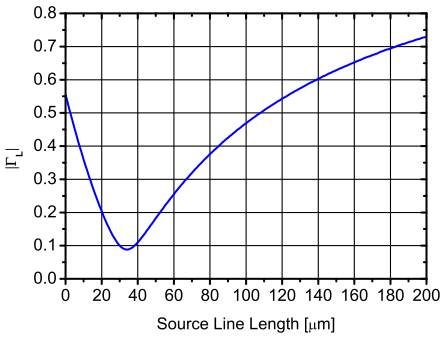

(a) Magnitude of Γ_L.

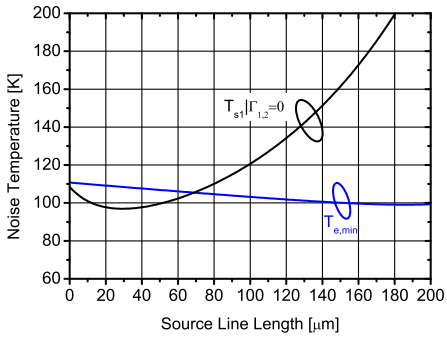

(b) Noise temperature.

Figure 3.7: $2 \times 15\mu$m transistor parameters vs. source line length.

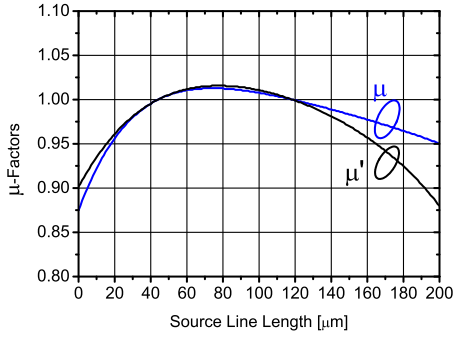

(a) μ-factors.

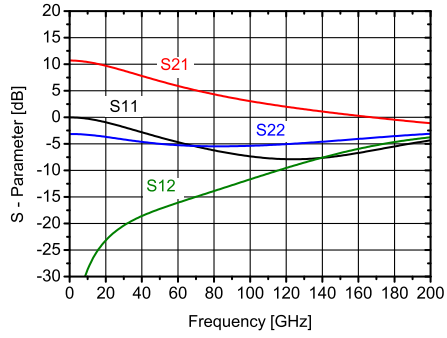

(b) S-parameters of single transistor.

Figure 3.8: $2 \times 15\mu$m transistor parameters vs. source line length and frequency.

feedback. For some of the 2-finger transistors a compromise in source line length can be found to achieve an acceptable trade-off in noise temperature and stability. The transistor in the second line of Table 3.3 is chosen for further analysis. While it has the highest μ-factor at a source line length of $75\,\mu$m (see Figure 3.8(a)), it still demonstrates a noise temperature of below $110\,$K at this source line length (see Figure 3.7(b)). Figure 3.8(b) demonstrates the S-parameters of this device versus frequency. The S_{11} and S_{22} parameters indicate no instabilities (see Figure 3.8(b). Figure 3.9(a) shows the μ-factors which are above unity at the desired frequency range.

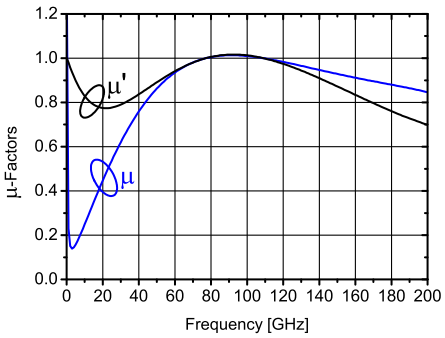

(a) μ-factors vs. frequency.

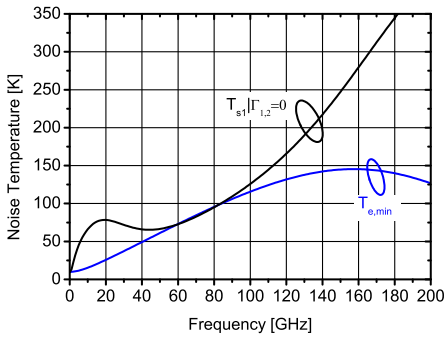

(b) Increased noise temperature.

Figure 3.9: Transistor parameters with a $75\,\mu$m $50\,\Omega$ source line.

The increase of the inductive source feedback leads to a slightly increased noise temperature, which can be seen in Figure 3.9(b). This noise temperature will further increase when the input matching network is implemented. Figure 3.10(a) demonstrates the optimum load reflection coefficient for the output matching network to obtain minimum noise temperature at the input. With this requirement, an output matching network was designed, following the design-flow in Figure 3.6. The output of the network is connected to a $50\,\Omega$ termination and the OMN designed to provide the required Γ_L on transistor side. Figure 3.10(b) compares the required Γ_L to the actual reflection coefficient of the OMN. Subsequently the input matching network was designed under the conditions for a simultaneous optimum noise match and input power match. The match of IMN to the $50\,\Omega$ terminal at the input can be seen in Figure 3.11(a), while the match at transistor side to the required Γ_{opt} can be seen in Figure 3.11(b). Finally input and output matching networks are connected to the transistor with feedback source line and the $50\,\Omega$ termination at the output is replaced by an ADS simulation port to calculate all S-parameters. The result can be seen in Figure 3.12(a). The crucial parameter is the input return loss of the ACL, which is shown in detail in Figure 3.12(b) and achieves below $-40\,$dB.

3.3.4 Novel Approach for Improved Design Flow

As the description of the practical design flow in the previous section has shown, the noise temperature of the complete ACL circuit can not be directly simulated in ADS, using the available transistor and transmission line models, but needs to be simulated in an iterative way. First, $[S]$ and Γ_{opt} need to be optimized by varying the feedback inductance. This yields the necessary Γ_L to design an OMN in the second step. Then, in the third step

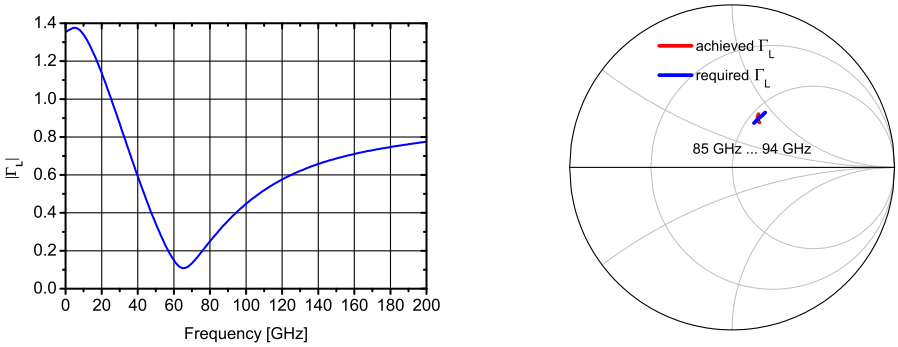

(a) Required Γ_L. (b) Achieved Γ_L of OMN.

Figure 3.10: Required and achieved Γ_L .

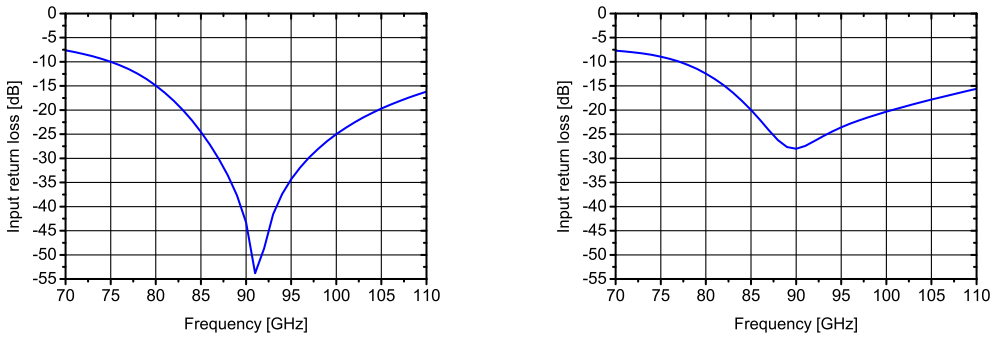

(a) Towards $50\,\Omega$ at input (b) Towards Γ_{Opt} at transistor gate

Figure 3.11: Input return loss of the input matching network.

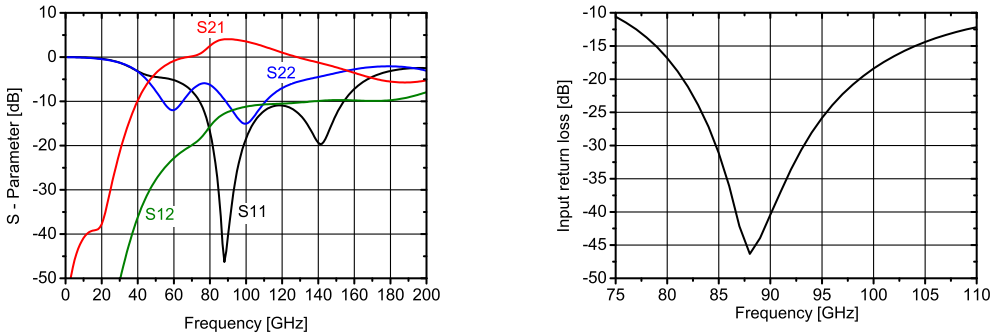

(a) S-parameters. (b) Input return loss.

Figure 3.12: S-parameters of transistor with IMN and OMN.

the IMN can be designed. What is not shown in the design flow chart in Figure 3.6, is that after connecting the designed OMN to the drain of the transistor, $[S]$ and Γ_{opt} change, because the required Γ_L can not be perfectly achieved with a physical OMN over a large bandwidth (see Figure 3.10(b)). This means, that before designing the IMN, Γ_{opt} needs to be recalculated. Moreover, two parallel projects need to be handled in ADS, because to determine the reflection coefficients, so called *Gamma-Probes* need to be placed between the stages of interest. But if the signal flow between two simulation terminals is interrupted by a *Gamma-Probe*, ADS can not calculate the noise parameters of the transistor anymore. Therefore, any change of the matching networks in one project needs to be copied to the other project, which can be a major source of error and makes it impossible to use automated optimization algorithms.
To overcome this iterative and very time-consuming procedure, and to benefit from the possibilities of modern numerical simulation methods and optimization algorithms, a novel approach was developed in this work. Based on the theory of noisy four-poles, as presented in [70], the Nyquist formula in the form

$$\overline{|i_{tot}|^2} = 4 \cdot k_B \cdot T \cdot \Delta f \cdot G_{tot} \tag{3.22}$$

with i_{tot} being the equivalent noise current of an otherwise noiseless device, and G_{tot} the total noise conductance, is transformed to calculate the noise temperature T:

$$T = \frac{\overline{|i_{tot}|^2} \cdot R_{tot}}{\Delta f \cdot 4 \cdot k_B} \tag{3.23}$$

The resistance R_{tot} is the reciprocal value of the conductance G_{tot}. Now, two implemented functions in ADS are used to compute the generated noise inside the active loads: *Icor* and *stoz(S)*. *Icor* is the noise current correlation matrix, in units of Amperes squared. It describes the short circuit noise currents squared at each port, and the correlation between noise currents at different ports. The function *stoz(S)* transforms a scattering matrix $[S]$ to an impedance matrix $[Z]$. Next, the active load as a whole, i.e. *with* its matching networks and the inductive feedback, is considered as a noisy two-port device and placed between two simulation terminals. The circuit is now characterized by its scattering matrix $[S]$ and the noise currents *Icor*. Expression 3.24 now allows to directly simulate the noise temperatures at the external terminals. For the noise temperature only the real part of the resulting matrix is of relevance and the missing bandwidth Δf can be omitted, because for spectral noise simulation the bandwidth is set to $1\,\mathrm{Hz}$.

$$[T] = Re\left(\frac{[stoz(S)] \cdot [I_{cor}]}{4 \cdot k_B}\right) \tag{3.24}$$

Having this expression available, it can be used as a goal for automated optimization algorithms, which are implemented in ADS. Another simultaneous goal must be the input return loss. After defining the frequency range and the targeted values of the goals, the parameters which the algorithm is allowed to vary and the limits within which they can be varied must be specified.

3.3.5 Generic Design Schematic

The described design flow in Section 3.3.3 was the basis for several active load circuits at different frequencies. Hence, in successive iterations, details of the matching networks were varied to optimize the performance for a specific frequency range or to balance different parameters like maximum return loss, minimum noise temperature, and stability against each other. To avoid multiple slightly different schematics for the circuits presented in following sections, a general design schematic shall be discussed beforehand.

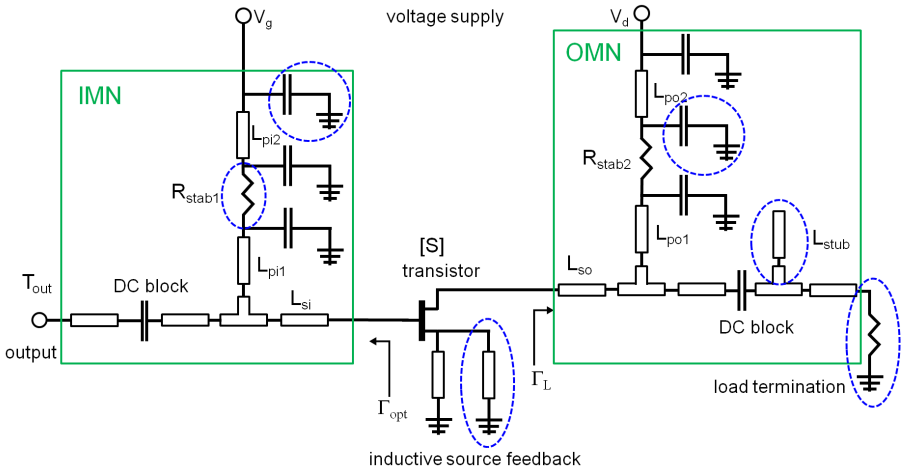

Figure 3.13: Generic design schematic of an ACL.

Figure 3.13 depicts the transistor as the core element of the active load. After choosing the number and length of gate fingers, the S-parameters and Γ_{Opt} of the transistor can be varied by adopting the feedback inductance. This is achieved with at least one shorted transmission line which is connected to the source of the transistor and labeled as inductive source feedback in the schematic. To attain symmetry in the layout, the feedback can be applied at both source connections of the transistor. However, for some of the designs it was beneficial to use one single transmission line because two parallel transmission lines require more length to achieve the necessary inductance. All other optional elements that were not implemented in all designs are marked with blue dotted circles in the schematic. The variation of line length and line impedance of the series transmission line L_{so} and the parallel transmission line L_{po1} yields the necessary Γ_L for the output matching. For some designs it was helpful to include another open stub L_{stub} to reach this goal. L_{po1}, R_{stab2}, and L_{po2} are in addition used to supply the drain voltage to the transistor and with additional parallel capacitors to ground, to decouple the voltage supply from the microwave signal. Both series capacitors serve as a DC-block towards the external terminals. In case of the OMN, the circuit is terminated with an optional $50\,\Omega$ load to ground in which case the DC-block is not necessary. But in case of the ACL for the integrated hot-cold load, this terminal is used as the *hot* output terminal, which makes the DC-block necessary. In analogy to the OMN, the variation of line length and line impedance of the series transmission line L_{si} and the parallel transmission line L_{pi1} yields the simultaneous noise and power matching at the input. Again, the transmission lines L_{pi1}, L_{pi2}, and L_{si}, and the resistor R_{stab1} are at the same time used to provide the gate voltage to the transistor and the parallel capacitors to ground to decouple the microwave signals. In the case of the IMN however, the implementation of R_{stab1} which

is improving the circuit stability, is very critical, because the noise generated in this resistor at ambient temperature directly adds to the noise of the ACL. Therefore, it was replaced in most designs by a transmission line. The influence of R_{stab2} in the OMN was investigated as well, but due to the limited backward gain of the transistor, it has no significant impact on the noise temperature. All unlabeled transmission lines in the schematic have merely connection purposes.

3.3.6 Realized Circuits

89 GHz ACLs for Active Calibration Sub-System

In Figures 3.14(a) and 3.15, the chip photographs of the two 89 GHz ACLs that were realized in the framework of the ESA project *Calload* [19] are shown. Both measure a size of 1×1 mm^2. It can clearly be seen, that their matching networks differ significantly. While the main focus of the first version was to achieve lowest possible noise temperature, the second design was optimized to improve the input return loss, which for the first version turned out to be worse than simulated (see Chapter 5). Another goal was a more compact layout, facilitating better integration into the ACSS. Both designs use GCPW transmission lines with different line impedances, which are recognized by the width of the transmission line. The more narrow ones are $70\,\Omega$ lines, while the more wider ones are $50\,\Omega$ lines. The transistor, the NiCr thin film resistors in the OMN and the source line inductance are labeled and marked by arrows. Furthermore, the MIM capacitors are recognized as the square structures that are connected to the transmission lines or the voltage supply. The smaller square structures that are spread on the chip are the through-substrate vias. For voltage supply, the IMN and OMN are connected to DC pads at the top of the chips. They can either be contacted by DC-probes for on-wafer measurements or gold wires can be bonded to the pads for module assembly.

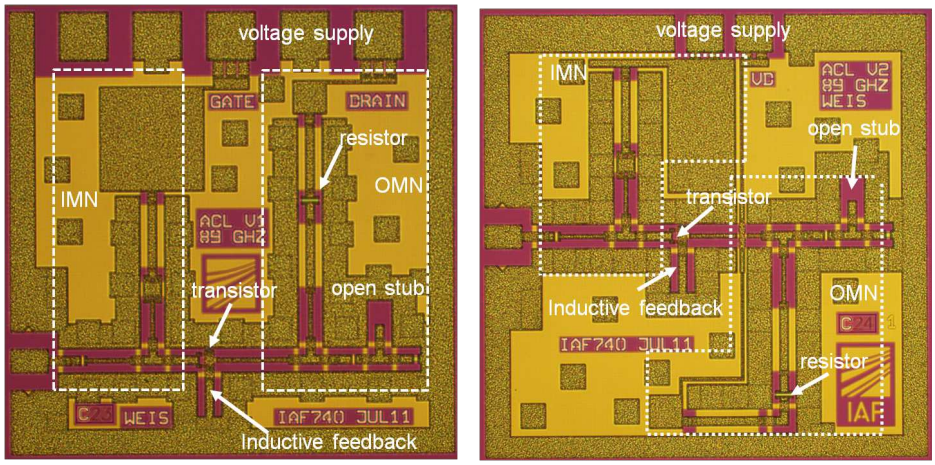

(a) 89 GHz ACL $V1$,variant for ACSS $V1$. (b) 89 GHz ACL $V2$, variant for stand-alone module assembly.

Figure 3.14: Chip photographs of two variants of the first 89 GHz ACL design, measuring a size of 1×1 mm^2, each.

For the OMN of the 89 GHz ACL $V4$ in Figure 3.15, the open stub and the middle one of the parallel capacitors in the DC supply were omitted. The first parallel capacitor was

replaced by a MIM capacitor, yielding a higher capacitance while having a more compact layout. While the lengths of L_{pi1} and L_{po1} are predetermined due to their impedance transforming function and can not be significantly reduced, the size of the elements above was drastically reduced yielding a compact layout. In the IMN of $V4$, all three parallel capacitors were included but reduced capacitance values also allowed a more compact layout.

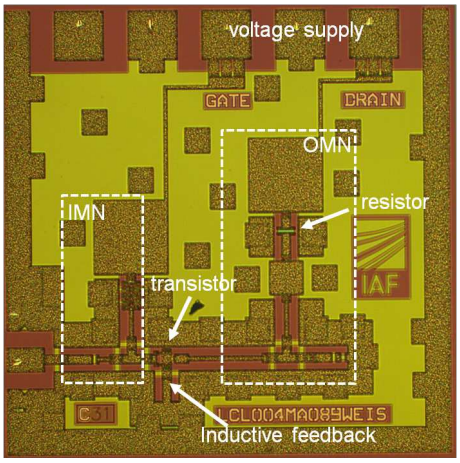

Figure 3.15: Chip photograph of the re-designed 89 GHz ACL for the second wafer run, measuring a size of $1 \times 1\,\mathrm{mm}^2$. This MMIC will be referred to as 89 GHz ACL $V4$ in the following and was integrated into the ACSS $V2$.

In Figure 3.14(b), a variant of the ACL $V1$ is depicted. It has an identical ACL core, including identical values of the components relevant for the matching networks, therefore a very similar performance to ACL $V1$ is expected. The reason for this modification was, to achieve compatibility to a module package that was originally designed for the W-band ACL and AHL. Hence, an additional stand-alone 89 GHz ACL module could be realized. Therefore, the core of the ACL was shifted towards the center of the MMIC to have the signal port in the middle of the side edge. On the IMN side the parallel stub just snugly fits into the available die space. Merely the MIM capacitor needed to be placed next to the parallel stub line. On OMN side however, a mirroring of the parallel stub towards to bottom of the die was necessary. There it was bent with a 90 degree bend towards the vacated space below the inductive source feedback line. A minor adjustment of the stub line length was made to compensate for the bend structure and to have an identical electrical length. In the simulation no difference between ACL $V1$ and ACL $V2$ was observed.

W-band ACL for Active Hot-Cold Load

A further simplification of Equation 3.20 is applied to simulate the noise temperature of the W-band ACL for the Active Hot-Cold Load (AHCL). It is based on the approach of [72] which is valid for a perfect match on drain side of the transistor. Accordingly assuming perfect noise matching on gate side, S_{11}^* equals Γ_{opt} and Γ'_{opt} becomes 0 (see Equation 3.6). As was demonstrated in the previous section, a sophisticated input matching network can achieve a return loss of below $-25\,\mathrm{dB}$ (see Figure 3.11(b)) towards the transistor gate, supporting

this assumption. In this case, the alternative noise parameter T_b equals the theoretical lower noise level $T_{s1,limit}$ of Equation 3.19 and Equation 3.20 can now be written as

$$T_{s1,simp.} = T_{s1,limit} + T_2 \cdot G_{12,ti} \tag{3.25}$$

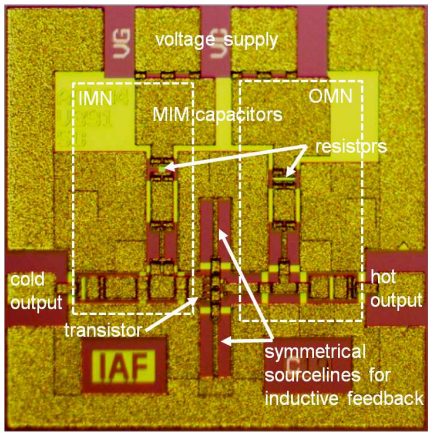

Figure 3.16: Chip photograph of the ACL measuring $0.75 \times 0.75\,\mathrm{mm}^2$. The left-side port provides the cold noise temperature when the right-side port is terminated with $50\,\Omega$.

The resulting circuit is depicted in Figure 3.16 and is in its topology very similar to the 89 GHz ACLs presented above. The series transmission lines on gate side have an impedance of $30\,\Omega$ and the parallel stub which is also used for the DC supply has an impedance of $70\,\Omega$. On the drain side towards the *hot* output $50\,\Omega$ impedance transmission lines are used and the parallel stub is also realized with $70\,\Omega$ impedance. Further differences of this W-band ACL to the above are, that it uses two symmetrical source lines to realize the inductive feedback and that another parallel capacitor in the gate voltage supply line was omitted. More important, however, is that this ACL is realized as a two-port device. This allows on one hand to verify the achieved matching of the output port to a $50\,\Omega$ termination, and to measure the full S-parameter. On the other hand, to implement this circuit into the integrated AHCL presented in Section 3.4.3, where the drain side output is used to generate a *hot* temperature when an appropriate input impedance is present on the gate side terminal. It should be noted, that as a stand-alone device this ACL is not designed to exhibit a *hot* output temperature on drain side. The full S-parameters allow to investigate the influence of the backward gain of the ACL, while for the measurement of the *cold* noise temperature on gate side, the output is terminated with an RF-probe that is connected to a matched calibration waveguide load. Since the *hot* output on the right side of the active load is not terminated with a constant and matched termination as the circuits in Figure 3.14, but when integrated in the AHCL will be confronted with different impedances, both, R_{stab1} and R_{stab2} must be implemented to ensure stability. As previously mentioned, this will slightly increase the cold output temperature.

W-band Active Loads for Switching Calibration Front-End

Based on the generic ACL schematic depicted in Figure 3.13, the novel approach presented in Section 3.3.4 was applied to design the active loads for the SCFE. Expression 3.24 was used to find the optimum design parameters for minimal noise temperature of the circuit.

One of these parameters is of course the length of the shorted source line which generates the feedback inductance. Even the transistor dimension in terms of number and width of the gate fingers can be included and varied in discrete steps. These parameters influence Γ_{opt}. To simultaneously optimize the OMN and IMN, further parameters to vary are the transmission line lengths of L_{si}, L_{so}, L_{pi1}, L_{pi2}, L_{po1}, L_{po2}, L_{stub} as defined in the design schematic in Figure 3.13, and the values of R_{stab1}, R_{stab2}, and of the blocking capacitors. Theoretically, even the line impedance of every single transmission line could be permuted between the discrete possible values $30\,\Omega$, $50\,\Omega$, and $70\,\Omega$. The resulting MMIC is shown in 3.17(a).

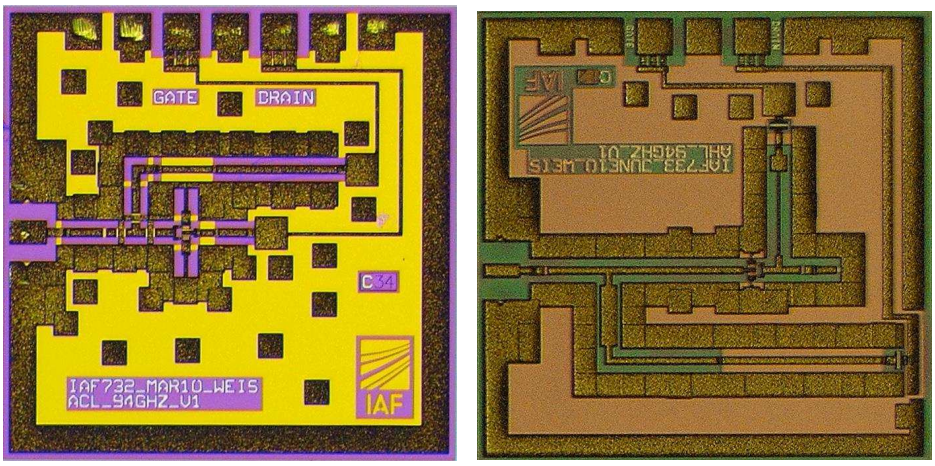

(a) Active Cold Load. (b) Active Hot Load.

Figure 3.17: Chip photographs of W-band active loads, measuring a size of $1 \times 1\,\mathrm{mm}^2$, each.

For the AHL, the approach is very similar. Since the schematic in Figure 3.13 is quite symmetrical in its general form, merely the orientation of the transistor needs to be reversed. This results in the AHL topology shown in Figure 3.18. To maintain consistency in the nomenclature, the IMN is still defined on the left side (drain) and the OMN on the right side (gate). Now, the same optimization routine can be run, except that the new primary design goal is to achieve a *high* noise temperature. A good input return loss of the AHL is of course equally important as for the ACL. Due to the expected high output noise temperature, the absolute power of the noise reflections between the AHL output and the subsequent stages will be higher than for ACLs. However, its influence on the noise measurement accuracy is also less critical. In Figure 3.17(b) a chip photograph of the AHL MMIC is shown.

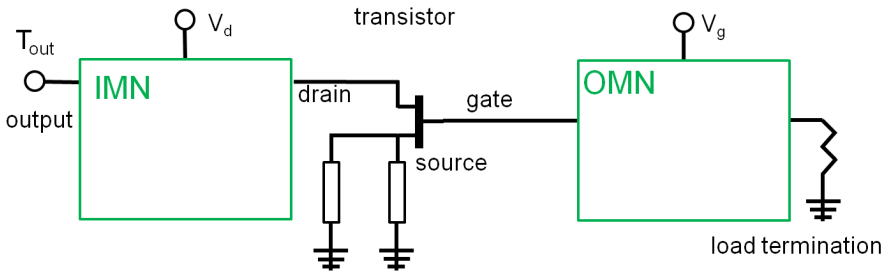

Figure 3.18: Topology of the $94\,\mathrm{GHz}$ AHL.

A drawback of this automated optimization approach is, that the parametric simulation models of capacitors or transmission lines can yield large geometries or line lengths to achieve the optimum values. The parallel capacitor in the IMN of the AHL for example could have been easily replaced by a parallel MIM capacitor, yielding the same capacitance with smaller geometry. Or the conspicuous length of the parallel stub line between the blocking capacitors in the IMN of the ACL, which should have very little influence on the actual matching of the circuit. If the optimizer finds a local gradient towards an improvement of the design goal, it will vary this parameter, even if the absolute influence on the desired noise temperature or matching is small. To facilitate an integration of ACL and AHL in close vicinity to each other in the SCFE presented in the next section, the parallel stubs of the matching networks were bent to run geometrically parallel to the signal line.

3.4 Active Loads with Integrated Switches

With the active loads presented in the previous sections, different circuits are realized that allow to switch between one or two input ports that can for example be connected to a receiving antenna, and two or more internal loads. In addition to active loads, two of the designed circuits also include a passive matched load, just as in a Dicke-radiometer front-end.

3.4.1 Switching Calibration Front-End

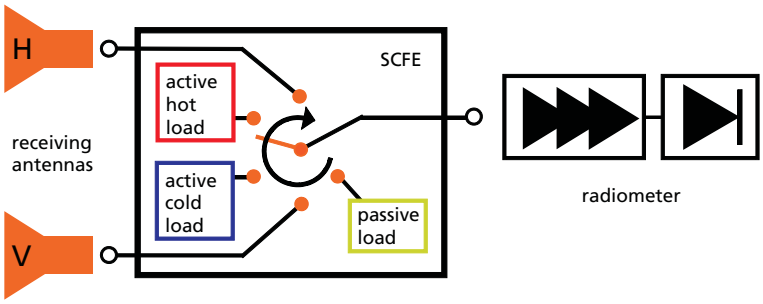

Figure 3.19: Principle operation mode of SCFE and example of application in a polarimetric radiometer system, where the SCFE is placed between the radiometer and the receiving antennas.

The principle operation mode of the SCFE is demonstrated in Figure 3.19. A SP5T switch allows routing the signal from five different sources to a common output port. While two branches are connected to two input ports (e.g. two orthogonal polarized receiving antennas), the three remaining branches are connected to active and passive loads within the same MMIC. The output of the SCFE is connected to the first stage LNA of a radiometer system.

Figure 3.20 shows a chip photograph of the manufactured SCFE MMIC with the dimensions $2 \times 2.5\,\mathrm{mm}^2$. The SP5T is marked by the white dotted area at the right half of the MMIC. The transmission lines from the five signal sources and the output port all intersect at a common star point S , which is marked by an arrow in the photograph. At $\lambda/4$ distance of this point FETs (labeled T_1 to T_5) are placed in shunt to the signal lines (labeled L_1 to L_5). The channel conductance of the transistors can be controlled by the applied gate voltage. For above-threshold bias conditions, the transistor shortens the signal line to ground and the

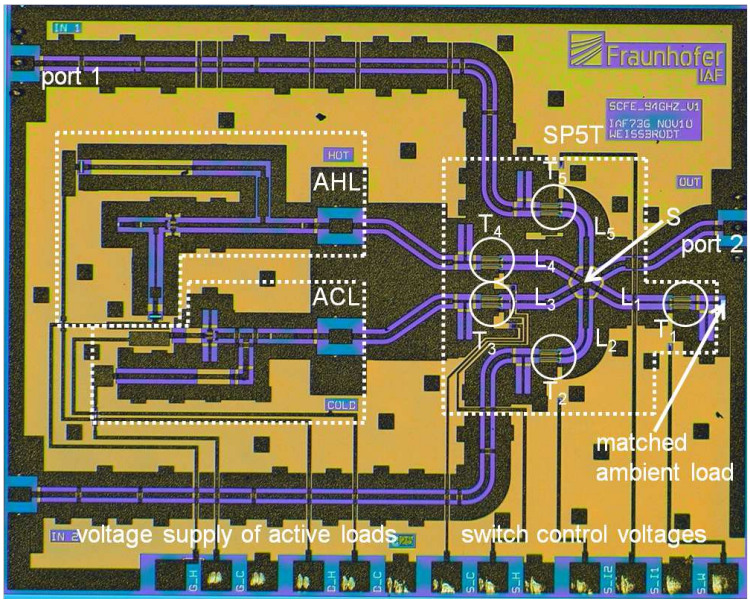

Figure 3.20: Chip photograph of W-band SCFE MMIC with integrated active loads ($2 \times 2.5\,\mathrm{mm}^2$).

short circuit is transformed by the $\lambda/4$-line to an open circuit at the star point S, isolating this specific branch. For sub-threshold bias conditions the FET channel is pinched-off, its parasitic capacitance is compensated by a shorted stub in close vicinity of the FET and the signal is routed to the output [77]. The shorted stub not only compensates for the parasitic capacitance, but also provides power matching and zero drain bias.
Since the function of this type of switches is not dependent on the performance of the FET itself, but on the proper design of the passive circuits, the repeatability and stability of the switching operation is warranted. However, measurements presented in Chapter 5 show, that the correct bias of the FET switches is crucial, to achieve proper isolation between the channels. The switching process involves no mechanics and is not subject to degradation like today's MEMS-based switches still are. Moreover, the switching rate is merely limited by the transistor speed. These facts are crucial for fast, continuous and reliable switching to calibration loads.
At the left half of the MMIC, the ACL and the AHL presented in the previous section (see Figures 3.17) are connected to channel three and four of the SP5T, respectively. Furthermore, a matched ambient load, realized with a $50\,\Omega$ NiCr resistor to ground, is connected to channel one. The two remaining channels are routed to the opposite side of the SCFE output (port 2). This is necessary to allow on-wafer measurements with the VNA setup, where the signal probes are typically placed on opposite sides, while the DC probes are at one or both orthogonal edges. This necessitates very long transmission lines, which of course increase the insertion loss. For the evaluation of the principle SCFE performance this loss can be de-embedded, but for an optional re-design intended for module assembly, these channels would be routed to the top and bottom edge, while the DC-pads would be placed at the left edge.

3.4.2 Active Calibration Sub-System

For the ACSS, an SP3T switch was designed by Mikko Kantanen from *Millilab*. The principal design procedure is similar to SP5T of the SCFE. Again, short circuits to ground at the FETs marked by white circles in Figure 3.21 are transformed to an open circuit at the common star point S, isolating this path from the intended signal path, while the FET of the signal path is open. In contrast to the SP5T, *two* transistors are placed at each branch, which improves the isolation between the channels, but also increases the insertion loss. In the first wafer run, the SP3T was placed as a stand-alone circuit to verify its performance and to estimate how its insertion loss will increase the noise temperature of the ACL. For the second run, the core structure of this SP3T was utilized and its three input ports modified as part of this work to connect to the respective ACL. The goal was to have the least insertion loss on the thru path to have as little influence on the radiometer performance. The second goal was to have symmetrical paths between the ACL and the internal matched load to ensure comparable conditions. The additional loss of the transmission lines and bends to connect the upper path to the ACL also needs to be taken into account. Both ACSS contain the identical SP3T, as can be seen in Figure 3.21, but differ by the integrated ACL version. For ACSS $V1$, the $89\,\mathrm{GHz}$ ACL $V1$ depicted in Figure 3.14(a) was utilized, while the $89\,\mathrm{GHz}$ ACL $V4$, shown in 3.15 was integrated into ACSS $V2$. Chip photographs of both ACSS are presented in Figures 3.21(a) and 3.21(b). As previously mentioned, one of the design goals of ACL $V4$ was to yield a more compact design. In the chip photograph of ACSS $V2$ it can be seen, that some space above the ACL is not used (except for the generously placed MIM capacitors). It would have been possible to reduce the size of the die by $0.25\,\mathrm{mm}$ of the longer edge length. However, to allow compatibility between the two ACSS versions in terms of module packaging, the dimensions of ACSS $V2$ were kept identical to ACSS $V1$.

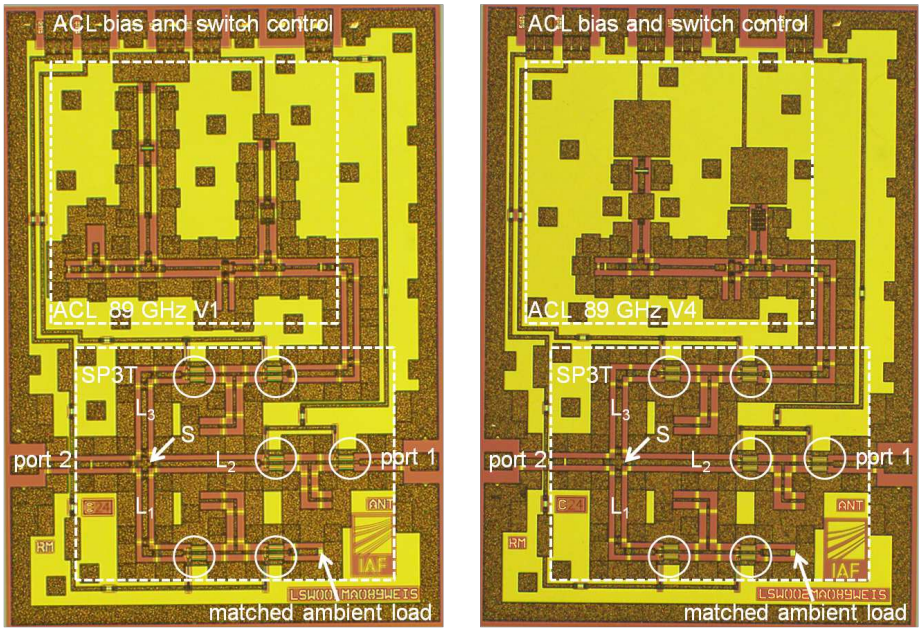

(a) $89\,GHz$ ACSS $V1$.

(b) $89\,GHz$ ACSS $V2$.

Figure 3.21: Chip photographs of the two $89\,\mathrm{GHz}$ ACSS versions, measuring a size of $1.75 \times 1.25\,\mathrm{mm}^2$, each.

3.4.3 Active Hot-Cold Load

As shown in the AHL in Section 3.3.6, the drain-connection of an ACL can be used as an active *hot* load. Contrary to the approach of the SCFE with two separate active loads, the main idea for the AHCL is to use only *one* noise-source and to switch between the two ports of the source to realize a cold *and* hot load. Although an additional transistor is needed to route the signal and the total number of transistors remains constant, only one transistor operates as active device. This leads to a reduction of the DC power dissipation by half. Moreover, only one transistor has to be power-matched, which allows for the reduction of chip-size, that is dominated by the transmission lines needed for the routing of the signal and impedance-matching.

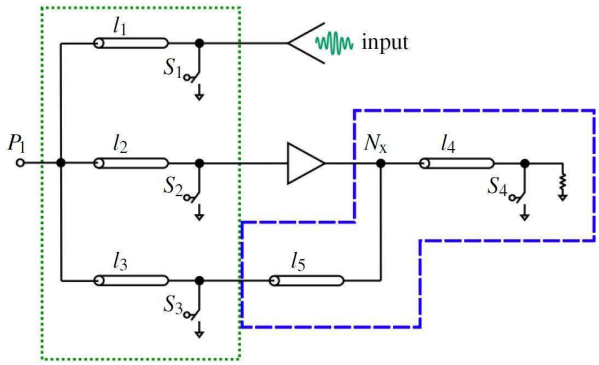

Figure 3.22: Schematic representation of the integrated AHCL. The dotted green box and dashed blue boxes frame the SP3T and the additional switching network, respectively. The Triangle stands for the transistor circuit operating as hot and cold load.

The schematic of the integrated AHCL is shown in Figure 3.22. The AHCL has two RF-ports - the left port ($P1$) is the output port going to the radiometer. The upper right port is connected to the receive antenna. The core of the AHCL is the ACL, which is illustrated by the amplifier symbol. Internally, the left and the right side of it are connected to the gate and drain of the ACL, respectively. The routing of the signal is done by a SP3T switch, which is marked by the green dotted box. The SP3T makes use of three transistor-switches ($S1$, $S2$ and $S3$) and three $\lambda/4$ length transmission lines ($l1$, $l2$ and $l3$). The behavior of the AHCL can be changed by a variation of the control voltage of these three switches and one additional switch ($S4$) on the drain side of the transistor. Three switching configurations exist, that are described in the following:

- **Receive:** When $S2$ and $S3$ create a short, the transmission lines $l2$ and $l3$ transform the short into an open and isolate the branches from $P1$. When in addition to that, $S1$ is biased to provide a through, the signal can travel from the input port to the output port $P1$, without being influenced by the other branches.

- **Cold:** The additional switch $S4$ is required to provide a $50\,\Omega$ termination to the ACL in the cold-load state, and to isolate this termination in the hot-load state. When $S1$ and $S3$ are biased to provide a short and $S2$ and $S4$ are biased for a through, the output port $P1$ is terminated with a low noise load. The short generated by $S3$ is transformed by the transmission line $l5$ with a length of $3/4\lambda$ into an open at node

Nx. The AHCL in cold operation has the same performance as the stand-alone ACL, with the difference that its noise temperature is increased by the SP3T losses.

- **Hot:** The hot load termination is realized, when $S1$, $S2$ and $S4$ are biased for short and $S3$ is biased to provide a through. In that case, the $\lambda/4$ length transmission line $l4$ transforms the $S4$-short into an open at node Nx and isolates the $50\,\Omega$ termination. This is necessary since it would otherwise decrease the noise temperature of the active hot load. In this switching configuration, the AHCL noise temperature cannot be described by Equation 3.25, which mandates matching of all ports. Thus, according to [72], and [71], the hot noise temperature will be dominantly dictated by the power generated in the transistor output, the amplified noise adjacent at the transistor input and by the noise power reflected at the transistor output.

Table 3.4 summarizes the switching states and the resulting AHCL behaviour at the output port.

Table 3.4: Biasing configurations of the AHCL switches for the desired output signal.

	Switch state			
Output signal	**S1**	**S2**	**S3**	**S4**
Receive	Through	Short	Short	N/A
Cold	Short	Through	Short	Through
Hot	Short	Short	Through	Short

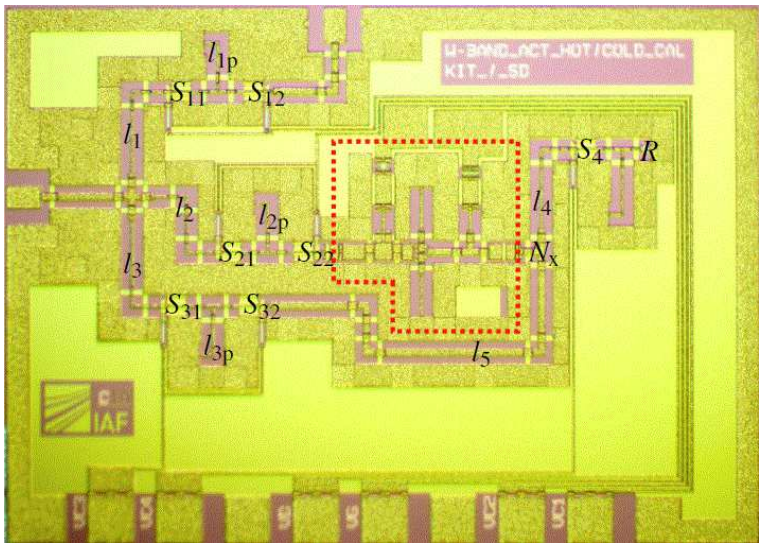

Figure 3.23: Chip photograph of the AHCL having a size of only $1.75 \times 1.25\,\mathrm{mm}^2$. For radiometer application, the left port is the output for radiometer connection and the top port is for receive antenna connection.

Again, the implementation of the SP3T on the MMIC is equivalent to the procedure described for the ACSS and the SCFE. Figure 3.23 shows the chip photograph of the developed AHCL. The nomenclature of the lines and switches in the photograph correspond to the one

used in the above schematic. As for the ACSS, to improve isolation *two* switching transistors were placed at each branch, marked as S_{x1} and S_{x2} in the photograph. The shorted $70\,\Omega$ stubs, that compensate for the parasitic capacitance are placed between the two transistors in each branch and marked as l_{xp}. The three $\lambda/4$ lines with $70\,\Omega$ impedance all intersect at a common star point and the respective path is routed to output port of the AHCL at the left edge. The core of the AHCL, marked by the red dotted box, is the ACL previously depicted in Figure 3.16 with its drain side output connected to the node Nx. For the switching network to the right of the ACL, only one shunt FET was used, since a low insertion loss at this point has priority over isolation. The $50\,\Omega$ load is marked R in the figure.

For the developed circuits of active loads with integrated switches presented in this section, a patent was granted [78].

3.5 D-Band Active Cold Loads and Low-Noise Amplifier

ACLs were also designed in D-band to push the state of the art to the limit and to demonstrate that the concept of active loads is still feasible in this frequency range. However, as will be presented in the next chapter, the requirements for active loads characterization are particularly challenging. Especially the low noise performance and good input return loss of the first amplifying stage in the measurement setup is essential. Due to limited commercial availability of appropriate LNAs in D-band, a dedicated broadband LNA MMIC was designed as part of this work [79].

D-band ACLs

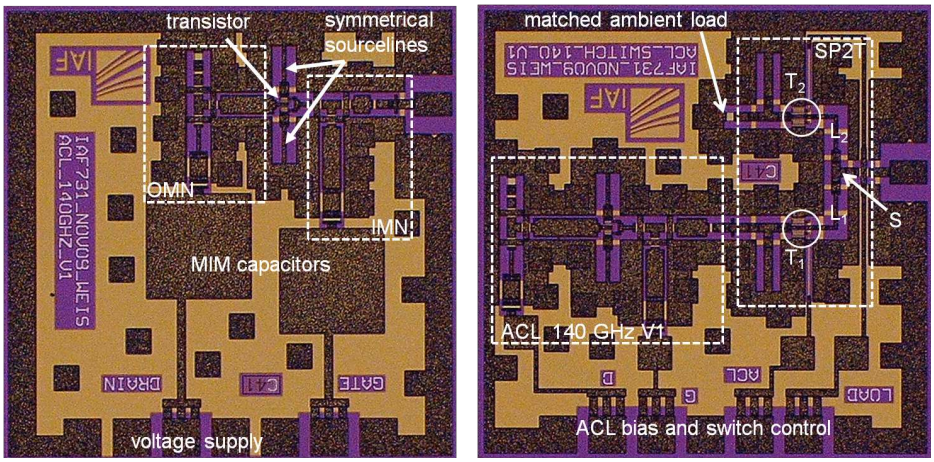

(a) D-band ACL.

(b) D-band ACL with integrated SP2T and matched load.

Figure 3.24: Chip photographs of D-band MMICs, measuring a size of $1 \times 1\,\mathrm{mm}^2$, each.

For the design of the D-band ACLs the same principal topology was used as for the W-band circuits. The layout of the $140\,\mathrm{GHz}$ ACL $V1$ can be seen in the chip photograph in Figure 3.24(a). Parts of the signal line and the parallel stub line of the IMN were realized

with $30\,\Omega$ line impedance, while the parallel stub line of the OMN was realized with $70\,\Omega$ line impedance. For stability at these high frequencies, NiCr resistors were placed in both DC supply paths, accepting the increase of noise figure associated with that. For the inductive source feedback, two symmetrical $70\,\Omega$ line are used. For the termination of the OMN, the signal path is divided by a T-structure into two parallel transmission lines, of which one is necessary for the power supply and the other to connect to the $50\,\Omega$ termination. This layout change was necessary to allow the integration with a SP2T switch into a very compact die, which is shown in Figure 3.24(b). The left white dotted rectangle marks the ACL core as seen in Figure 3.24(a), merely with smaller MIM capacitors in the DC supply lines, due to the restricted space. The right white dotted rectangle marks the SP2T with its two shunt FETs $T1$ and $T2$ and the two $\lambda/4$-lines $L1$ and $L2$, that connect at the star point S. The principal functionality is identical to the one explained for the SCFE. The performance of the SP2T at D-band frequencies was demonstrated in [80] by the implementation as a Dicke-switch into an LNA MMIC. As for the switching references presented in Section 3.4, the SP2T allows to switch between a passive matched load at ambient temperature and the ACL.

D-band LNA

D-band LNAs, using IAF's mHEMT process with $100\,$nm and $50\,$nm gate length were published in [81] and achieved noise figures on MMIC level as low as $3\,$dB, but in a very narrow bandwidth around $130\,$GHz. For the purpose of covering the frequency range of noise measurement setup presented in the following section, the goal of *this* LNA design was to achieve a broadband good noise performance [79]. The LNA was designed using transistors with $35\,$nm gate length. This mHEMT process exhibits a channel electron mobility μ_0 and a channel electron density n_e as high as $9800\,\mathrm{cm}^2/\mathrm{Vs}$ and $6.1 \cdot 10^{12}\,\mathrm{cm}^{-2}$, respectively. The maximum extrinsic transconductance $g_{m,max}$ is $2500\,\mathrm{mS/mm}$ and a transit frequency f_T of over $500\,$GHz is achieved [57]. The chosen topology is a four-stage design in common source configuration with gate widths of $2 \times 15\,\mu$m, each. Inductive source degeneration with symmetric $30\,\Omega$ transmission lines was used to increase stability and improve noise behavior [68]. This is especially important at the first stage. $50\,\Omega$ GCPW lines are used to connect the four transistors and series capacitors placed between the stages to decouple the DC bias. The input and output matching as well as the inter-stage matching is achieved with parallel stub lines with $30\,\Omega$ and $50\,\Omega$ impedance. These stub lines are also used to provide the DC bias. A serial NiCr resistor and two parallel capacitors in each stub line are placed to decouple the RF signal from the DC source. The first two and the second two stages of the LNA can be biased separately at the DC pads at the upper edge of the MMIC. A schematic of the LNA is shown in 3.25 and a chip photograph is depicted in Figure 3.26.

Figure 3.27 shows the manufactured LNA MMIC mounted into an open split-block module. The module is equipped with an integrated programmable DC-control board. Note, that the chip layout allows the first two transistor stages and the subsequent two stages to have separate DC-supplies. While all four transistors are operated with the same gate voltage in the module, the DC-control board allows to allocate different drain voltages for the first two and the subsequent two stages. This permits to fine-tune the LNA for optimum gain-to-noise-ratio. Gold bond wires are used to connect the signal port pads to microstrip lines and the DC pads to external pads on a PCB. The microstrip lines are processed on a quartz substrate and terminated with feeding patches on the waveguide side. The waveguide routes

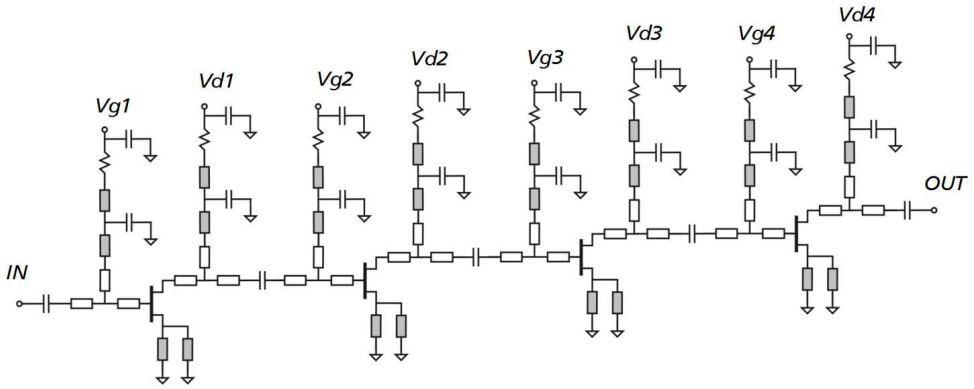

Figure 3.25: Schematic of D-band LNA.

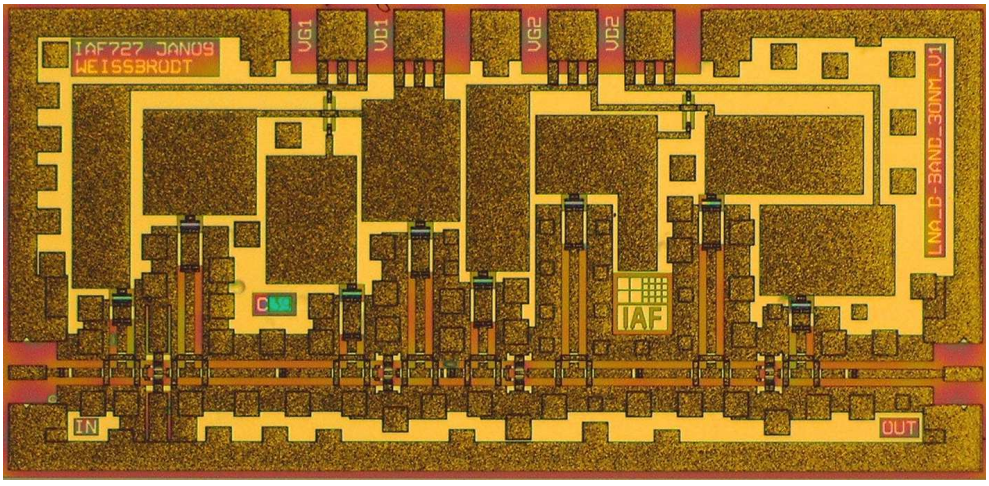

Figure 3.26: Chip photograph of the processed D-band LNA MMIC ($2 \times 1\,\mathrm{mm}^2$) with grounded coplanar waveguide transmission lines and large on-chip capacitors.

the signal in a 90 degree bend to the external standard flanges on opposite sides of the LNA module. The complete module can be seen in Figure 4.15 as part of the D-band noise measurement setup presented in the following chapter.

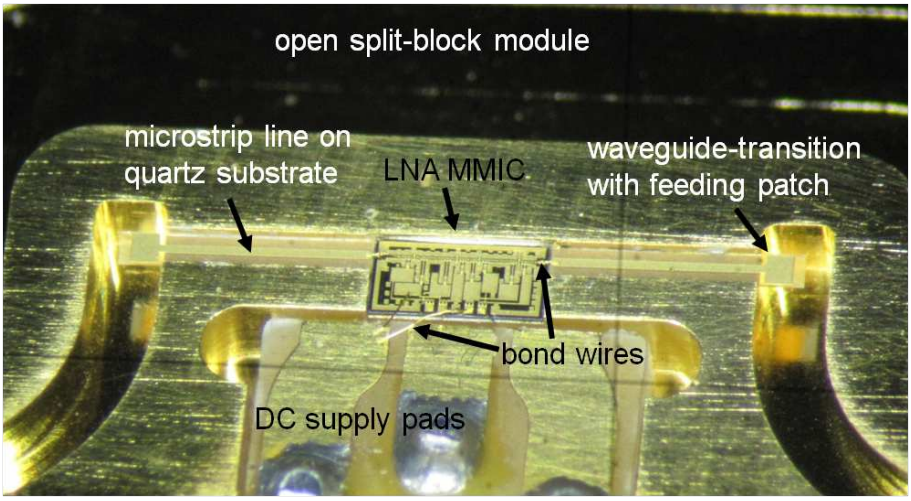

Figure 3.27: View of an open D-band split-block package with mounted LNA MMIC and transitions to waveguide.

Summary and Conclusion

After frequency considerations and the introduction of the utilized technology, the main emphasis of this chapter was the design of stand-alone active loads and active loads with integrated switches. For that, different simulation approaches and design-flows were compared to each other and several MMICs in W-band and D-band were designed for manufacturing. It was shown, that the general design-flow is very elaborate, iterative and time-consuming, so that other authors have already investigated simplified approaches. This work has demonstrated a way to effectively make use of today's numerical computation methods. Based on the transistor and passive components models and ADS features, a very direct calculation method of the noise temperature was presented, that allows to apply automated optimization algorithms. By that, the normal optimization effort was drastically reduced.
The designed circuits were manufactured but before they can be characterized, an appropriate measurement setup needs to be evaluated and assembled. This will be discussed in the following chapter.

4 One-Port Noise Measurement Setups

For the characterization of the designed MMICs presented in the previous chapter, several noise temperature measurement approaches were investigated as part of this work. Possible error sources were analyzed analytically and different measurement methods experimentally tested. The findings concluded in two dedicated one-port noise measurement setups for W- and two for D-band, which are presented in this chapter. The measurement results achieved with these setups, are demonstrated and compared in Chapters 5 and 6. In addition, some of the W-band circuit- and module measurement results were verified by measurements of third parties. The setups used by *Radiometer Physics GmbH* (RPG) and *Millilab* for this purpose are also shortly introduced in this chapter.

4.1 Noise Figure Measurements

For a better understanding of the following discussion about the components and factors that influence the measurement setup, a schematic diagram of the finally established setup is shown beforehand in Figure 4.1. All of the components illustrated in this schematic will be discussed in this chapter and a detailed description of the final setup will be given in Section 4.4.

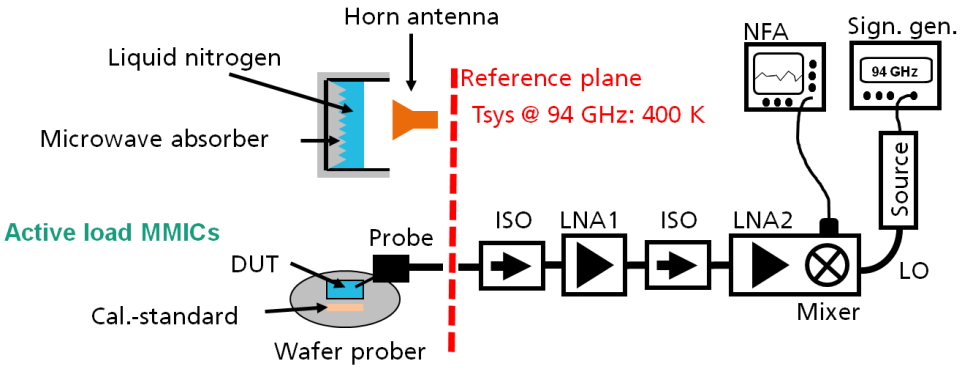

Figure 4.1: Setup of custom on-wafer measurement system for one-port noise measurements.

To distinguish the task of measuring the absolute noise temperature of a one-port noise source from the prevalent procedure of noise figure measurements, it is important to introduce some common fundamentals. The noise figure measurement of a two-port DUT is straightforward and well explained in numerous textbooks and application notes. However, requirements increase with frequency, while the availability of accurate measurement equipment drastically decreases. The common definition of noise figure was introduced in [82]

as the ratio of the signal-to-noise ratio (SNR) at the *input* of a network to the SNR at the *output*:

$$NF = 10 \cdot \log_{10}(F) = 10 \cdot \log_{10}\left(\frac{SNR_i}{SNR_o}\right) \tag{4.1}$$

It is common to differentiate between noise factor F, which is the linear ratio, and the noise figure NF, which is the decadic logarithm of the noise factor with the unit dB. The relation between noise figure and noise temperature was already introduced in Equation 3.1. The SNR is deteriorated by the added noise N_a of the device, which becomes evident when transforming Equation 4.1 into

$$F = \frac{S_i/N_i}{S_o/N_o} = \frac{S_i/N_i}{GS_i/(N_a + GN_i)} = \frac{N_a + GN_i}{GN_i} = \frac{N_a + kT_0BG}{kT_0BG}, \tag{4.2}$$

where G is the gain of the DUT, k the Boltzmann constant, and B the bandwidth. Hereby, one fundamental difference to the presented one-port noise measurements setups becomes obvious. The investigated DUTs have no gain G and no input signal S_i, but only exhibit an inherent noise which is the quantity of interest to be measured. The lack of gain in the DUT is a crucial challenge in the accuracy of the one-port noise measurements. While the gain of typical DUTs like LNAs drastically reduce the influence of the measurement setup's own noise figure and mitigate the requirements, the noise contribution of the setup in one-port measurements is particularly critical. To make things worse, the expected noise temperature of the DUT is considerably lower than the one of the measurement setup itself. Because all errors in the determination of the measurement system's noise figure are introduced into the results, a thorough characterization of the setup is necessary. This is done by the Y-factor method, which is basically the same procedure as the calibration of radiometers described in Section 2.

Y-factor Method

The Y-factor method is the basis of most noise figure measurements, whether they are manual or automatically performed internally in a noise figure analyzer [83]. The Y-factor is the ratio between two measured power levels at the output of the system with two different noise levels at its input.

$$Y = \frac{N_2}{N_1} = \frac{N^{ON}}{N^{OFF}} \tag{4.3}$$

Due to the ratio, the absolute power level accuracy of the measuring device is not important. The relative level accuracy within the noise figure analyzer (NFA) however, is fundamental and requires very linear internal power detectors.
In addition to the measured noise levels and the calculated Y-factor, the excess noise ratio (ENR) of the two input noise levels needs to be known in order to calculate the system noise figure. For commercially available noise measurement setups, the NFAs come with a calibrated noise diode as a noise source and include the ENR table either stored internally or provided as hard-copy. In this case the measured noise levels in the above described Y-factor correspond to the noise source being turned *ON* and *OFF*. In general, the ENR can be calculated for any two noise temperatures at the input by

$$ENR_{dB} = 10 \cdot \log_{10}(ENR) = 10 \cdot \log_{10}\left(\frac{T_h - T_c}{T_0}\right), \tag{4.4}$$

where T_h is the *hot*, T_c the *cold* noise temperature, and T_0 equals as always $290\,\mathrm{K}$. Note, that therefore an ENR of $0\,\mathrm{dB}$ still describes a noise temperature difference of $290\,\mathrm{K}$ between hot and cold. Furthermore, it should be noted that suppliers, when providing the ENR table for their noise diode, assume that the physical temperature of the noise source during measurement is T_0. Which leads to $T_c = T_{ND}^{OFF} = T_0$. In many cases laboratory conditions differ from this assumption and the error needs to be corrected.
With the measured Y-factor and the known ENR of the noise source, the system noise factor can be easily calculated [84], using

$$F_{sys} = \frac{ENR}{Y - 1} \tag{4.5}$$

Errors in the ENR of the noise source are a major source of measurement uncertainty in noise figure measurements. In some cases, the uncertainties are similar to the measured quantities [85]. As can be derived from Equation 4.5, any ENR error transfers directly to the noise figure [86]: $NF = ENR_{dB} - 10\log_{10}(Y - 1)$. This applies of course also for noise sources other than noise diodes. Especially errors during calibration with the hot and cold references will inflict subsequent errors during measurements. However, errors can be reduced by carefully choosing the proper noise source for this measurement method and especially for this kind of low-noise one-port DUT. Depending on the characteristic of the DUT, either a high or low ENR is advantageous [87]. This will be discussed in Section 4.2.

To better understand the implications of the Y-factor and the ENR on the performance of the measurement setup, Figure 4.2 depicts the parameters, that influence the slope and the range of the two-point curve. This curve characterizes the setup and is defined by the choice of the measurement setup components and hot and cold references. It is important to understand this graph, since during the evaluation of components and references in the following sections, it will repeatedly be referred to.

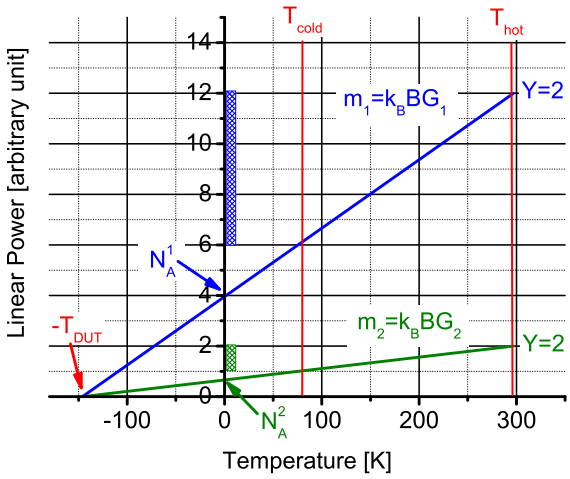

Figure 4.2: Diagram showing the Y-factor variables.

The blue and the green lines in Figure 4.2 are exemplary for two different measurement setups. Both curves are determined by using the same references $T_c = 77\,\mathrm{K}$ and $T_h = 298\,\mathrm{K}$ which are plotted on the x-axis. The y-axis represents the measured noise power at the NFA on a linear scale. Obviously, the slope m of the curve determines in which power measurement range of the NFA the signal is received. The slope m, in turn, is dependent on the total (conversion) gain of the components between the DUT or the references and the NFA. The two exemplary curves and the numbers in the diagram are chosen on purpose, to point out one crucial fact: If the Y-factor for both curves is calculated by applying Equation 4.3, it becomes evident that both measurement setups have the same Y-factor (in this example $Y = 2$). Furthermore, they both were characterized with the same references T_c and T_h, yielding an identical ENR. According to Equation 4.5 this means, that they both have the same system noise figure F_{sys}. This can also be concluded from the fact that both curves intersect with the negative x-axis at the same point, which is the negative system noise temperature (or in general $-T_{DUT}$). What needs to be pointed out here is, that two setups, though having the same system noise figure, can *project* the same temperature range in different power measurement ranges of the NFA, which are marked blue and green at the y-axis in Figure 4.2. This, however, can have a major influence on the accuracy of the measurement, as will be discussed in the following sections.

Second-Stage Effect

During the typical noise figure measurement procedure of a two-port DUT, first the measurement system is characterized by connecting the noise source directly to the system. This results in the noise factor F_2 of the measurement system alone. After that, the DUT is placed between the noise source and the measurement system and the combined noise factor F_{sys} of *both*, DUT and system, is measured. In analogy to the Friis formula [82], the cascaded noise factor can be rewritten to find F_1, the noise factor of the DUT:

$$F_1 = F_{sys} - \frac{F_2 - 1}{G}, \tag{4.6}$$

where G is the gain of the DUT. It is obvious, that if the gain of the DUT is sufficiently high, the so-called second stage contribution of the measurement system will be small and can be neglected. If not, a second stage correction should be performed, which is typically done automatically by the NFA. As previously pointed out, the DUTs in this work exhibit no gain. Nevertheless, this automated correction is not possible, because, due to the nature of a one-port DUT, the noise source can not be connected to the *input* of the DUT. Therefore, the combined noise factor F_{sys} in Equation 4.6 can not be measured with the Y-factor method and it is not possible to perform an automatic second stage correction.

4.2 Evaluation of Hot and Cold References for Y-factor Measurements

4.2.1 Noise Diode

Noise diodes (ND) typically provide a high level of ENR, which is desirable in many applications. If the noise figure of the DUT is much higher than the ENR, the device noise

tends to mask the noise source output. In this case the Y-factor will be very close to 1 and accurate measurements of small ratios become difficult. As a rule of thumb, the noise figure should not be more than $10\,$dB above the ENR of the noise source [83]. So in general, a high ENR is beneficial, when *not* measuring very low-noise devices. On the other hand, it is recommended to use low ENR whenever possible, especially when the DUT has a very low noise figure.
The following paragraph is cited from *Keysight*'s application note [87]: "A low ENR noise source will minimize error due to noise detector non-linearity. This error will be smaller if the measurement is made over a smaller, and therefore more linear, range of the instruments detector. [...] A low ENR noise source will require the instrument to use the least internal attenuation to cover the dynamic range of the measurement, unless the gain of the DUT is very high. Using less attenuators will lower the noise figure of the measurement instrument, which will lower the uncertainty of the measurement."

Referring to the diagram in Figure 4.2, this not only means, that T_c and T_h need to be carefully chosen, but also, that it is not necessarily beneficial to have the *highest possible* gain in the measurement setup. This will be further discussed in Section 4.4. Available noise diodes for the setups in W-band and D-band were the NC5110 from *NoiseCom* with an ENR varying between 9 and $20\,$dB over the band and the ISSN-06 from *Elva* with an ENR of $11 - 15\,$dB, respectively. Due to the previously cited guideline, most manufacturer of noise diodes boast about the high ENR their diodes can provide. But an ENR of $15\,$dB corresponds to a noise temperature of almost $9000\,$K, which is far above the expected noise temperature of the DUTs in this work. Since the measurement setup's gain is optimized to measure the very weak noise power of the ACL - as will be explained in Section 4.4 - this would drive the setup into saturation or cause the NFA to automatically switch to higher internal attenuation to prevent this.
As previously mentioned, it is necessary to regularly have the ND re-calibrated by the supplier to reduce ENR uncertainties. Typically, in data sheets of ND the nominal ENR and the ENR flatness over the frequency band are provided. Sometimes also the voltage standing wave ratio (VSWR), and the stability over temperature or time are provided [88], [89]. What typically is *not* provided is the *accuracy* of the delivered ENR table after the (re-)calibration. On specific request after a commissioned re-calibration, the distributor of *Elva* NDs forwarded the information from the manufacturers engineers, that the estimated accuracy of the ISSN calibration is $\pm 0.5\,$dB for W-band and $\pm 1\,$dB for D-band [90]. As we remember from Equation 4.5, this uncertainty directly transfers to the calculation of the noise temperature, resulting in an additional error of $\pm 35\,$K and $\pm 75\,$K in W-band and D-band respectively. This relatively large error is due to the fact, that the method used to determine the ND's ENR is to calibrate it versus hot and cold standards, just like the ones presented in the following sections. Since the slope of the hot cold calibration curve is defined over a small temperature range (typically between 77 and $373\,$K) this introduces a significant extrapolation error at the ND's temperatures around several thousand Kelvin. This is less critical when measuring DUTs with NF in the vicinity of the ENR, because the same error is inevitably introduced when characterizing such DUTs directly with hot cold standards. But when using NDs to measure a very low noise DUT, a *second* extrapolation error is introduced. In this case other references than a noise diode are preferable, which encompass the expected noise temperature

of the DUT. Such references will be presented in the following. Another disadvantage is the large impedance change of the ND when switching between the *ON* and *OFF* state, which is partially counteracted by incorporating an isolator. But again, the passive references presented in the following (waveguide loads and antennas) are advantageous, because of their negligible impedance change between hot and cold.

4.2.2 Cooled or Heated Waveguide Loads

Matched passive loads emit a noise temperature equivalent to their physical temperature. So a very straightforward way is to cool or heat standard waveguide calibration loads to use them as cold and hot references. By this, either cold and ambient, ambient and hot, or cold and hot loads can be generated to create a two-point calibration curve.

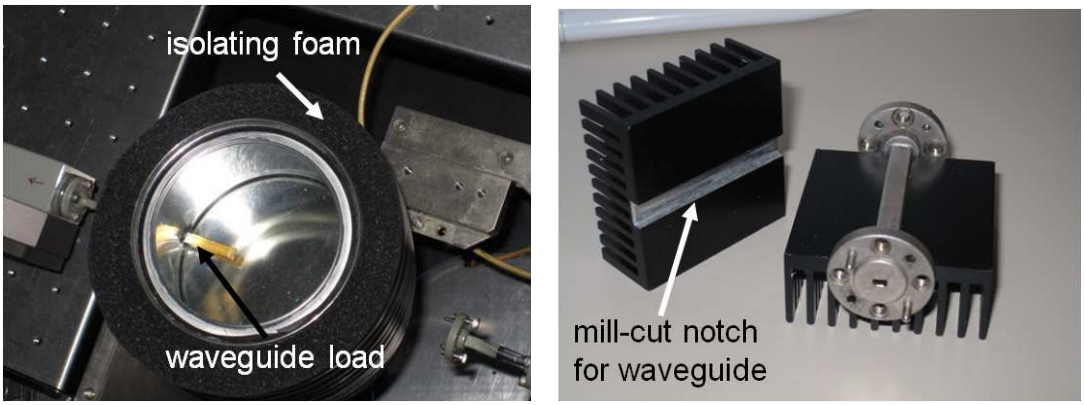

(a) Container for liquid nitrogen with integrated waveguide load.

(b) Dissipator for thermal decoupling.

Figure 4.3: Components for setup with cooled waveguide matched load.

Cooled Waveguide Load

A waveguide matched load was soldered into the outer casing of a container so that the load is inside the container and the standard waveguide flange outside can be connected to the measurement system (see Figure 4.3(a)). Now the container can be filled with liquid gas. The use of liquid gases as a cold reference is based on the fact that its boiling temperatures are well defined and known. For the commonly used liquid nitrogen (LN) this temperature is at 77 K. The Container was thermally isolated with foam to minimize boiling of the LN. A thermal equilibration needs to be awaited, even though the boiling itself is not as critical as if looking with an antenna from above into the LN as presented in the next section. However, thermal conductivity of the waveguide is a massive error source. In both directions: the first stages of the measurement setup consequently get cooled down, while the thermal capacity of the measurement system leaks into the container to the matched load and avoids that it can be cooled down to the actual temperature of the LN. The main problem with this is, that no *stable* and *defined* temperature at any reference plane of the setup can be achieved. A possible solution is to monitor accurately the temperature along the waveguide with several sensors, modeling the heat flow and to extract afterwards the error from the measurement results. A more practical approach is the use of a piece of

stainless steel waveguide instead which has notable lower thermal conductivity as copper or brass. Also, one solution presented in [91], was to physically separate the waveguides and leave an isolating air gap between two flanges. However this has a massive filtering effect, so that the distance of the gap and additionally needed structures to compensate for the effect need to be modeled and simulated and the customized interconnection needs to be manufactured. For the evaluated setup in this work, the heat flow was strongly reduced by the use of a customized heat dissipator as depicted disassembled in Figure 4.3(b). When assembled, it sourrounds a piece of waveguide and the thermal conductivity is optimized by conductance paste. In the measurement setup it is placed between the waveguide flange of the matched load in the cooling container and the first stage isolator of the receiver. A fan, pointed at the dissipator, amplifies the convection and pulls the temperature of the cold waveguide towards the ambient temperature. By this, a thermal barrier is generated between the physically cold waveguide load and the measurement receiver. In Figure 4.4 the effect of this barrier can be observed: while the condensed air humidity generates a layer of frost on the waveguide bend left of the dissipator, the isolator on the right was only slightly colder than the ambient temperature.

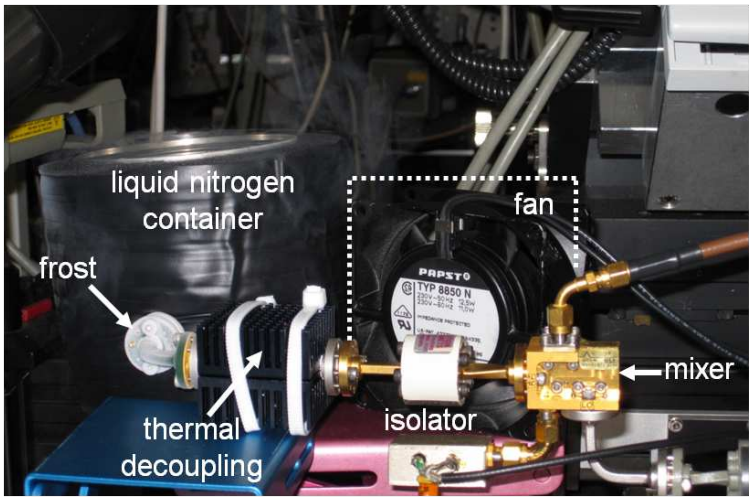

Figure 4.4: Setup for measuring with cooled waveguide load.

However, a residual heat transfer and therefore an influence on the receiver can not be prevented by this method. Whatever action is taken to minimize the thermal conductivity along the waveguide, it can not be avoided, that the air exchange *inside* the waveguide due to the temperature gradient leads to a heat flow. Furthermore, this leads to condensation *inside* the waveguide, which of course has an unpredictable influence on the wave propagation inside the waveguide. Therefore, this option was not chosen for the calibration of the final measurement setup.

Heated Waveguide Load

When in contrast heating the waveguide load, the issue of condensing air humidity is omitted. In addition, from a practical and safety point of view, it is not as challenging as the handling with liquid gases. However, the heat transfer issue remains and has an influence on the receiver. Furthermore, the achieved ENR is limited by the fact that a waveguide load should not be heated to more than $100\,^{\circ}\mathrm{C}$ to avoid damage of the load.

4.2.3 Artificial Black Body

The concept of an artificial black body was introduced in Section 2.2. A microwave absorber is used to radiate a defined brightness temperature, depending on its own physical temperature. Connecting an antenna to the front-end of the measurement system and facing it towards the absorber, the setup can be calibrated with two known absorber temperatures, just as a radiometer. The necessary components for this procedure are presented in the following.

Microwave Absorber

The absorber used as an artificial black body was unpainted pyramidal *C-RAM* from *Cuming Microwave* [92]. It is a high performance broadband absorber from specially treated low density polyurethane foam, which is typically used for anechoic chambers. Even though it is only characterized up to 50 GHz by the manufacturer, yielding a typical reflectivity of -50 dB at normal incidence, it is known to provide premium performance even at higher frequencies and off-normal incident angles. An extensive investigation of similar pyramidal absorber was performed up to 600 GHz in [93] and confirmed its usability. Furthermore, the absorber foam is resistant to cold temperatures like being soaked in LN. Therefore it can not only be used as an ambient load, but also as a cold load.

Antenna

To calibrate the measurement setup with hot and cold microwave absorber, an antenna needs to be connected to the measurement system front-end. This has the inherent advantage, that by the physical separation of the measurement system and the loads, the previously described issue of heat transfer and thermal conductivity is practically solved. Another notable advantage of this approach is, that in contrast to noise diodes, the antenna impedance does not change between the hot and cold state. The return loss of the antenna is in fact a very crucial parameter that will be discussed in Section 4.3. The influence of the ohmic resistance of the antenna, however, is only negligible as long as it is at the same temperature as the measurement system. This is typically the case, but when working with LN as described in the following, some precautions must be taken. The beam efficiency of the antenna might have some influence but is not critical because it is assumed, due to the setup's geometry, that from any relevant receiving angle the same temperature is seen. In [50], the optimal distance between a horn antenna and cold target is stated to be in the range of $8 - 8.5$ cm for the test-beds at 23.8 GHz and 36.5 GHz. For the investigated setups in W-band and D-band, a similar distance was found to be optimal with a corrugated horn antenna. The main influence is thus not directly dependent on the frequency, but on the measurement setup geometry. This was experimentally confirmed and applied for the setups used in this work.

Liquid Nitrogen

Having the two previously described components at hand, the measurement of the ambient reference temperature is straightforward. To generate a cold reference target, the absorber needs to be cooled with LN. To achieve reliable results, many details need to be taken into

account. In the applied setup, the LN was filled into a Dewar vessel which was covered with absorber pyramids at the bottom. When pouring the liquid nitrogen into the Dewar vessel this results in a strong evaporation, due to the high temperature difference. Temperature equilibration needs to be awaited, so that the surface of the LN becomes flat. The air temperature inside the Dewar vessel in the space between the upper edge of the vessel and the LN surface becomes significantly cold. Therefore it needs to be taken care of, that the antenna does not immerge into that space, but is above the edge of the Dewar. Only then the thermal isolation is ensured and the ohmic resistance of the antenna does not influence the calibration result. Figure 4.5 illustrates such a setup geometry.

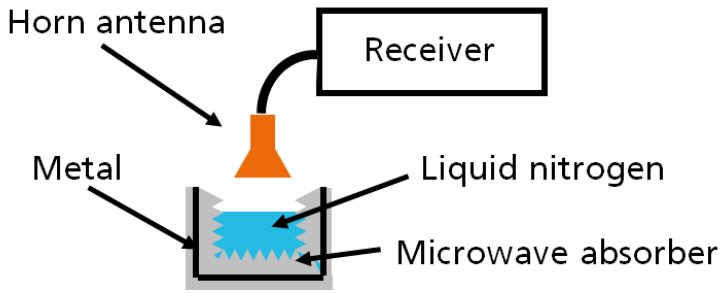

Figure 4.5: Utilized setup for the measurement system calibration with liquid nitrogen.

Due to the small opening angle of the main lobe of the antenna and the reduced side-lobes, this arrangement is not critical. Furthermore, the outer casing of the Dewar is made of metal. This way all unwanted radiation that would leak from any angle from above into the vessel would be reflected into the absorbing bottom. On the other side, any side-lobe of the antenna is pointed at a flat angle towards the outer casing and will therefore also receive the emitted cold radiation of the absorber reflected by the casing. The physical temperature of the antenna was monitored to be at room temperature.
Another critical point is the filling level of the LN. If it is far above the microwave absorber, the radiation emitted from the absorber will be attenuated. The radiation of the LN itself is not too crucial, because its characteristic is far from a black body and its emissivity very low. Its reflectivity, however, could cause some spurious radiation due to reflections on its surface. In a worst-case scenario, the emitted low temperature of the absorber would be strongly attenuated and instead the antenna would measure spurious noise from the room which is reflected at the LN surface. But due to the chosen geometry, the conducting casing of the Dewar, the above mentioned antenna pattern, and an appropriate LN filling level, this influence can be neglected. With much more sensitive radiometer systems, which use a lot of integration time and measure with an accuracy of a tenth of Kelvin, these parameters *can* have some influence. Also, the boiling temperature of the LN is dependent on the actual air pressure. While this was accounted for during the measurements with the temperature stabilized test-bed at DA-Design to avoid misinterpretation of drifts during continuous measurement, this was not as critical for the short-term measurements in this work. Several filling levels were experimentally tested, as well as different angles of the antenna in relation to the LN surface, but no significant influence was observed with the applied setup.
An alternative setup would be to have an antenna pointed to a styrofoam container *above* the measurement setup. The container is covered with absorber at the bottom so that the

antenna looks directly through the styrofoam at the absorber, which is permanently cooled by the LN filled in the container. The styrofoam itself has negligible influence for the penetration of the radiation. The advantage is, that there is no influence due to reflection of the LN surface, and that the filling level of the container has no relevance at all. This way it can be generously filled and closed with a lid for better isolation and limiting evaporation, which is especially beneficial for long-term measurements. Figure 4.6 illustrates such an alternative setup.

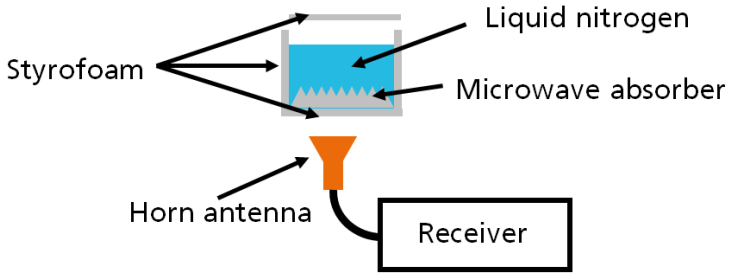

Figure 4.6: Alternative setup for the measurement system calibration with liquid nitrogen.

Disadvantage is, that despite the isolating capability of the styrofoam, the bottom of the container becomes colder than the surrounding air, which leads to condensation of the air moisture. Water drops at the bottom of the styrofoam container have on one hand significant influence on the radiation path and on the other hand risk to drop inside the antenna. Another issue with this setup is, that the air below the container is cooled down due to convection. If the setup is placed below the container, this will have an effect on the temperature stability of the measurement system. And long waveguides to move the receiver outside the reach of influence yield additional losses, also the waveguides are influenced by the cooling. While this setup, despite its drawbacks, would be favorable for long-term measurements and stability analysis, it was assessed to be too elaborate for the purpose of this work. Besides, it is not practicable for on-wafer measurements.

4.3 Measurement System Analysis

As it was emphasized in Section 4.1, a minimal overall noise figure of the measurement system is crucial to mitigate large influence on the measurement results. With this goal, several components were cascaded in the setups. A trade-off between minimal noise figure, optimum gain, and reduction of interstage mismatch had to be found. These factors will be discussed in the following.

4.3.1 System Noise Figure and Gain

The system noise figures of the setups can be characterized thoroughly and the results for the accordant setup can be taken into account for the interpretation of the measurements. However, the noise figure is not the only parameter which influences successful measurements. As was pointed out in Section 4.1, the choice of the proper gain in the setups front-end is equally important, because it dictates in which dynamic power range of the NFA the noise temperature is projected. The NF or losses of the first stages in the receiver chain (e.g.

the first LNA or isolator) are the relevant components that influence the overall system noise figure [82], while the noise introduced by the mixer or further amplifiers for example has little influence (this only applies for the influence on the system noise figure - not on possibly occurring reflections, as will be derived in Chapter 5). However, the gain or loss of *any* component within the receiver chain has a direct influence on the overall gain of the measurement setup. As was shown in Figure 4.2, for two setups with identical system noise figure, this yields different slopes of the hot-cold curve and, as a consequence, another dynamic range of the NFA is addressed.

Over a larger dynamic range, the NFA's power detector can exhibit a different linearity, yielding a different measurement result for the same noise temperature. In the application note [84] it is stated, that the power range in which the noise is measured in the NFA should be rather small because this favors the linearity of the detector. Because it is not known in which range the linearity of the detector is optimal, two different setups were used to characterize the circuits. A major focus of this work is therefore, to point out the influence of the measurement setup on the results and to explain diverging results of identical DUTs.

4.3.2 Interstage Mismatching

To have the best possible system noise figure of the measurement setup, it would be beneficial to have an amplifying component as a first stage. This is easily explained by applying the Friis formula [82]. Therefore, in a first approach, the reference plane of the measurement system was directly at the first stage amplifier input. This, however, resulted in strong oscillations in the measurement results, due to reflections between the LNA module and the probe. These reflections superpose with others that originate at the discontinuity between probe tip and the MMIC. At these stages, before the first LNA, where the power levels to be measured are very weak, this has a major influence. Since none of any components used in a measurement setup has an ideal matching, especially because noise is an extremely broadband effect, always *some* amount of the noise is reflected at its input or output. These re-reflections happen between any stage within the receiver chain and, even worse, can be carried forward through the subsequent stages where they are superposed with the other reflections. Therefore, the effect of mismatch on noise figure measurements is extremely complicated to analyze. Some effort was made to subtract this effect from the measurement result, by characterizing the critical components in magnitude and phase and subtracting their influence from the result. The outcome however, was not satisfying.

Isolators

The best way to minimize these reflections, is to place isolators between critical stages. While its influence on the overall system noise figure and gain is negligible if they are placed *after* the first LNA, its insertion loss directly adds to the system noise figure if it is placed at the first stage. However, especially at this position its use is mandatory to achieve a good improvement in the ripple of the results.
Figure 4.7(a) depicts the measured S-parameters of the isolator used as a first stage component. It has an input return loss of around $20\,\mathrm{dB}$ and an isolation of more than $30\,\mathrm{dB}$. This significantly reduces the amount of noise waves traveling back to the DUT, however, as results in Chapter 5 will show, this is not enough to completely isolate the DUT from the

influence of the measurement setup. If the antenna, which is used for the calibration causes re-reflections due to non-ideal matching, this error will persist in all subsequent measurements after the calibration. Therefore a good matching of the antenna is equally important. Figure 4.7(b) depicts the input return loss of the W-band horn antenna used for the system calibration. With an input return loss of more than $22\,\mathrm{dB}$ on antenna side and $20\,\mathrm{dB}$ on the isolator side, this effect can be significantly minimized, at least during calibration. For the following measurements however, the amount of interstage reflections depends on the matching of the DUT and, for on-wafer measurements, additionally on the matching of the wafer probe.

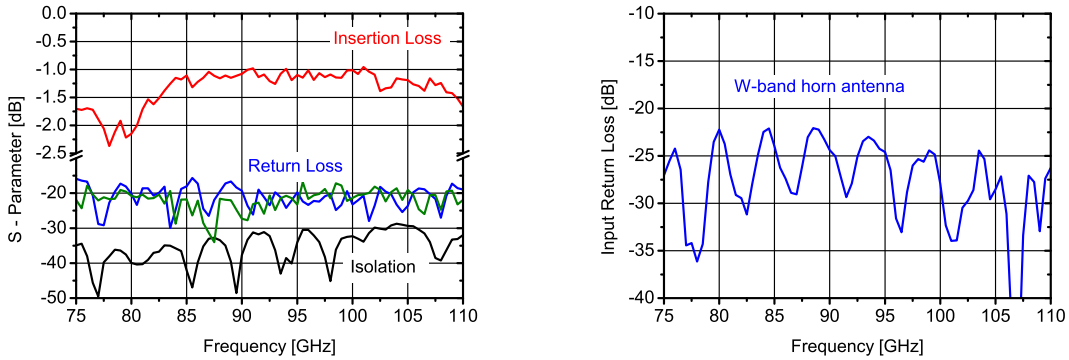

(a) Measured S-parameters of the W-band first stage isolator from HP (Ser.No.178).

(b) Measured return loss of the W-band horn antenna at the waveguide flange.

Figure 4.7: S-parameters of the most critical front-end components of the W-band measurement setup.

RF-probe

The previously described isolator can significantly reduce the reflections between the measurement setup and the *module* DUT and also between the setup and the RF-probe if the probe is sufficiently matched at the waveguide side. Figure 4.8 shows the S-parameters of the used *Picoprobe* for W-band (measured) and the *Cascade Microtech* probe for D-band (provided by the supplier). While the return loss on waveguide side is better than $20\,\mathrm{dB}$ at the respective center frequencies of both RF-probes and better than $10\,\mathrm{dB}$ within the respective waveguide band, the return loss on the probe-tip side for the W-band probe is less than $10\,\mathrm{dB}$ at some frequencies. This has two consequences. For one this yields re-reflections between the probe-tip side and the on-wafer DUT, which can not be avoided. Furthermore, the loss of the probes was only accounted for by subtracting the temperature increase due to its scalar loss (red curve in Figure 4.8) from the noise temperature results. This is normally a sufficiently valid approach. For very low absolute noise temperatures and for high reflection coefficients, however, the accurate way would be to account for the *available gain* of the wafer-probe, defined by Equation 4.7.

$$G_a = \frac{(1-|\Gamma_S|^2)|S_{21}|^2}{|1-S_{11}\Gamma_S|^2(1-|S_{22}+\frac{S_{12}S_{21}\Gamma_S}{1-S_{11}\Gamma_S}|^2)} \tag{4.7}$$

This means, that the amount of loss that the RF-probe inflicts on the measurement signal, is dependent on the matching and the reflection coefficients of its surrounding stages.

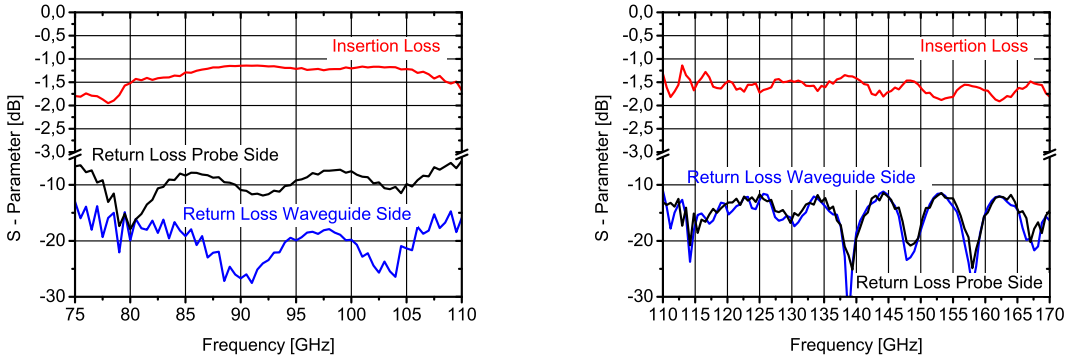

(a) W-band Probe

(b) D-band Probe

Figure 4.8: S-parameters of the microwave probes by GPP industries (W-band) and Cascade Microtech (D-band).

4.4 Final Measurement Setups in W- and D-band

4.4.1 W-Band Setups

For the noise temperature characterization of the reference loads, a dedicated hot-cold measurement setup with the possibility of on-wafer one-port measurements was established. A schematic diagram of the setup was already depicted at the beginning of this chapter in Figure 4.1. The reference plane for the hot-cold calibration with a corrugated horn antenna and microwave absorber at 398 and $77\,\mathrm{K}$ temperature is behind the RF-probe, which is mounted on a wafer probe station. To cool down the absorber, LN was used. Since the probe is not within the calibration loop (please see Figure 4.1), the resistive part of its loss adds noise to the measured noise temperature of the DUT. This additional noise is taken into account and subtracted from the result after measurement. The receiver consists of a LNA module with $20\,\mathrm{dB}$ small-signal gain and a receiver module containing an integrated LNA-mixer-MMIC with a conversion gain of approximately $10\,\mathrm{dB}$. The LO signal for the mixer is provided by a *HP* $83650B$ swept signal generator and an *HP* $83558A$ millimeter-wave source module for W-band. The IF output of the mixer is connected to an *Agilent* $8975A$ NFA. To minimize the influence of noise reflections, isolators were placed at critical stages. A photograph of the wafer probe station and the above mentioned components of the on-wafer measurement setup can be seen in Figure 4.9. Please be aware that the components necessary for the calibration of the setup (compare with Figure 4.1) are not present in the photographed scenario.

The return losses of the first stage isolator and the on-wafer measurement probe are both around $20\,\mathrm{dB}$ and the return loss of the horn antenna lies even well above $20\,\mathrm{dB}$. Since this is crucial for accurate measurement of the DUT with the Y-method, the degradation of the system noise figure due to a lossy first stage is accepted. The system noise figure of the measurement setup at the reference plane is shown in Figure 4.12. It is around $4\,\mathrm{dB}$ in the frequency range of $75 - 95\,\mathrm{GHz}$. It should be noted that this slightly worsens if referred to the reference plane on chip, due to the mentioned losses of the probe.

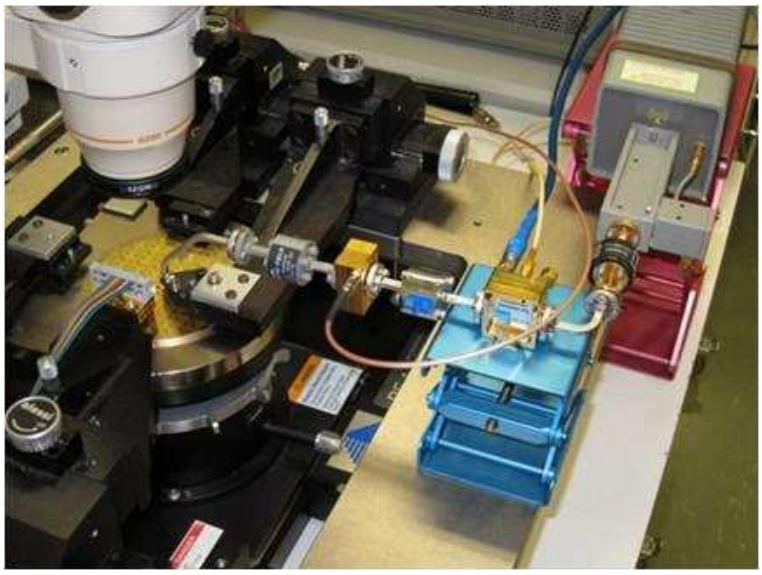

Figure 4.9: Photograph of the wafer probe station and the on-wafer measurement setup.

W-Band Temperature Chamber Measurement Setup

While the noise temperature of passive loads has a linear relation to its physical temperature (1 K/°C), investigations in [34] (for SiGe HBT ACLs) and [65] (for GaAs FET ACLs) have shown, that ACLs are less sensitive to temperature variations than passive loads (0.3 K/°C and less than 0.4 K/°C, respectively). It should be noted, that the investigated ACLs in these publications were at much lower frequencies (1.4 GHz and 10.69 GHz, respectively), than the ACLs in this work and that in both publications only physical temperatures above 0 °C were analyzed (0-50 °C). To analyze the temperature dependence of the W-band ACL design integrated in the SCFE, an ACL module was characterized in a temperature chamber. The ACL module was placed into a *WEISS WKL series* climate and temperature test chamber and connected with a $WR-10$ waveguide to the measurement receiver outside the chamber (see Figure 4.10). The measurement setup was calibrated at the reference plane at the ACL module before and after the test series. Because a long piece of waveguide had to be placed between the first LNA outside the chamber and the DUT inside the chamber, the reference plane moves inside the chamber, yielding a higher system noise figure than the regular setup (see blue curve in Figure 4.12). To ensure a stable operation of the receiver and to minimize the influence of thermal conduction through the waveguide, a fan was placed at the front-end and a thermistor (NTC) was attached to the first stage LNA, monitoring its temperature. To avoid condensation inside the ACL module, the temperature ramp was run from cold to hot. The temperature was increased from -40 °C to +80 °C in steps of 10 K. Since the ACL is not an amplifying element and has negligible power dissipation, it can be assumed that after an appropriate time, the temperature of the module is equal to the temperature set inside the test chamber.

Millilab Setup

For the measurements performed at *Millilab*, a standard waveguide load was used with a heating resistor attached to its body. A separate control box measured the temperature at

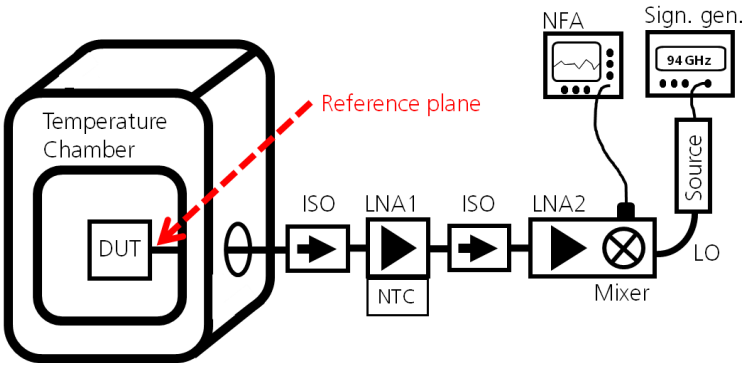

Figure 4.10: Temperature chamber measurement setup.

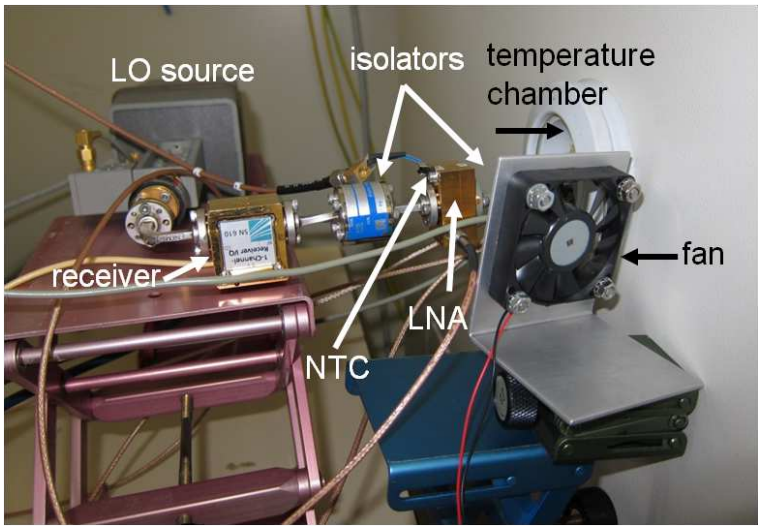

Figure 4.11: Photograph of the temperature chamber measurement setup.

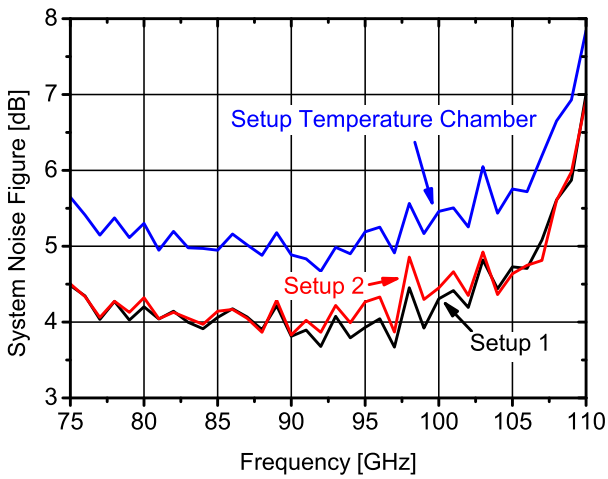

Figure 4.12: System noise figure of the measurement systems at their reference plane.

the waveguide load with a sensor and controlled the current in the resistor. The temperature oscillated with a $\pm 2\,\mathrm{K}$ amplitude around the set temperature. Four temperatures between ambient and $100\,^{\circ}\mathrm{C}$ were used to fit a hot-cold curve between the calibration points. All points were very close to the resulting line, and essentially a calibration with only ambient and $100\,^{\circ}\mathrm{C}$ would have yielded the same results. Measurements at all temperatures took about 15-20 minutes when starting from the lowest temperature towards the higher temperatures. A $50\,\mathrm{mm}$ long stainless steel waveguide was used to minimize the heat flux between the heated load and the measurement setup. While the isolator did not get warmer during the measurements, a temperature gradient could be observed on the solid steel waveguide.

RPG Setup

Additional measurements were performed at RPG. For the measurement of the ACL and AHL modules different first stage LNAs were used to adapt for the large difference in expected noise temperature. For the ACL measurement setup an LNA with a small-signal gain of $40\,\mathrm{dB}$ was used, while for the AHL measurement setup an LNA with only $25\,\mathrm{dB}$ was used, to avoid the need of an additional attenuator. The respective system noise figures differ from each other and are shown in Figure 4.14. For the ACL setup the measurement system has a noise figure of below $5\,\mathrm{dB}$ (red curve) and for the the AHL setup a noise figure of around $6\,\mathrm{dB}$ (blue curve). Instead of a NFA, a *Rohde&Schwarz FSU Spectrum Analyzer* was used to measure the noise power from the IF output of the measurement setup's mixer. A *Rohde&Schwarz SFM 100A Signal Generator* was used to generate the LO signal for the mixer. The receiver front-end is placed on a temperature stabilized Peltier-testbench, which reduces the gain variations of the measurement setups and yields very accurate results. As in the IAF setups, an isolator and LNA are used as first stages. A photograph of the setup is shown in Figure 4.13.

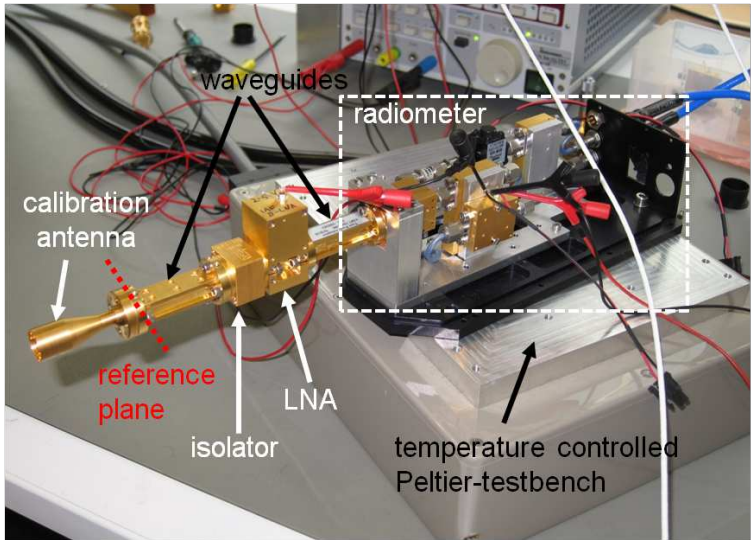

Figure 4.13: Module measurement setup with temperature stabilized radiometer at RPG.

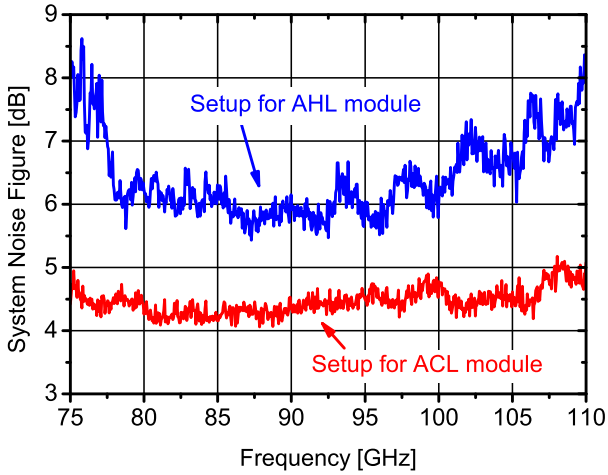

Figure 4.14: System noise figures of the measurement system at RPG for the characterization of ACL and AHL modules.

4.4.2 D-Band Setups

As previously mentioned, the D-band LNA, presented in Section 3.5, was specially developed for the purpose of characterizing the D-band ACL circuits. Therefore, several LNA MMICs were assembled into split-block modules and characterized. While the overall performance of the modules was very equal to each other, one of the modules has shown particularly good results in terms of noise figure. Consequently, this module *LNA 667* was always chosen to be the first amplifying stage in the following setups. Its performance is presented in Chapter 6. Other available modules were the *LNA 666* and *LNA 670*. Due to the limitation of the mixer in the receiver, only the *lower* part of the D-band ($110 - 150$ GHz) can be analyzed. The general architecture of the setup (see Figure 4.15(a)) is similar to the ones presented in W-band. Again, the reference plane is always at the input of the first isolator. After hot-cold calibration with a D-band horn antenna, the antenna is replaced by the *Cascade Microtech* D-band probe and accounted for the probe loss (see Figure 4.8(b)) during the noise temperature calculation. Furthermore, the setup consists of two consecutive LNA modules, connected by a piece of waveguide. Together, they achieve a total gain of 44 dB. Different permutations of the sequence of LNAs and isolators were investigated by comparison of the flatness of the system noise figure over frequency. This gives an indication about the unwanted reflections of the power waves between the stages. Typically best performance is achieved if a lossy component is placed between two amplifying stages. Hence, the two consecutive LNAs were believed to be the most critical combination within the setup. The measurement of the system noise figure presented in Figure 4.16 (blue curve), however, confirms that this sequence achieved the wanted flatness in the frequency range above 130 GHz. While this is the relevant frequency range for the intended characterization of the D-band ACL MMICs, which were designed at a center frequency of 140 GHz, this setup was not suitable to investigate the performance of the W-band ACL module above 110 GHz. All setups that were hot-cold calibrated with the available D-band horn antenna, exhibited a more or less strong ripple below 130 GHz, independent of the sequence or number of LNAs and isolators. Therefore a modified assembly was used, especially for the characterization of the W-band

ACL module. It is presented in Figure 4.15(b) and allows a hot-cold calibration with the previously described W-band horn (see Figure 4.7(b)). For this, the waveguide transition to W-band and the *HP* isolator (see Figure 4.7(a)) are placed directly in front of the *LNA 667*. After hot-cold calibration with the W-band horn, the DUT is connected at the reference plane, as shown in Figure 4.15(b). The result of this measurement is presented in Section 5.2.

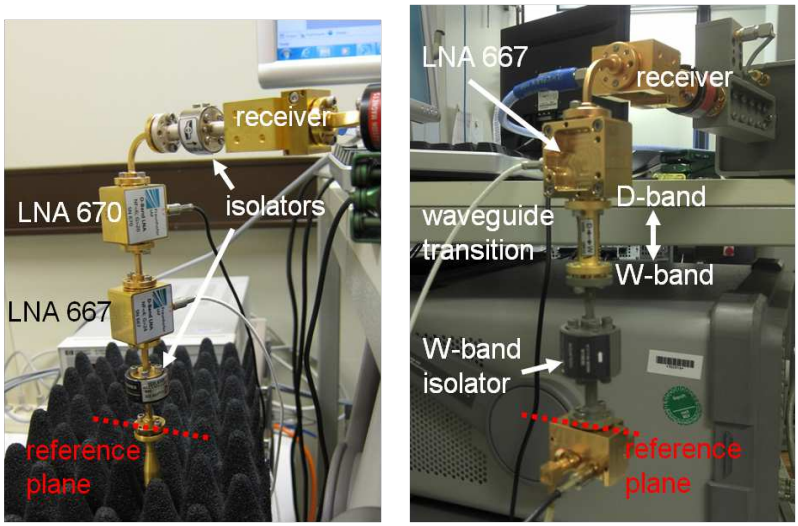

(a) D-band measurement setup for on-wafer characterization of ACLs and module measurements.

(b) Modified D-band measurement setup for characterization of W-band ACL-module.

Figure 4.15: Different measurement setups for the lower D-band ($110 - 150\,\mathrm{GHz}$).

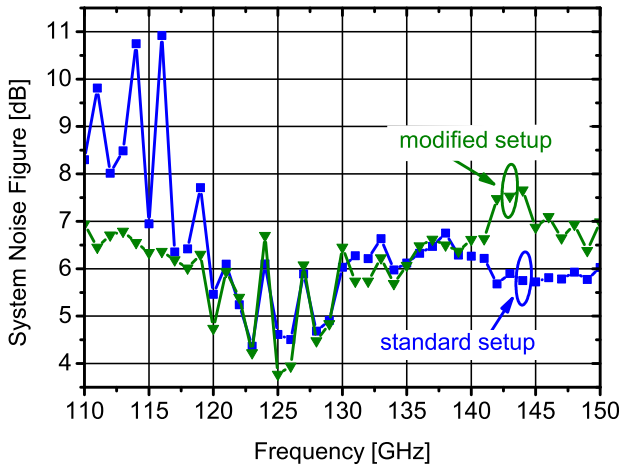

Figure 4.16: System noise figures of the two D-band measurement setups.

The system noise figure of the *modified* D-band setup is also shown in Figure 4.16 (green curve). Compared to the chosen general setup (blue curve) and all other investigated setups, it exhibits an adequate flatness and a noise figure below $7\,\mathrm{dB}$ in the frequency range of $110 - 120\,\mathrm{GHz}$, which is suitable for the characterization of the W-band ACL module. In

return its performance deteriorates above $140\,\text{GHz}$ compared to standard setup. In general, the covered frequency range by both setups can be divided into four sections:

- From $110 - 120\,\text{GHz}$, where the calibration with the W-band horn is advantageous (green curve).
- From $120 - 130\,\text{GHz}$, where *both* setups have a strong fluctuation between the measurement points, indicating a common inherent error source other than the antenna. This could be the receiver or more likely the first stage *LNA 667*, which has an output return loss of less than $-10\,\text{dB}$ in the range of $115 - 128\,\text{GHz}$ (see Figure 6.2).
- From $130 - 140\,\text{GHz}$ where both setups have a very similar system noise figure.
- From $140 - 150\,\text{GHz}$ where the standard D-band setup with two LNAs is advantageous (blue curve).

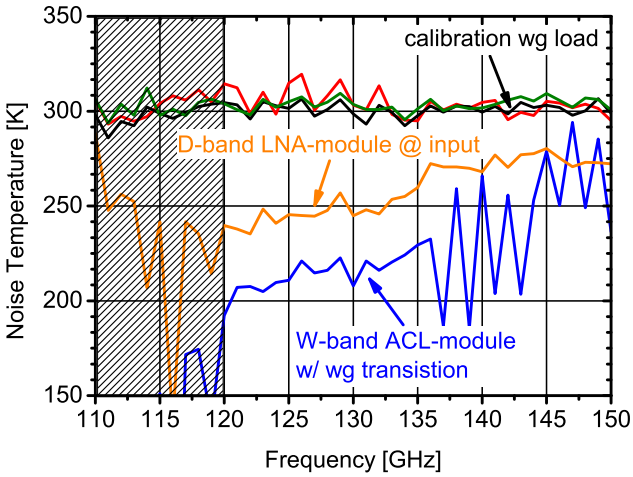

Figure 4.17: Measurement of W-band ACL-module with a waveguide transition to D-band, and the D-band LNA module 666 at its input port.

To verify the suitability of the standard setup for the characterization of the D-band ACLs, the D-band LNA module 666 and the W-band ACL module were measured. After hot-cold calibration with the D-band horn, the LNA was connected with its *input* port to the reference plane at the D-band isolator, while the output port was terminated with a waveguide matched load. Likewise, the W-band ACL-module was connected at the reference plane, but together *with* the waveguide transition from W- to D-band. The result can be seen in Figure 4.17. As a reference, a waveguide calibration load was measured (black curve). The red curve and the green curve are the measured noise temperatures of the ACL-module and the LNA without bias, respectively. The shaded area indicates the frequency range, where due to the previously determined system noise figure no correct results can be expected. The measured noise temperature of the ACL module (blue curve) is consistent with the module measurement that was performed with the modified setup (see Figure 5.11 except for the strong ripple above $135\,\text{GHz}$ which is due to the waveguide transition (which was not part of the calibration loop) and no reason for concern. The LNA (orange curve) exhibits a

noise temperature around $250\,\mathrm{K}$ from $120-135\,\mathrm{GHz}$ and around $275\,\mathrm{K}$ from $135-150\,\mathrm{GHz}$. However, the ripples on the curves of the calibration load and the DUTs *without* bias from $120-135\,\mathrm{GHz}$ indicate, that the strong ripple of the system noise figure in this range (see Figure 4.16) has a not negligible influence on the measurement. This has of course more consequences at temperatures that are in the vicinity of the temperatures with which the setup was calibrated (in this case the ambient temperature) and less at temperatures that are encompassed by the two calibration references (like the ACL module). Nevertheless, due to this verification, only measurement values above $135\,\mathrm{GHz}$ are assumed to be reliable with this setup. Therefore, the area below this frequency is also shaded in the result figures in Chapter 6.

Summary and Conclusion

In this chapter it was elaborated, that it is not sufficient to assemble a supposedly standard measurement setup, but that one-port noise measurements - especially at these frequencies and such expected low noise temperatures - are a very challenging task. Several different approaches were evaluated, which concluded into few dedicated measurement setups in W- and D-band, that were hot-cold calibrated with absorber at ambient temperature and at $77\,\mathrm{K}$. One common most critical influence however, was found to be the reflected noise power between the multiple stages due to non ideal matching. Even though this problem is also known from standard two-port noise measurements, there exists no analytical way to satisfactorily account for this reflections or to eliminate its influence on the noise measurement result. Therefore, as crucial part of this work, critical components were identified and measures taken to reduce their influence as much as possible. However, the conclusion of comparing very similar setups against each other is, that it is *not* sufficient to just apply these best practices and then to rely on the result. But that in order to have reliable results for such impedance sensitive DUTs, measurements should be performed with different setups, yielding different results, but narrowing down the *correct* values. Measurement results of this kind should only be interpreted under consideration of the applied measurement setup, which will be further discussed in the following result chapters.

5 Characterization of W-Band Active Load MMICs and Modules

The setups presented in the last chapter allow a thorough noise characterization of the circuits designed for this work, in addition to the standard S-parameter measurements. While the latter were performed in a common procedure with standard measurement equipment and unambiguous results, all the measured noise temperatures presented in this chapter need to be discussed with regard to the used measurement setup. Especially the comparison of identical DUTs, measured with different setups, or the difference between on-wafer and module measurement results with the *same* setup will give further insight into the interdependency of the noise measurement setup and the DUT. This shall be discussed in this chapter, along with the comparison of the used noise simulation method with the measurement result. Furthermore, the performance of the manufactured ACL modules will be compared against other loads and its suitability as a hot-cold reference for noise measurements demonstrated.

5.1 MMIC measurements

5.1.1 89 GHz ACLs

Because the evaluation and assembly of the appropriate measurement setup described in the previous chapter was not yet completed at the early stage of the *Calload* project, the standalone ACL circuits for this project, were initially shipped to the project partner *Millilab* for characterization. The measurement results of the 89 GHz ACL $V1$ were awaited to confirm the simulation approach before initiating a re-design. Later, comparative noise measurements were performed for some of the circuits with the setups at IAF. The S-parameters of the circuits were measured with a VNA, an appropriate W-band extension and GSG on-wafer probes. In Figure 5.1(a), the measured input return loss (red curve) is compared to the simulated value (blue curve) and it can be noticed that the measurement result at 89 GHz is 10 dB worse than than the predicted value. At the same time, in Figure 5.1(b), the comparison of the measured result (red curve) and the noise temperature simulated with Equation 3.20 (blue curve), yields a better result than predicted at 89 GHz. Therefore, the design goal of the re-design was to focus on an improved return loss, while accepting a higher noise temperature. For the measurements, the ACLs were biased with a drain voltage of $V_d = +1.0$V and the gate voltage V_g was set to yield a drain current of $I_d = 400$ mA/mm, which corresponds to the bias settings in the simulation.

The results of the re-design, 89 GHz ACL $V4$, are depicted in Figures 5.2. Again, the same bias was applied for the measurements as for the simulation (same bias as for ACL $V1$). The simulated input return loss (blue curve) in Figure 5.2(a) was much more ambitious than for ACL $V1$, yet, an even larger discrepancy of over 20 dB between simulation and

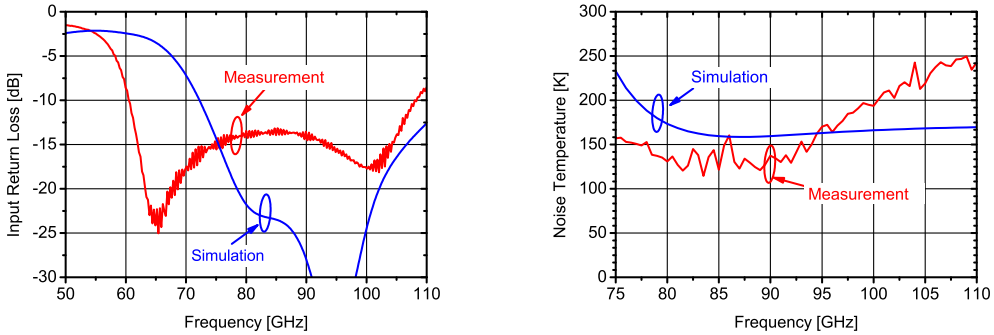

(a) Input return loss.

(b) Noise temperature.

Figure 5.1: Measured and simulated S-parameter and noise temperature of $89\,\text{GHz}$ ACL $V1$ MMIC, measured at *Millilab*.

measurement (red curve) can be observed. However, an improvement of over $5\,\text{dB}$ was achieved compared to ACL $V1$. For ACL $V4$, the measured (red curve) noise temperature in Figure 5.2(b) was higher than predicted in the simulation (blue curve), even though the simulation yielded similar results as for ACL $V1$. By the time ACL $V4$ was manufactured, the noise measurement *Setup 2* was operational, allowing a comparative measurement which is represented by the green curve in Figure 5.2(b). Different cells were probed and biased with different voltages, yielding a variation of maximum $10\,\text{K}$ at $89\,\text{GHz}$. For the green measurement curve shown in Figure 5.2(b), $V_g = 0.0\text{V}$ and $V_d = +0.6\text{V}$ was set, to achieve the same drain current of $I_d = 400\,\text{mA/mm}$.

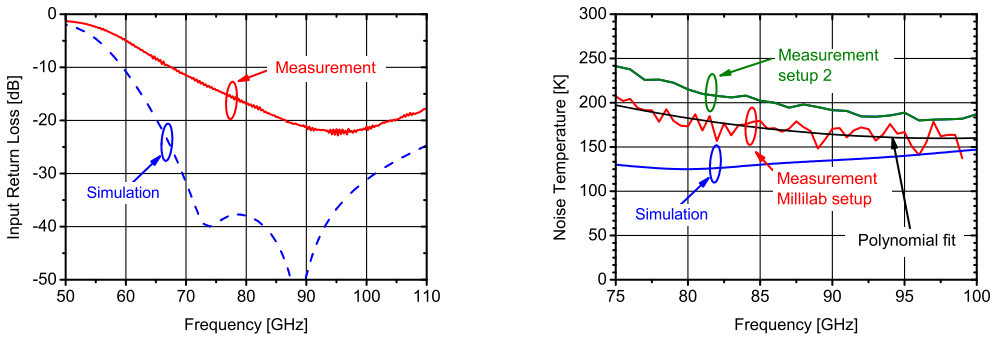

(a) Input return loss.

(b) Noise temperature.

Figure 5.2: Simulated S-parameter and noise temperature of $89\,\text{GHz}$ ACL $V4$, compared to measurements at *Millilab* and at IAF.

The difference of the measurement results achieved with the two different setups, confirms the concerns that initially led to the investigation of one-port noise measurement setups in Chapter 4. At some frequencies, both setups yield identical results, while at others, a worst case difference of around $40\,\text{K}$ can be observed. Furthermore, the red curve exhibits a strong ripple, which is an indicator for the noise power reflections described in Chapter 4. It also shows, that by the taken measures to reduce this impact, this ripple can be significantly reduced. However, if the effect of the ripple is masked by applying a second order polynomial

fit through the measurement points (black curve), the principal trend of both measurements is very similar. This is of course a very nonscientific approach and only done at this point to emphasize the importance of a thorough investigation of the measurement setup. Still, the fact that in average, one setup yields consistently (referring to the fitted curve) lower temperatures, than another remains. *This* can be explained with the described influence of the setup's front-end gain on the linearity of the NFA in the dynamic range. Further observations of this effect will be discussed in the course of this chapter. At this point, it can be stated, that the final measurement setups, derived from the investigations in Chapter 4, did successfully reduce the influence of noise power reflections. And that the results measured with *Setup 2* yield around $30\,\mathrm{K}$ higher noise temperature for on-wafer measurements at $89\,\mathrm{GHz}$.

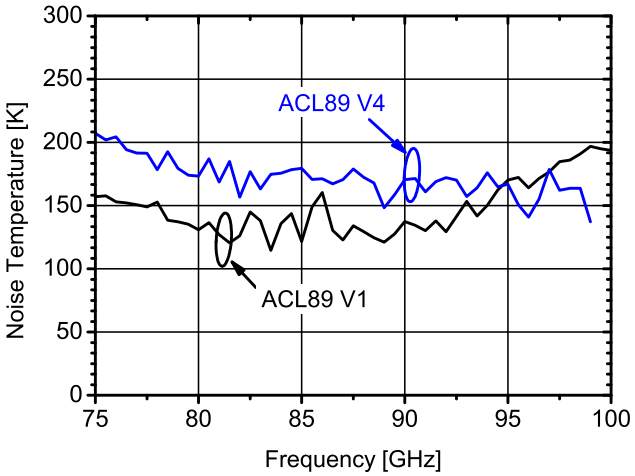

Figure 5.3: Comparison of noise temperatures of $89\,\mathrm{GHz}$ ACLs $V1$ and $V4$, measured at *Millilab*.

In Figure 5.3 the noise temperatures of both $89\,\mathrm{GHz}$ ACL versions are compared against each other. As expected, the noise temperature of $V4$ is around $40\,\mathrm{K}$ higher as consequence of the trade-off for an improved input return loss. What's more, it can be seen, that in the vicinity of $85\,\mathrm{GHz}$, where the input return loss of ACL $V1$ is worse than $-15\,\mathrm{dB}$, the ripple on the noise temperature is particularly strong. Simultaneously, for ACL $V4$, where the input return loss is better than $-15\,\mathrm{dB}$ over the entire W-band, the ripple is slightly smaller.

5.1.2 W-band ACLs

The noise temperature of the stand-alone W-band ACL circuit that was intended for integration into the SCFE, as well as for module assembly, was measured on-wafer with *Setup 1*. The input return loss was measured with a VNA, two different port extensions for W- and D-band and the respective on-wafer probes. The ACL bias was $V_g = +0.1\,\mathrm{V}$ and $V_d = +1.0\,\mathrm{V}$, yielding an $I_d = 300\,\mathrm{mA/mm}$.

Figures 5.4 show the comparison between the simulation (red curves) and the measurement (black curves). For the simulation of the noise figure, Equation 3.24 was used. In Figure 5.4(a), a perfect match between simulation and measurement at the desired center frequency of $94\,\mathrm{GHz}$ can be observed, yielding $-30\,\mathrm{dB}$. Above the center frequency, the input return

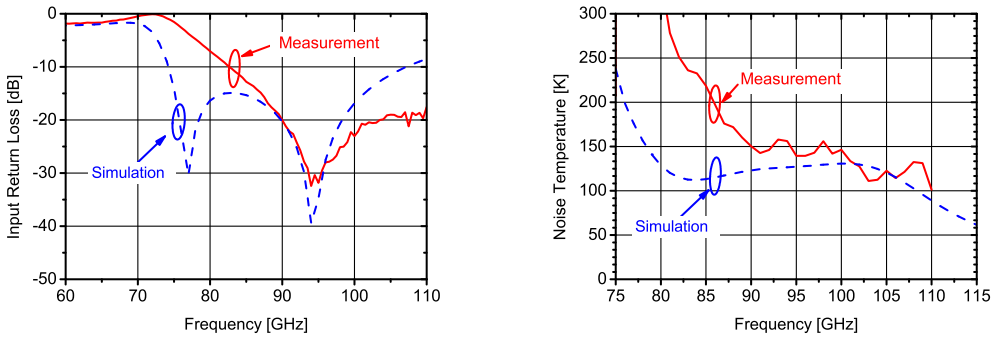

(a) Input return loss.

(b) Noise temperature.

Figure 5.4: Comparison of simulated and measured input return loss of the ACL MMIC and noise temperature.

loss is better than expected, yielding around $-20\,\text{dB}$ up to $110\,\text{GHz}$ and more than $-10\,\text{dB}$ up to $140\,\text{GHz}$. The measured noise temperature above $90\,\text{GHz}$ in 5.4(b) matches very well with the simulated values, but drastically increases for frequencies below. This coincides exactly with the degradation of the input return loss. This emphasizes the fact, that an extraordinary good input return loss is equally important as the supposed main goal of a low noise temperature. Further evidence of this correlation will be presented in Section 5.2.

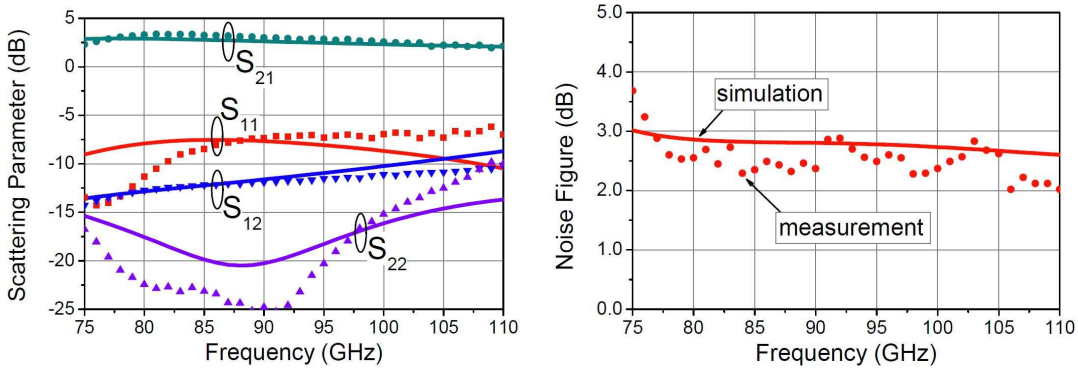

(a) S-parameter.

(b) Noise figure.

Figure 5.5: Comparison of simulation and measurement results of the ACL S-parameters and noise figure.

Compared to the previous ACLs, the W-band ACL, that was intended for the AHCL, has the notable difference that the drain side is also routed to an RF-signal pad. Thus, a full S-parameter analysis can be performed, as well as a standard two-port NF measurement. This allows to verify, if the desired design goals for the simplified approach of [72] were achieved. Remember, that Equation 3.25 is only valid for a perfect match on the drain side of the transistor. Furthermore, the added noise from the *output* port is minimized, if the backward gain is reduced. Therefore, the focus of this design was to achieve the lowest possible $S22$ and $S12$, while still achieving noise matching at the gate side. The measurements were performed with a bias of $V_g = 0.0\,\text{V}$ and $V_d = +0.8\,\text{V}$, yielding a drain current of $100\,\text{mA/mm}$. As a hot-cold source for the NF measurement, a *Noise Com* noise diode was used. As can be seen in Figure 5.5(a), measured and simulated S-parameters are

in good agreement. With a measured backward gain of less than $-10\,\mathrm{dB}$ and a $S22$ of below $-25\,\mathrm{dB}$ at $90\,\mathrm{GHz}$, the validity of 3.25 is assured. Figure 5.5(b) shows the comparison of the NF measurement with simulation. An achieved NF of below $3\,\mathrm{dB}$ confirms a successful noise matching.

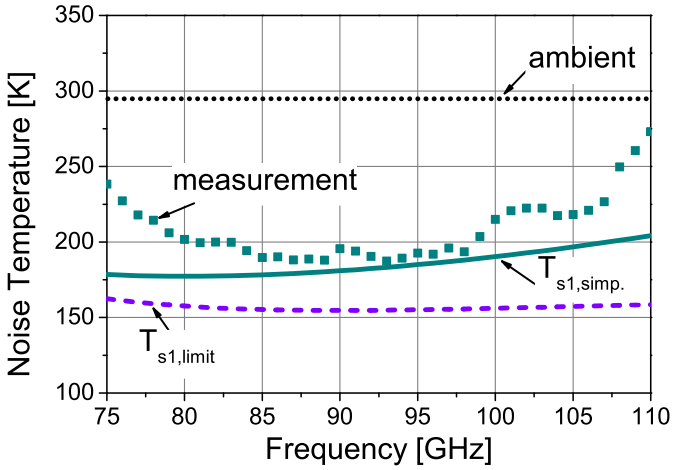

Figure 5.6: Comparison of measured noise temperature with *Setup 1* to two simulation methods. The dotted line indicates ambient temperature.

Figure 5.6 shows, that the measured noise temperature between 85 and $98\,\mathrm{GHz}$ is only slightly higher than simulated. Above $100\,\mathrm{GHz}$ and even more towards $110\,\mathrm{GHz}$, it strongly increases, which coincides with the deteriorating $S22$ in Figure 5.5(a). This confirms the relevance of a good $S22$ for the validity of 3.25. Although a low $S12$ was achieved to minimize the backward gain, its influence is yet not negligible: $T_{s1,limit}$ in Figure 5.6 depicts the noise temperature that could be achieved with zero backward gain.
The absolute noise temperature achieved with this approach is higher than for the previously presented ACLs. This is due to the different design goal prioritization, which yields a non ideal $S11$. The influence of $S11$ on the achievable noise temperature was pointed out above.

5.1.3 W-band AHL

The noise temperature of the stand-alone W-band AHL circuit that was intended for integration into the SCFE, as well as for module assembly, was measured on-wafer with *Setup 1*. The input return loss was measured with a VNA, two different port extensions for W- and D-band and the respective on-wafer probes. The AHL bias was $V_g = 0.0\,\mathrm{V}$ and $V_d = 0.8\,\mathrm{V}$, yielding an $I_d = 384\,\mathrm{mA/mm}$.

Figures 5.7 show the comparison between the simulation (red curves) and the measurement (black curves). Again, Equation 3.24 was used, to simulate the noise temperature. While a fairly good agreement between simulation and measurement is demonstrated in Figure 5.7(a), the achieved noise temperature in Figure 5.7(b) decreases faster than predicted by the simulation towards higher frequencies. However, the difference of almost $2500\,\mathrm{K}$ over the entire band due to this gradient is not much if compared to noise diodes. We remember, that as explained in Section 4.2, the ENR_{dB} of the *Noise Com* noise diode *NC5110* varies between 9 and $20\,\mathrm{dB}$, yielding a noise output flatness of $\pm 5.5\,\mathrm{dB}$. If the maximum ($3950\,\mathrm{K}$)

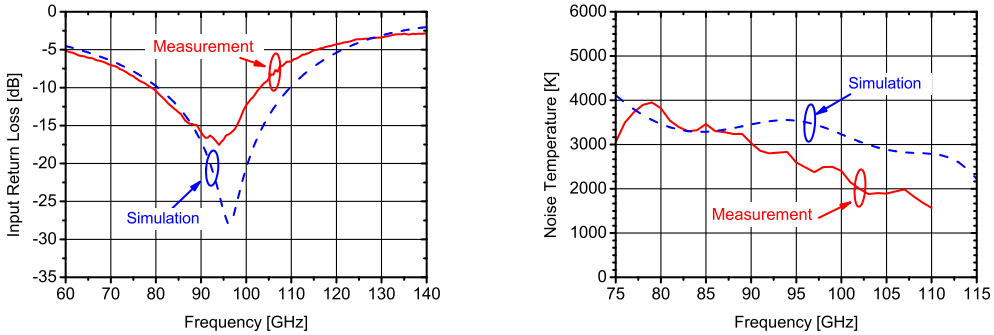

(a) Return loss.

(b) Noise temperature.

Figure 5.7: Comparison of simulated and measured input return loss of the AHL MMIC and noise temperature.

and minimum ($1570\,\mathrm{K}$) noise temperatures from the measurement shown in Figure 5.7(b) are used to calculate the achieved ENR_{dB} with Equation 4.4, the resulting ENR_{dB} are $11\,\mathrm{dB}$ and $6.4\,\mathrm{dB}$, respectively. This corresponds to a flatness twice as good as for the mentioned ND. However, the absolute noise temperature of the AHL is considerably lower than of the ND. The packaging of the AHL MMIC has not much influence on the absolute noise temperature, as will be shown in the following section.

5.2 Module Measurements

The W-band ACL (chip photograph in Figure 3.17(a), results in Figure 5.4) and the W-band AHL (chip photograph in Figure 3.17(b), results in Figure 5.7), which were integrated in the SCFE, were packaged into split-block modules (ACL module 1 and AHL module 1). Furthermore, the $89\,\mathrm{GHz}$ ACL $V2$ depicted in Figure 3.14(b), which is a variant of the ACL integrated in the ACSS, was packaged (ACL module 3). As stand-alone modules, their performance can be further investigated. The influence of the wafer-probes is eliminated and comparative measurements can be performed at other facilities. Furthermore, the suitability of the active loads as a calibration load for standard noise figure measurements can be demonstrated and its noise temperature can be compared to the input port noise of standard LNAs.

Figure 5.8(a) shows the assembled ACL module 1 with a standard *UG-387* waveguide flange and two subminiature type B (SMB) connectors for the gate and drain voltage supply. In Figure 5.8(b) the open split-block is depicted and the mounting of the ACL MMIC can be seen. As for the D-band LNA, the transition to waveguide is realized with a feeding patch and a microstrip line on a quartz substrate. The DC and RF pads are bonded with gold wires to the bias supply and the microstrip line, respectively.

First, the input return loss of the ACL module was verified at different bias conditions. Comparing the result in Figure 5.9 to the on-wafer measurement in Figure 5.4(a) shows, that the assembly into the split block package has negligible influence on the $S11$. The minimum of $-15\,\mathrm{dB}$ is slightly shifted towards $90\,\mathrm{GHz}$ and above $100\,\mathrm{GHz}$ the $S11$ even improves compared to the bare MMIC. Overall, the input return loss of over $10\,\mathrm{dB}$ between 80 and $105\,\mathrm{GHz}$ is very appropriate for the intended noise temperature measurements. The

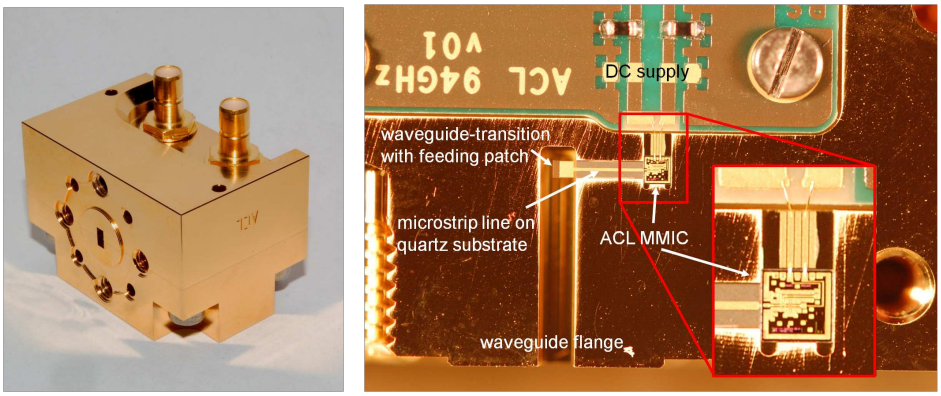

(a) Assembled ACL module in a split-block package.

(b) Open module with ACL MMIC and transition to waveguide.

Figure 5.8: Photographs of the ACL module 125-001.

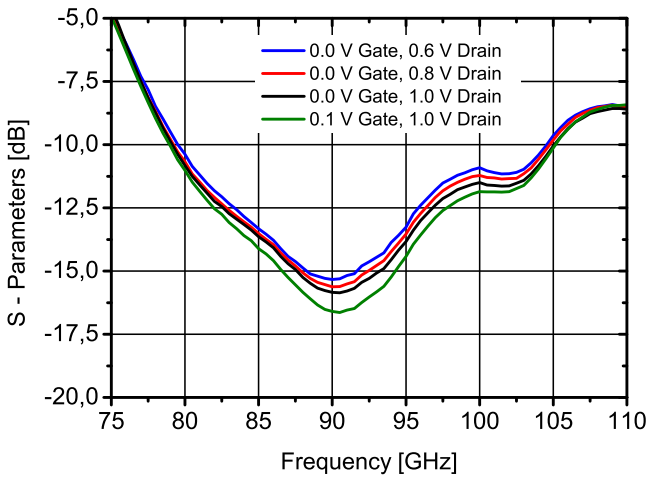

Figure 5.9: Measured input return loss ($S11$) of the ACL module 125-001 at different bias conditions.

influence of the $S11$ on the noise measurement was previously pointed out and will be further emphasized in the following. The change of $S11$ due to bias variations, however, has negligible influence on the noise measurement compared to the effect this bias change has on the generated noise in the ACL.

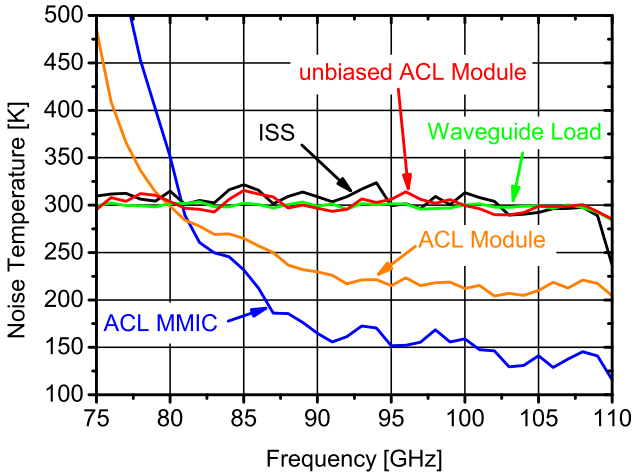

Figure 5.10: Noise temperatures of ACL MMIC and module, measured with *Setup 1*. As a reference, the measured noise temperatures of calibration standards were added in the graph.

Figure 5.10 compares the measured ACL on-wafer noise temperature (blue curve) with the measured noise temperature of the ACL module (orange curve). Both measurements were performed with *Setup 1*. The bias for the module was $V_g = 0.0\,\mathrm{V}$ and $V_d = 0.6\,\mathrm{V}$, yielding an $I_d = 200\,\mathrm{mA/mm}$ which was the optimum for minimal noise. Without bias, the ACL module exhibits an ambient noise temperature (red curve), similar to waveguide calibration load (green curve) or the on-wafer measurement of an impedance standard substrate (ISS), which were included in the graph for comparison. As expected, the losses related to chip bonding and the waveguide transition increase the noise temperature of the ACL module. However, subsequent measurements with other setups reveal, that the ACL module seems to exhibit considerable lower noise.

The black curve in Figure 5.11 describes the same measurement of the ACL module 1 with *Setup 1*, as the orange curve in Figure 5.10. Measured with *Setup 2*, however, the same ACL module with identical bias achieves a noise temperature, which is up to $70\,\mathrm{K}$ lower. We remember, that the system noise figure of both measurement setups was determined in Chapter 4 and found to be almost identical - not explaining this difference (see Figure 4.12). Furthermore, the front-end of both setups is identical up to the *LNA2+Mixer* stage (see Figure 4.1). To preclude a fundamental systematic error in the setup, the ACL module was characterized one more time with the setup at RPG, which has a slightly higher system noise figure than *Setup 1* and *Setup 2* up to $100\,\mathrm{GHz}$ and similar or better for higher frequencies (see Figure 4.13). The result of the noise temperature measurement with RPG's setup is represented by the blue curve in Figure 5.11 which is located right in the middle between the other two curves. For now, the difference between the measurements is explained by the different conversion gain of the *LNA2+Mixer* stage at the IAF setup and a different total (conversion) gain of the RPG setup. This projects the measured temperature in different

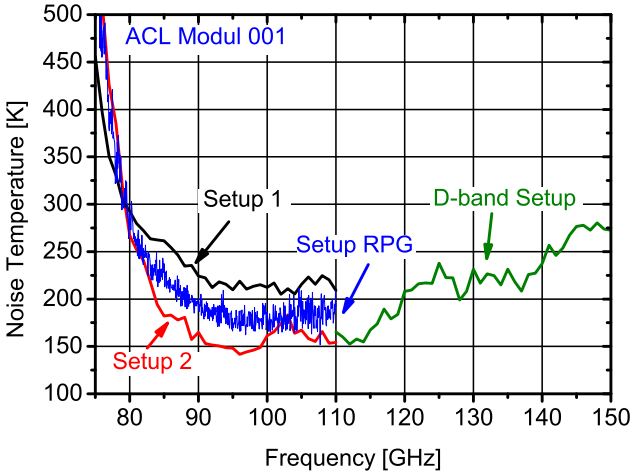

Figure 5.11: Comparison of measurement results of ACL module 125-001 with four different setups.

dynamic ranges of the NFAs power detector which can have non-linearities. Later in this chapter, further evidence of the setups influence is derived. A fourth measurement was performed with the modified D-band setup. The setup, including the ACL as a DUT, connected below the reference plane was shown in Figure 4.15(b). The result is the green curve in Figure 5.11. It is notable, that the D-band result fits very well to the one achieved with *Setup 2*. Except for the first W-band isolator and the NFA, totally different components were used, as described in Chapter 4.

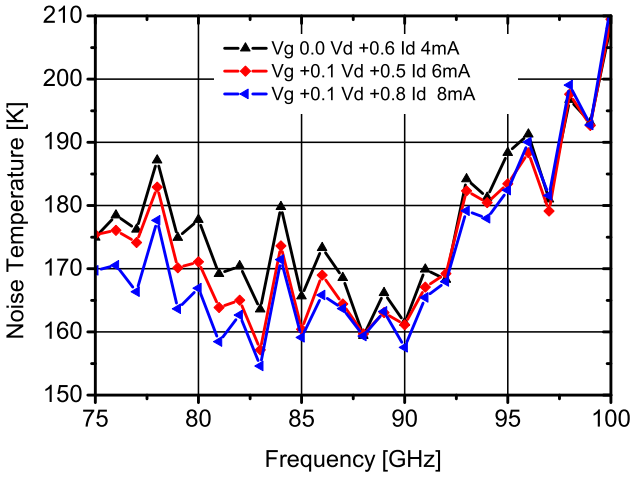

Figure 5.12: Noise temperature of ACL module 125-003 at different bias, measured with *Setup 2*.

The bias dependency of ACL module 3 was only characterized with *Setup 2* and the module results then compared with on-wafer results of the MMIC that is mounted in the module. Figure 5.12 shows the measured noise temperatures at three different bias conditions, yielding a normalized drain current of $133\,\mathrm{mA/mm}$ (black curve), $200\,\mathrm{mA/mm}$ (red curve), and $267\,\mathrm{mA/mm}$ (blue curve). The bias dependent variation of the noise temperature at the

designed target frequency 89 GHz is less than 5 K, which is impressive and of crucial importance when using an ACL as a reference load. LNAs are typically more sensitive to gain variations and the advantage of ACLs over LNAs in this respect will be presented in the next section. But first, the module measurement of module 3 shall be compared to the on-wafer results.

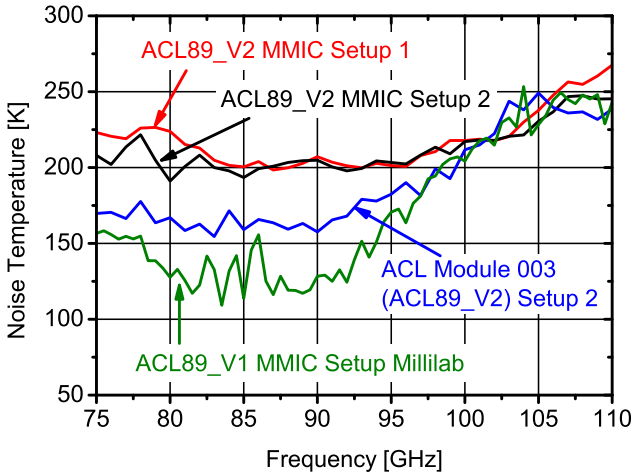

Figure 5.13: Comparison of measurements with setup 1 and setup 2. The black curve is the result of the exact same chip that was assembled in ACL module $125 - 003$ (ACL 89 GHz V2). The chip characterized by the red curve is identical but from a different wafer. As a comparison a measurement of ACL 89 GHz V1 at *Millilab* is shown.

From the curves depicted in Figure 5.13 several things can be concluded. The red and the black curve characterize two different dies of the same MMIC, measured with different setups. The two measurements were performed with a time period of two months in between. This indicates, that the principal measurement method is fairly reproducible and that both setups yield comparable results for *on-wafer* measurements, even with different setups. On the other hand it would be expected, that the module exhibits a higher noise temperature than the MMIC, due to the transition losses, as it was seen in Figure 5.10. However, we have also seen, that module measurement results of ACLs (we will see later, that this is not the case for LNA modules) vary strongly, depending on the used setup (see Figure 5.11). For example, the packaged ACL module 1 exhibits a comparable temperature when measured with *Setup 2* (red curve in Figure 5.11), as the MMIC when measured with *Setup 1* (blue curve in Figure 5.10). Therefore, it is only at the first glance surprising, that the ACL module 3 (blue curve in Figure 5.13) exhibits a noise temperature which is up to 30 K lower at 89 GHz, than the exact same MMIC that was mounted into the module, measured with the same setup (black curve). Furthermore, we have seen in Figure 5.2(b), that IAF's on-wafer measurements tend to yield more conservative noise temperatures. Since the 89 GHz ACL $V2$ is merely a variation of 89 GHz ACL $V1$, adapted for packaging but with the same ACL core (compare Figure 3.14), the temperature of 89 GHz ACL $V1$ measured by *Millilab* is also included into the graph. If now comparing *Millilab*'s on-wafer result with the module measurement with *Setup 2*, the increased noise temperature due to packaging losses can be explained conclusively.
This comparison is only done to demonstrate some essential findings of this work: Module

measurements can not be compared with on-wafer measurements, even when performed with the same setup. One reason is, that the calibration is done without the wafer probe and only the scalar loss of the probe is accounted for *after* the calibration. As was demonstrated with the previous results in this chapter, the ACL is very sensitive to the impedance it is connected too. And as explained in Chapter 4, the correct way to account for the wafer probe's loss would be to calculate its available gain with Equation 4.7, which is dependent on its matching and the source reflection. But the return loss of the probe on wafer side (Figure 4.8(a)) is about $10\,\mathrm{dB}$ worse, than of the isolator 4.7(a). Therefore, the method to account for the probe loss has only limited success and a comparison with module measurements is to be done with caution.
For the same reason, the *Millilab* on-wafer setup yields different noise temperatures than IAF's on-wafer setups (different probe), while *Setup 1* and *Setup 2* yield comparable results (same wafer probe).

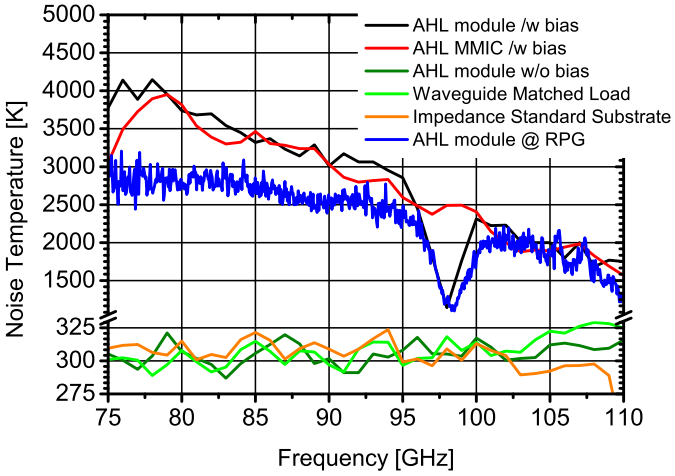

Figure 5.14: Noise temperatures of AHL MMIC and module, measured with *Setup 1*. As a reference, the measured noise temperatures of calibration standards were added in the graph.

The AHL module noise temperature was measured with *Setup 1* and compared to the on-wafer measurement with the same setup. This time, for the module a lower noise temperature would be expected than for the on-wafer result, because losses due to packaging would pull the noise temperature towards the ambient temperature. But again, this comparison needs to be done carefully. In Figure 5.14 the measured on-wafer temperature (red curve) and the module temperature (black curve) yield very similar results. It must be stated, that even a conservatively assumed loss of $1\,\mathrm{dB}$ associated with the packaging would merely yield a change of $75\,\mathrm{K}$ in the noise temperature, which would be difficult to identify in relation to the absolute temperatures of the AHL. Again, as a reference, the measured noise temperatures of an ISS, a calibration waveguide load and the AHL without bias are added in the graph. Furthermore, the measurement of the AHL module performed at RPG is included (blue curve). Not surprisingly anymore, it yields a different result, which can again be explained with the different dynamic power range in which different setups project the noise temperature, and the non-linearity associated with that. The dip at $98\,\mathrm{GHz}$ must be associated with the

assembly of the module. Since AHL module 1 was the only module assembled, this effect could not be investigated further.

5.2.1 Comparison of Active Load Modules to Conventional LNAs as a Load

Since the design approach for an ACL is very similar to the design of an LNA, it appears obvious to measure the noise temperature at the *input* of an LNA in the same way as the ACL.

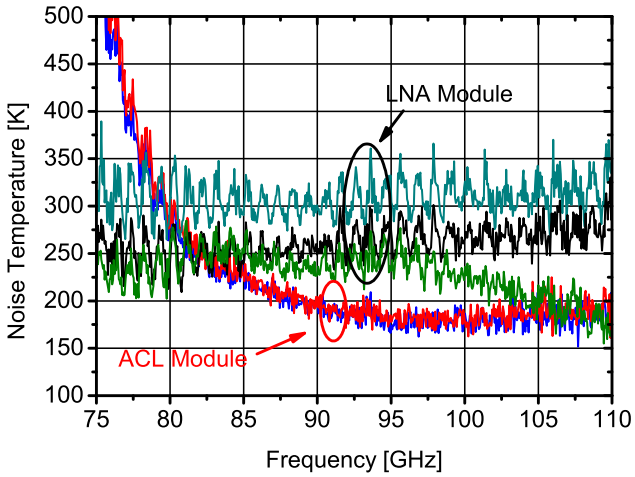

Figure 5.15: Comparison of an LNA module, measured at its input as a load, versus the ACL module 1. Measurement performed at RPG.

At RPG a double-LNA with around $40\,\mathrm{dB}$ small-signal gain was measured at its input port with the same setup as the ACL module 1. The LNA module contained an MMIC manufactured at IAF and packaged at RPG. For the measurement the output port of the LNA was terminated with a matched waveguide load. The LNA measurement result is depicted in Figure 5.15 for three bias states: $1.0\,\mathrm{V}$ (cyan curve), $1.2\,\mathrm{V}$ (black curve), and $1.5\,\mathrm{V}$ (green curve). It was also measured with voltages above, but while the increase up to $1.5\,\mathrm{V}$ yielded a reduction of noise temperature, it increased again for higher voltages. Therefore the other results are omitted in the graph. The ACL module was also measured in two different bias states, with $V_d = 0.6\,\mathrm{V}$, yielding an $I_d = 200\,\mathrm{mA/mm}$ (blue curve), and $V_d = 0.8\,\mathrm{V}$, yielding an $I_d = 266\,\mathrm{mA/mm}$ (red curve). The ACL module exhibits notable better noise temperature, than the LNA and more important, the ACL module is negligibly bias dependent compared to the LNA, whose noise temperature strongly depends on the bias. Furthermore, the effect of non-optimal input return loss of an LNA at the expense of good NF can be seen: The LNA noise temperatures are strongly oscillating due to reflected noise power between LNA and radiometer input. This demonstrates the main advantages of ACLs compared to LNAs. They are much less sensitive to bias variations and, that they obviously achieve much lower noise temperatures than standard LNAs typically do.

After this first initial comparison, further IAF-manufactured LNAs were measured with *Setup 1* and the results are shown in Figure 5.16. Since the modules include a bias control

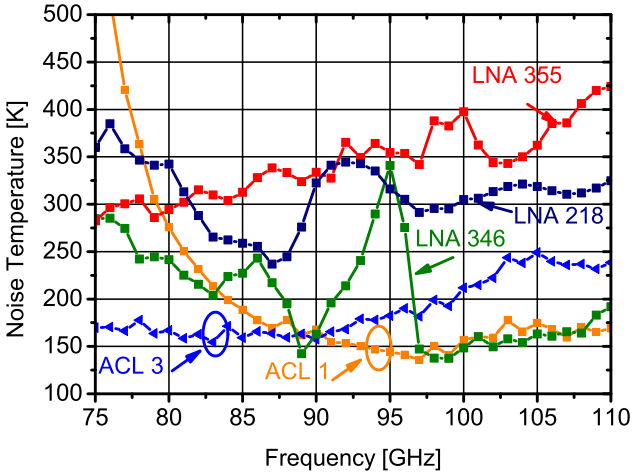

Figure 5.16: Comparison of three LNA modules, measured at their input as a load, versus the ACL modules 125-001 and 125-003. Measurements performed with *Setup 2*.

circuit, the exact voltages applied to the MMICs are not known. LNA 218 and LNA 355 posses a small-signal gain of around $20\,\mathrm{dB}$ and a NF between 3 and $4\,\mathrm{dB}$. LNA 346 is a double-LNA with around $45\,\mathrm{dB}$ gain and $4\,\mathrm{dB}$ NF. Its exact S-Parameter and NF are shown in Figure 5.17(a) and will be discussed shortly. The orange and blue curves show the measured noise temperature of ACL module 1 and ACL module 3, respectively. It can be seen, that standard LNAs exhibit a noise temperature around ambient or above at their input port. Furthermore, they exhibit a more or less strong ripple over the frequency range. The ACLs, in contrast, demonstrate a very continuous gradient of the noise temperature. Also, as we have seen before, they achieve a lower noise temperature. Merely LNA 346 achieves a comparable noise temperature above $94\,\mathrm{GHz}$, but has an notable peak at $95\,\mathrm{GHz}$. Therefore, it is investigated in more detail.

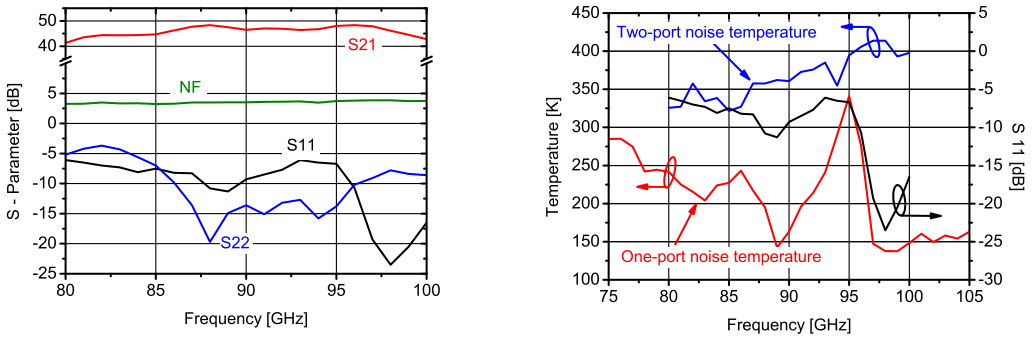

(a) Measured S-parameters and noise figure of LNA module 346.

(b) S11 versus one-port noise temperature measurement and standard noise measurement.

Figure 5.17: Investigation of LNA module 346.

Figure 5.17(a) depicts the S-parameters and NF of LNA 346. It can be seen, that for LNA design it is much simpler to achieve a good output matching (S22), than a good input matching (S11), because the impedance transformation for optimum noise is different than

for optimum power matching and a compromise needs to be chosen. If the LNA is used as a first stage in a receiver the reduced input matching is not too critical, as long as the LNA has enough gain. Typically the reflected power at its input does not affect the system performance. In exchange, prioritization of the optimum noise matching yields a flat NF below $4\,\mathrm{dB}$ (green curve). If this standard two-port measured NF is transformed into a noise temperature, using Equation 3.1, it can be plotted together with the one-port measured noise temperature at its input. In Figure 5.17(b), the noise temperature is depicted on the left scale and the $S11$ on the right scale. Now, the cause for the noise peak at $95\,\mathrm{GHz}$ can clearly be identified. It strongly correlates with the deteriorating $S11$ in the frequency range $90 - 97\,\mathrm{GHz}$, while the noise temperature is very low for a $S11$ below $-15\,\mathrm{dB}$. The other notable finding is, that the two-port NF does not correlate with the one-port noise temperature. This, one more time, emphasizes how important the input matching is for the one-port measurement of the noise temperature. While for LNA design the goal is to minimize the noise figure - which characterizes the amount of noise added by the device to the input signal at the *output* of the device - the goal of the ACL must be clearly different. The absolute noise temperature at the *input* is the relevant quantity and furthermore an extremely good input matching is mandatory. This clearly distinguishes ACLs from LNAs (at their input port) and justifies dedicated ACL designs. Only in one respect LNAs seem to have an advantage over ACL modules, which is the robustness against reflections from the measurement system. This is presented in the following.

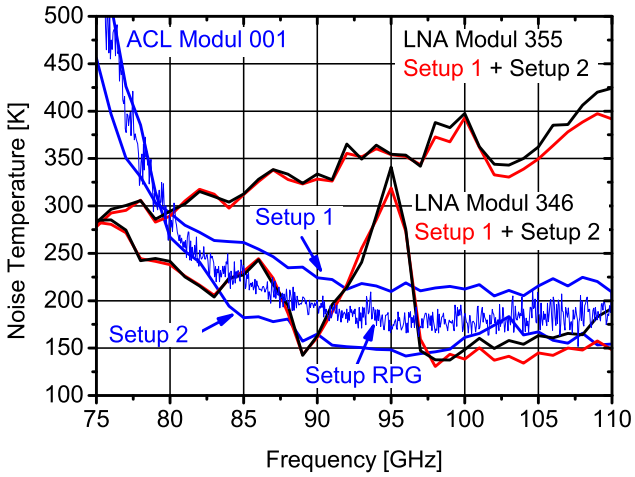

Figure 5.18: Comparison of two LNA modules, measured at their input as a load, versus the ACL module 125-001.

Since it was previously shown, that especially module measurements can yield different results with different setups, two of the LNAs were also measured with *Setup 1* and compared to all the previous measurements of ACL module 1. In Figure 5.18 all the results are summarized. While the explanation for discrepant results of different setups was based on the non-linearity of the power detector inside the NFA and different dynamic ranges, this measurements contradicts the previous argumentation. Obviously, only the ACL modules are susceptible to changes in the setup, while the LNA modules are very robust in this respect. We recall, that the *only* difference between *Setup 1* and *Setup 2* is the different receiver

module. The isolators and LNA 1 (see Figure 4.1), as well as the utilized instruments and calibration procedure are identical. Therefore, the only explainable source of this discrepancy is that some reflection at the mixer must leak back to the DUT, all the way thru two isolators and one LNA. This influence is obviously frequency dependent. The three noise curves of the ACL intersect at $80\,\mathrm{GHz}$ at around ambient temperature, while they diverge towards higher frequencies and lower noise temperatures. The latter leads to believe, that this effect is only seen at lower noise temperatures and therefore just hidden above ambient. But the two curves for LNA 346 are very similar up to $100\,\mathrm{GHz}$, where they also demonstrate a very low noise temperature, and only then slightly diverge. A similar divergence above $100\,\mathrm{GHz}$ is also observed for LNA 355.
This leads to the conclusion, that the ACL modules are more sensitive to mismatches and reflections in the setup, than LNAs.

5.2.2 ACL Module as Hot-Cold Load in Noise Measurements

As an alternative to standard noise measurements with a noise diode or with an antenna pointed at heated and cooled absorber, the ACL module can be used. When noise diode manufacturers deliver their calibrated diodes, they provide the associated ENR table. Since noise diodes have a moderate return loss, the manufacturers or suppliers only deliver the diodes with an isolator at its output and calibrate the combination of both components. The ENR table is then only valid for this combination. Similar to this procedure it is necessary to thoroughly characterize the ACL module *with* an isolator, before using this combination as a hot-cold load at the input of the DUT. The measured *cold* noise temperature of ACL module *and* isolator is then used to calculate the ENR of this combination. The *hot* state for the ENR calculation is when the ACL is switched off, the other way round as for ND. Of course the isolator reduces the ENR, but it is necessary, because in the *off* state of the ACL, its return loss is not defined and what the DUT *sees*, is the ambient noise of the isolator.

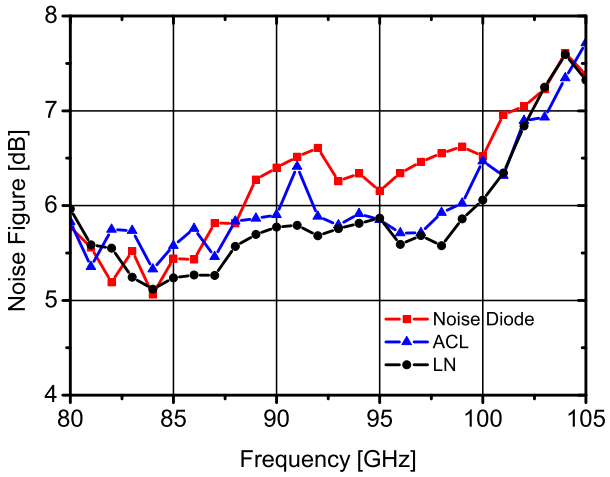

Figure 5.19: The noise figure of an amplifier was measured with three different methods: Noise diode, antenna with hot-cold (LN) load, and ACL in *on* and *off* state.

To validate this measurement method, an amplifier was chosen as a DUT and its noise figure measured. Therefore the combination of ACL and isolator was connected as a hot-

cold load to the input of the DUT while the output was connected to the NF measurement setup. With the known ENR of the hot-cold load, the NF of the DUT can be calculated with the Y-method. The same DUT was then measured with standard methods and the results are compared in Figure 5.19. When using the ND, one LNA had to be removed from the measurement setup, to avoid saturation of measurement system. This, again, demonstrates the advantage of an ACL for calibration of very sensitive receivers with high gain, as they are used in radiometers. Typically, the noise behavior of an amplifier changes continuously over frequency. Due to the ripple on the red curve (ND) and the blue curve (ACL), which are typical for noise power reflections, it is believed that the result achieved with the antenna and LN is the most accurate of the three. This can be explained with the measured return losses in Figure 4.7, where the antenna has an even better matching than the isolator in front of the ACL, thus reducing these reflections. The results of the measurement performed with the ACL as a hot-cold load and the LN measurement agree very well. Even the results achieved with the ND are comparable, diverging only in the center of the frequency range by less than $1\,\mathrm{dB}$. This impressively demonstrates the suitability of an ACL module as a hot-cold load for noise measurements and even points out its advantages compared to NDs.

5.2.3 Temperature Dependence of ACLs

When characterizing the sensitivity of the ACL to external physical temperature changes, the entire W-band was measured at each temperature step. For clarity sake only the results at the center frequency are shown. However, it should be noted that since the performance of the ACL is frequency dependent, the sensitivity to temperature changes as well.

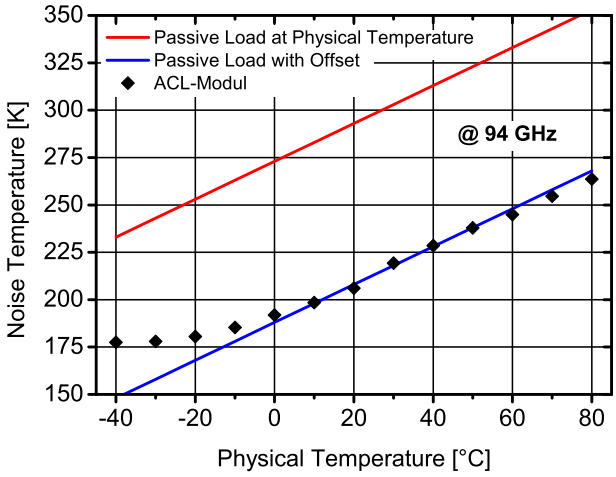

Figure 5.20: Measured noise temperature of ACL module at different physical temperatures compared to the theoretical value of a passive matched load. Measured with *Setup 1*.

The solid line in Figure 5.20 shows the noise temperature, which a passive matched load would exhibit at the accordant physical temperature. The slope of the curve is $1\,\mathrm{K}/^{\circ}\mathrm{C}$. For a better comparison to the sensitivity of the ACL, an offset was subtracted from this curve which corresponds to the difference between a passive load and the presented ACL at ambient temperature. In comparison to the dashed offset curve it can be observed that for physical

temperatures below ambient the ACL is less sensitive to temperature changes than a passive load, while for temperatures above ambient a similar behavior as for a passive load can be observed. While previous publications only investigated the temperature dependence above 0 °C ([34], [65]), this is the first work to analyze the ACL behavior below zero. If in accordance to previous work, a linear fitting curve is applied only for the measurement points above 0 °C, the slope of the curve is 0.9 K/°C. If in a similar fashion the measurement points below ambient temperature are fitted, an average dependence of 0.5 K/°C can be observed. Finally, if only measurements below zero are considered, a dependence of 0.36 K/°C can be derived. In the application scenario of an ACL as a calibration reference, however, such extreme temperature changes are not expected, since these systems are typically very accurately temperature stabilized. However, it is noteworthy, that the noise temperature of an ACL, being an active device, does not increase more than a passive load, when being heated.

5.3 Active Loads with Integrated Switches

5.3.1 Switching Calibration Front-End

One of the critical parameters of the SCFE depicted in Figure 3.20 is the insertion loss between the internal loads and the output port, which will deteriorate the achieved high or low temperature of the respective load. Due to the integrated design, it is however not possible to measure this loss directly. Therefore one of the through paths must be characterized and the loss added by the additional transmission line, to connect to the ports at the left edge, must be subtracted. The necessity of this layout was explained in Chapter 3. Since the two input channels of the SFCE are designed symmetrically, only the upper branch was characterized.

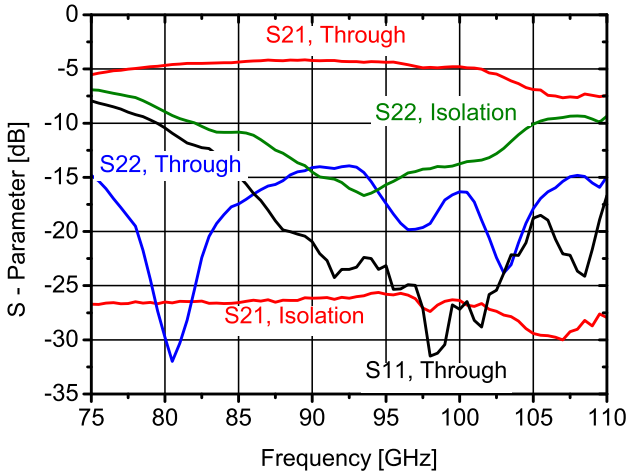

Figure 5.21: S-parameters between input port 1 and output port for switch position to input port 1 (through) and to internal matched load (isolation).

In Figure 5.21 S-parameter measurement results are shown, where port 1 is the input port and port 2 is the output port (compare with Figure 3.20). In *through* position all branches are closed ($V_{sw} = +0.1\,\mathrm{V}$), except for the upper input signal path ($V_{sw} = -0.5\,\mathrm{V}$). An

insertion loss between 4 and 5 dB is measured within the bandwidth of $80 - 100$ GHz. The line length difference of $1700\,\mu$m between the path from the internal loads and the path from input to the switch core yields a simulated added loss of -0.7 dB. This results in an estimated insertion loss of 3.3 dB at the center frequency for the two internal paths to the active loads. To measure the isolation of the SCFE, the output port is routed to the internal matched load and S-parameters are measured at the same ports as above. An isolation of more than -25 dB is measured within the entire W-band. Furthermore, the input return loss is very good in all switching states of the SCFE. Even though the $S11$ in the through position is measured at the input port 1 (black curve), it gives a good indication of the internal matching towards the internal loads. As previously shown, the very good matching of less than -15 dB will allow a good performance of the internal loads.

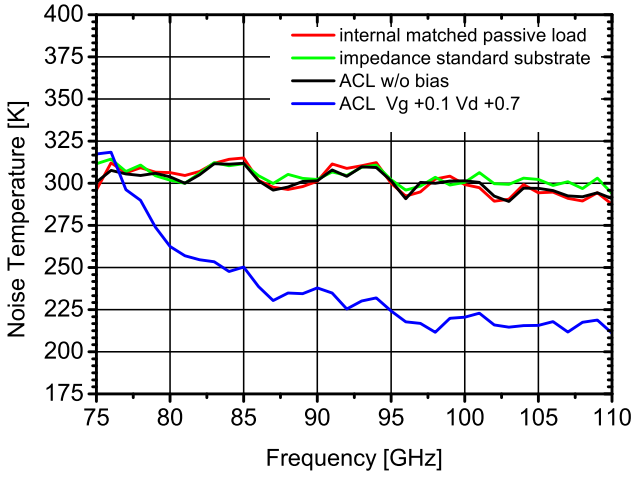

Figure 5.22: Noise temperatures in switch positions *ACL* and *passive load*, compared to standard substrate load and ACL without bias.

For the characterization of the cold reference on the SCFE, the SP5T switch was set to the accordant position. The ACL was biased with $V_g = +0.1$ V and $V_d = +0.7$ V, yielding a drain current of 173 mA/mm at which the lowest noise temperature was achieved. The result is shown in Figure 5.22 (blue curve), compared to measurement of an ISS (green curve). Furthermore, the noise temperature of the SCFE was measured when the SP5T is switched to the internal matched load (red curve) and switched to the ACL at zero bias. For the last two states it must be noted, that it can not be differentiated if it is really the noise temperature of the passive load, of the ACL without bias or the switch itself, since all are at ambient temperature. For frequencies above 90 GHz, the SCFE achieves a mean noise temperature of 220 K in the *cold* position. Compared with the measured temperature of 150 K of the stand-alone ACL, the increase of 70 K is due to the losses of the SP5T switch. The temperature change, due to a resistive loss is described by Equation 5.1.

$$T_2 = T_1 \cdot L_{lin} + T_0 \cdot (1 - L_{lin}) \tag{5.1}$$

For example, the cold temperature of the ACL before the switch would be T_1 and L_{lin} the linear loss of the switch at an ambient temperature T_0, then the cold temperature after the switch would increase to T_2. This of course also applies for a temperature T_1 above T_0,

e.g. for a hot load, then the resulting temperature is pulled down by the switch loss and T_2 decreases.

$$L_{dB} = 10 \cdot log_{10}(L_{lin}) = 10 \cdot log_{10}\left(\frac{T_2 - T_0}{T_1 - T_0}\right) \tag{5.2}$$

If the measured noise temperatures at $95\,\text{GHz}$ of the stand-alone ACL MMIC of $140\,\text{K}$ (see Figure 5.4(b)) and of the SCFE of $225\,\text{K}$ (see Figure 5.22) are inserted into Equation 5.2 as T_1 and T_2, respectively, the resulting loss yields $-3.35\,\text{dB}$. This is very close to the insertion loss, derived above from the *through* measurement by de-embedding the simulated line loss.

Unlike the AHL, the ACL is very insensitive to bias variations. The difference of the highest and the lowest achievable noise temperature with extreme bias conditions is less than $20\,\text{K}$ within the entire operation bandwidth. Figure 5.23 shows the achieved noise temperatures at different bias.

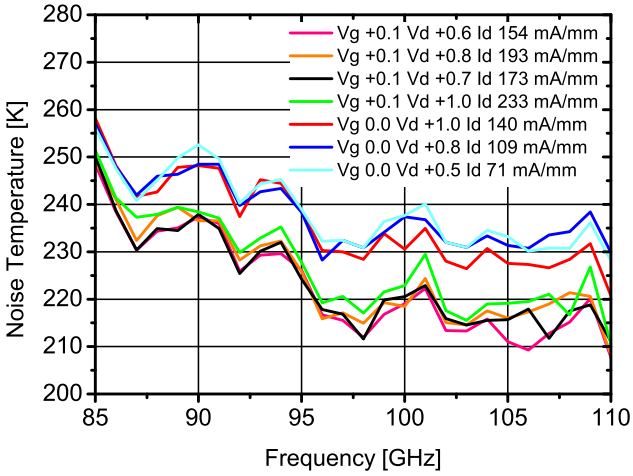

Figure 5.23: Noise temperatures in switch positions *ACL* at different ACL bias.

The hot reference on the SCFE was characterized accordingly, by routing the signal from the AHL to the output. In contrast to the ACL, however, it is possible to achieve different levels of noise temperature as a function of transistor biasing (see Figure 5.24). Again, the originally higher noise levels of the stand-alone AHL are reduced by losses of the SP5T, according to Equation 5.1. Nevertheless, noise temperatures as high as $1750\,\text{K}$ at $94\,\text{GHz}$ were achieved, measured at the output of the SCFE. Again measurements of an ISS and the SCFE switched to the internal load are included in the graph, as well as the temperature with zero bias AHL.

If the achievable ENR of the SCFE is calculated applying Equation 4.4, with $1700\,\text{K}$ for the *hot* and $225\,\text{K}$ for the *cold* state at $95\,\text{GHz}$, this yields an ENR of $7\,\text{dB}$. This is much higher, than an ENR achieved only with a cold and an ambient load and confirms the advantage of a SCFE for hot-cold calibration. A novel application of such a device could be to use it as a wafer-probe reference to calibrate a noise measurement setup. As described in Chapter 4, the state-of-the-art is to calibrate such a setup *without* the wafer-probe and then to account

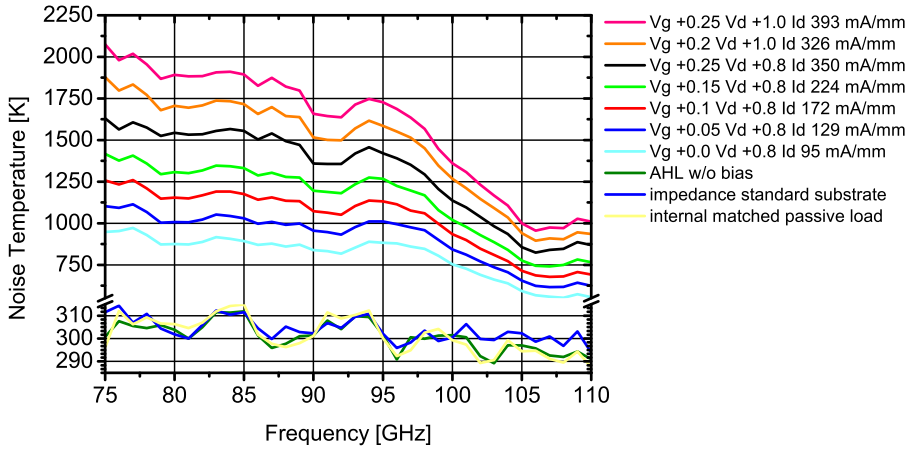

Figure 5.24: Noise temperatures in switch positions *AHL* at different AHL bias, compared to standard substrate load and AHL without bias.

for the loss afterward. The error introduced with this approach was discussed earlier in this chapter. With the SCFE presented in this work an *on-wafer* calibration of the setup could be performed. Reflections due the non-ideal matching of the wafer-probe would be accounted for during the calibration, yielding more reliable results. Furthermore, the variable *hot* noise temperature of the SCFE at different bias states of the AHL allows to extend the number of reference loads above three and to improve the calibration accuracy even more. However, it remains the necessity to analyze the influence of biasing and of temperature changes on the stability of the AHL and to calibrate the SCFE in the first place to calculate an ENR table.

5.3.2 Active Calibration Sub-System

The two versions of the ACSS presented in Chapter 3 were characterized similar as the SCFE. The S-parameters were measured at *Millilab* and on-wafer noise measurement were measured with *Setup 2* at IAF and with the *Millilab* setup. Figures 5.25 and 5.26 depict the S-parameters in different switching states for ACSS $V1$ and ACSS $V2$, respectively.

Since the SP3T of both versions is identical, the measured $S11$ and $S21$ for the through position are very similar, as well as the $S21$ for isolation, when the switch is set to the internal matched load. The $S22$ describes the matching at the output of the ACSS, which will be connected to the radiometer. It changes, depending on the switch position of the SP3T. The better matching of 89 GHz ACL $V4$ over 89 GHz ACL $V1$ at the design frequency (compare Figures 5.1(a) and 5.2(a)) also reflects in the ACSS results. In both cases the matching when switched to the ACL (orange curve) is better at 89 GHz, than when switched to the matched load (green curve) or the through path (blue curve). For ACSS $V2$, an ideal match of -25 dB was achieved at design frequency for the ACL switch position.

Figure 5.27 compares the achieved noise temperatures of ACSS $V1$ and $V2$, measured with the *Millilab* setup. As for the stand-alone MMICs, the first version achieved a lower noise temperature, while the prioritized design goal for the second version was the improved return loss. It can be observed, that the difference in noise temperature between the two ACSS versions is less, than between the respective stand-alone ACLs. This is explained by

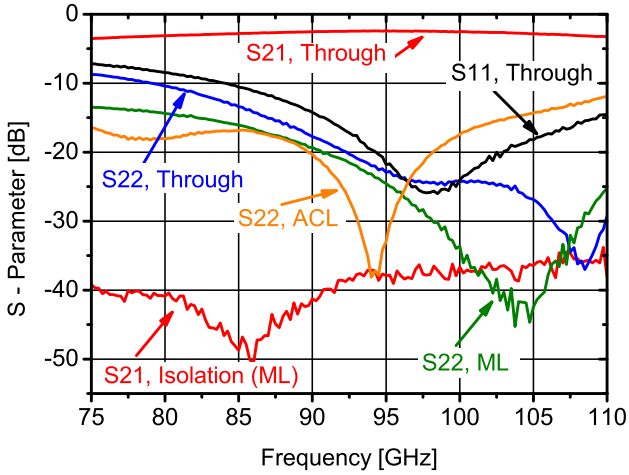

Figure 5.25: S-parameters of ACSS $V1$ in different switch positions.

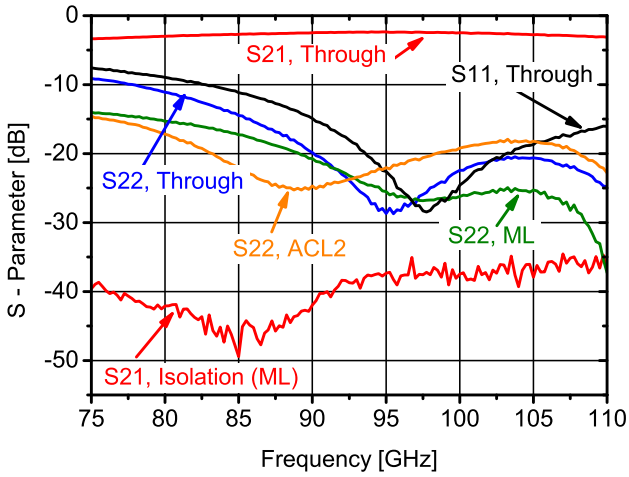

Figure 5.26: S-parameters of ACSS $V2$ in different switch positions.

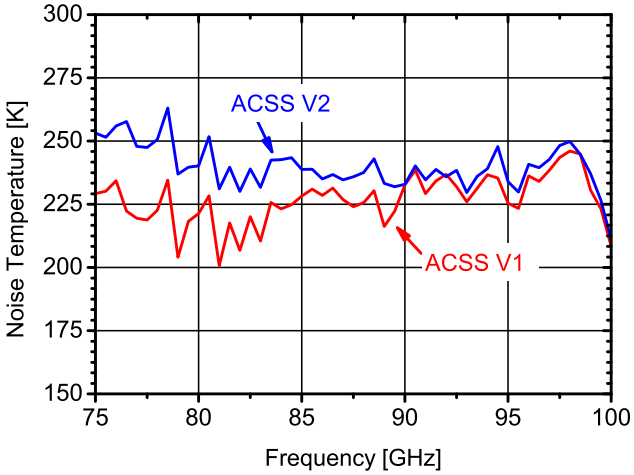

Figure 5.27: Achieved noise temperatures of ACSS $V1$ and ACSS $V2$ in switch position *ACL*, measured at *Millilab*.

the loss of the SP3T, which has a relatively higher impact on the lower noise temperature, than on the higher noise temperature ACL (compare Equation 5.1), pulling both towards ambient temperature.

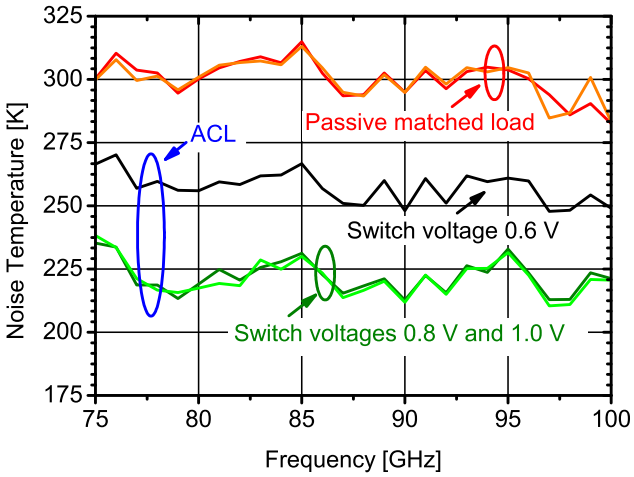

Figure 5.28: Noise temperatures of ACSS $V1$ in switch positions *ACL* and *passive matched load*, measured with *Setup 2* at IAF. If the switch is not supplied with the appropriate bias, the isolation breaks down and noise from the matched load leaks into the ACSS output.

Since the performance of the SP3T is crucial for the application of the ACSS, its influence on the achieved noise temperature in different switch positions was further analyzed. The bias threshold of the switch was tested and found to be around $+0.7\,\mathrm{V}$. For any voltage below this threshold, the FET switches does not shorten the signal to ground and the basic functionality of the SP3T is corrupted. The result is, that noise power from all three input channels is superposed at the star point and routed to the output of the ACSS. This effect is shown in Figure 5.28 for ACSS $V1$. The switches are set to route the ACL signal to the output and thus isolating the other two channels. The ACL is biased with $V_g = -0.2\,\mathrm{V}$ and

$V_d = +0.6\,\mathrm{V}$. For a switch bias of $+0.6\,\mathrm{V}$ the noise power of internal matched load and the input port leak into the output , increasing the measured noise temperature (black curve). For any switch voltage *above* the threshold, the isolation of the switch is identical, which is demonstrated in Figure 5.28 with $+0.8\,\mathrm{V}$ and $+1.0\,\mathrm{V}$ (green curves). This confirms the very important property of the designed SPxT switches, that their performance is not bias sensitive and thus not introducing an additional error source for the temperature references. The good isolation of the SP3T is also confirmed, when the switches are set to route the signal to the internal matched load. In this state, the noise temperature from the ACL must be isolated from the output. In Figure 5.28, the measured noise temperature at the output in this state is shown, while during one measurement the ACL was biased (orange curve) and during another measurement not biased (red curve). Both curves are very identical, proving that the internal low noise temperature of the ACL around $150\,\mathrm{K}$ does *not* influence the output noise temperature, due to good isolation.

It is notable, that the on-wafer measurements of ACSS show almost no difference between results achieved with the *Millilab* setup (Figure 5.27) and with the IAF setup (Figure 5.28). This indicates, that the loss of the switch in front of the ACL isolates the ACL from the output, making it less sensitive to the impedance of the setup. Furthermore, as for the characterization of the stand-alone ACL in 5.2(b), the comparison shows that the measures taken to reduce noise reflections in the setup, yield a smaller ripple on the temperatures measured with *Setup 2*.

In the course of the *Calload* project, ACSS $V1$ was selected for packaging due to the slightly better noise performance. Some tuning with bond wires during the assembly was done to improve the matching at the center frequency. The performance was good and a noise temperature of $227\,\mathrm{K}$ was achieved for the module, which is again equal to the value in on-wafer measurements. This is the same effect that was discussed in this chapter. The long-term stability of the ACSS was characterized with the highly temperature stabilized test-bed at *DA-Design* and was also very good.

5.3.3 Active Hot-Cold Load

The noise temperature measurements of the AHCL in cold and hot load switch biasing are shown in Figure 5.29. As for the two previously presented MMICs with integrated ACLs and switches, the loss of the SP3T increases the cold temperature and decreases the hot temperature, compared to the stand-alone circuit. For the simulation results shown in Figure 5.29, this loss was accounted for, by inserting the simulated SP3T loss and the measured noise temperature of the stand-alone circuit into Equation 5.1. Since the stand-alone ACL test-structure is measured with RF-pad, which has an insertion loss of about $0.3\,\mathrm{dB}$, and which is not employed in the AHCL, this value can be subtracted from the switch loss. This yields an effective insertion loss of 1.7 to $2.7\,\mathrm{dB}$. Thus, at $93\,\mathrm{GHz}$ where the stand-alone ACL provides a temperature of about $190\,\mathrm{K}$, an AHCL cold temperature of 225 to $240\,\mathrm{K}$ can be expected. This is in agreement with the measured AHCL cold temperature, as can be seen in 5.29. In the frequency range of 91 to $104\,\mathrm{GHz}$ the AHCL cold temperature is lower than $250\,\mathrm{K}$. The measured AHCL hot temperature has its maximum at $91\,\mathrm{GHz}$ with a temperature of $860\,\mathrm{K}$. When comparing measurement and simulation, it can be stated that the simulation was able to predict the AHCL temperatures at its center frequency. The measured noise power

bandwidth is not as large as the simulated, which can be explained by small frequency-dependent impedance mismatches between the ACL, SP3T and the additional switching periphery, which in total lead to a noticeable deviation of measurement and simulation. The AHCL has a power dissipation of $3.2\,\mathrm{mW}$, which is the same value as obtained with the ACL test structure. This very low power consumption can only be accomplished due to the fact that only one noise source is employed and that the switches have a negligible DC power consumption.

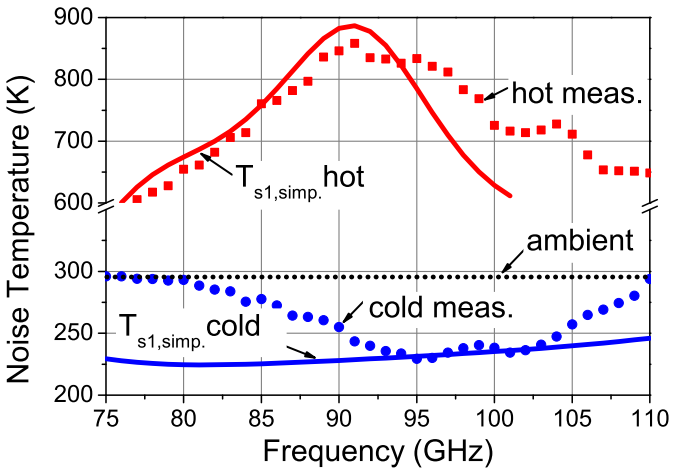

Figure 5.29: Measurement versus simulation of the AHCL's hot and cold noise temperatures. The dotted line indicates ambient temperature.

Summary and Conclusion

Designing the different active load circuits based on different simulation approaches, allowed to verify the suitability of each simulation method. It was shown, that the noise temperature discrepancies between simulation and measurement are also due to utilized measurement setup. Nevertheless, none of the simulation methods was found to be particularly superior or inferior to the others in terms of accuracy. However, the novel method presented in this work, has a significant advantage in terms of shorter design flow and faster numerical optimizer possibilities.
Furthermore, ambiguous noise temperature results were presented, but by cross-checking the measurements with many different setups, a fairly good understanding of the effects influencing one-port noise measurements was gained. It was found, that it is not sufficient to rely on one particular setup and that especially for short-term on-wafer and module measurements only an achieved temperature *range* can be derived from the actual measurement results. Overall, state-of-the art noise temperatures were achieved for all presented active loads, even if the measurement setup yielding the higher result was considered. Also, the W-band ACLs presented in this chapter are the first active loads at such high frequencies. A comparison to previously published stand-alone ACLs will be given at the end of the next chapter, after the D-band ACL results were presented.
After the difference between LNA and ACL designs was pointed out, packaged ACLs were characterized and compared to LNAs as a load. With the result, that not only the suitability

of an ACL as a calibration reference was demonstrated, but also its advantages compared the conventional loads were emphasized. It was shown that an ACL module can be used to perform noise measurements on LNAs, yielding comparable results as with noise diodes. The behavior of an ACL for below zero ambient temperatures was investigated for the first time and the results compared to previous work which only analyzed the temperature dependency for above zero.
Since this work is the first one to present an active *hot* load based on a FET, it was possible to integrate cold, ambient and hot loads into integrated switching calibration front-ends. Different implementations of such front-ends were developed and characterized. If the noise performance due to the switch losses and the herewith associated temperature increase is suitable for future space mission instrumentation has to be investigated in future work. But no similar highly integrated calibration front-ends based on MMIC technology are known up to date and a patent was granted [78].
It will be demonstrated in the following chapter, that the state-of-the-art noise performance of the presented ACLs in this chapter and the concept of integrating FET switches, is not only limited up to W-band frequencies, but also outstanding results can be achieved even up to $150\,\mathrm{GHz}$.

6 Characterization of D-Band Active Load MMICs

Similar to the presented results in the previous chapter, the designed D-band active load circuits were characterized with the on-wafer measurement setup described in Section 4.4. None of the D-band active load MMICs were assembled in a package, therefore the results are limited to on-wafer measurements. The designed D-band LNA necessary for the measurement setup, however, was of course mounted into a module, as depicted in Figure 3.27. Therefore, S-parameter and noise figure measurements of the LNA module 667 are presented, in addition to on-wafer results of the mounted MMIC which are compared to the simulations.

6.1 LNA Module for Measurement Setup

Just as all the developed active loads, the LNA was designed using IAF's proprietary model library, which, at the time of the LNA design, was based on extractions from measurements up to $110\,\text{GHz}$. The results of the S-parameters and the noise figure simulated in ADS are shown in Figure 6.1 (solid lines) and compared to on-wafer S-parameter measurements (dashed lines). The applied voltages for the measurement were $-0.1\,\text{V}$ at the gate and $0.8\,\text{V}$ at the drain, yielding a drain current density of $430\,\text{mA/mm}$. This results in a total DC power consumption of 41.3 mW. The simulation shows a very flat gain of around $23\,\text{dB}$ over the entire D-band, whereas the measurement result exhibits a slowly decreasing gradient from about $26\,\text{dB}$ at $110\,\text{GHz}$ to $16\,\text{dB}$ at $170\,\text{GHz}$. Also, the input and output return losses show some discrepancy between simulation and measurement. These inconsistencies might be due to the limitation of the modeling data up to $110\,\text{GHz}$. However a good matching of below -$10\,\text{dB}$ was achieved over the bigger part of the D-band.

More important for the purpose of this work, however, is the performance of the LNA *module*, since especially the noise figure and the input matching of this component are ultimately responsible for the evaluated measurement setup described in Section 4.4. Remember, that the chip layout and packaging explained in Section 3.5 allows to bias the first two transistor stages and the subsequent two stages with different drain voltages. The programmable DC-control board was set to supply $+0.8\,\text{V}$ at stage 1 and 2 and $+1.0\,\text{V}$ at stage 3 and 4, while all gates are biased with $-0.1\,\text{V}$. Figure 6.2 shows the measured S-parameters and noise figure of LNA module 667. It exhibits a small-signal gain (S21) of far above $20\,\text{dB}$ in a frequency range of $50\,\text{GHz}$ and covers the entire D-band with a linear gain of more than 15 dB. Input- and output return losses (S11 and S22) of the LNA are better than $-5\,\text{dB}$ in the entire band and mostly below $-10\,\text{dB}$. This makes it ideal for the purpose of any kind of broadband measurement setup. The gradient in the gain can be observed again and is identical to the on-wafer measurement. Above $150\,\text{GHz}$, the performance of the LNA in terms of small-signal gain and S11 deteriorates, which is not critical, because the frequency

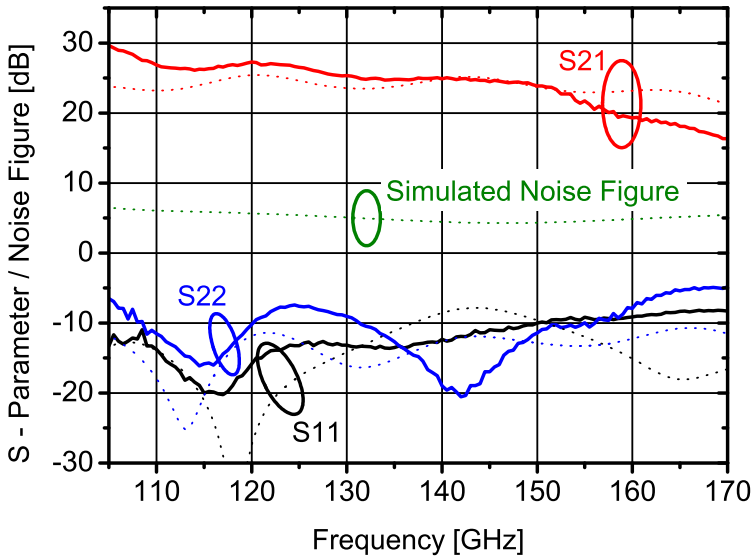

Figure 6.1: S-Parameter of D-band LNA MMIC.

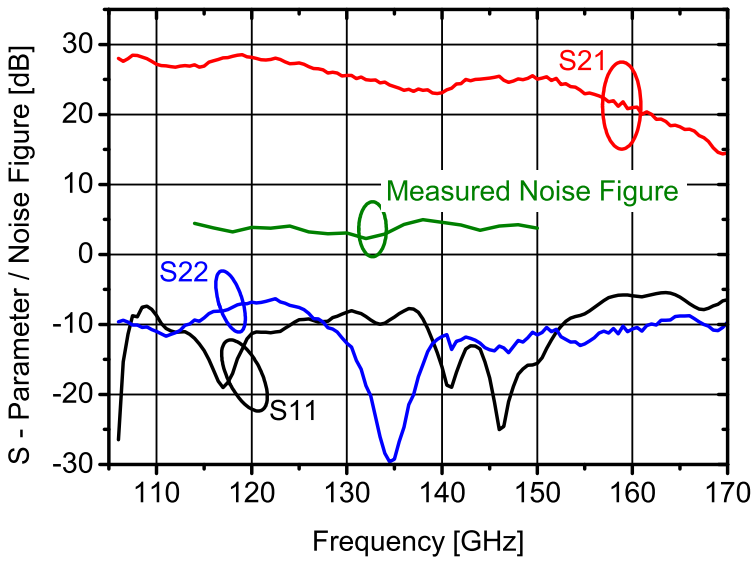

Figure 6.2: Measured S-Parameters and Noise Figure of D-band LNA module 667.

range of the measurement setup is limited by the used mixer. Losses due to the packaging and the waveguide transitions are compensated by the modified operating voltages. The noise figure measurement was performed with a re-calibrated ISSN-06 noise diode from *Elva*. The setup allowed measurements in the frequency range from $113 - 150$ GHz, again limited by the mixer, where the LNA module achieves a state of the art noise figure of below 5 dB and even below 4 dB between 115 and 135 GHz. This validates the usability of this LNA module for the dedicated one-port noise measurement setup even in a much wider frequency range, than was finally achieved due to the limitations described in Section 4.4. In the relevant frequency range for the following ACL characterization, a slightly lower noise figure than 5 dB is measured, which is consistent with the achieved system noise figure of the measurement setup around 6 dB (see Figure 4.16), that includes the additional loss of the isolator at the first stage. Furthermore, the input return loss (S11) is best in the frequency range $140 - 150\,GHz$, which is the range where the one-port noise measurement setup has the smallest ripple and therefore the results presented in the following are the most reliable.

Even though the expected input power at the first stage LNA module is extremely low, it should be considered, that radiometers or one-port noise measurement systems are cascading several high gain LNA stages and that a linear behavior of *all* stages must be assured. Therefore, it is important to know the large signal characteristics of the LNA when dimensioning the measurement system to provide enough dynamic range. Linearity measurements were performed at the center frequency of 140 GHz. Figure 6.3 shows the measured output power and the calculated gain for input power from -25 dBm to -11 dBm. The 1-dB compression point is located at -22 dBm input power, which for the expected noise power to be measured gives enough headroom even for the second stage LNA.

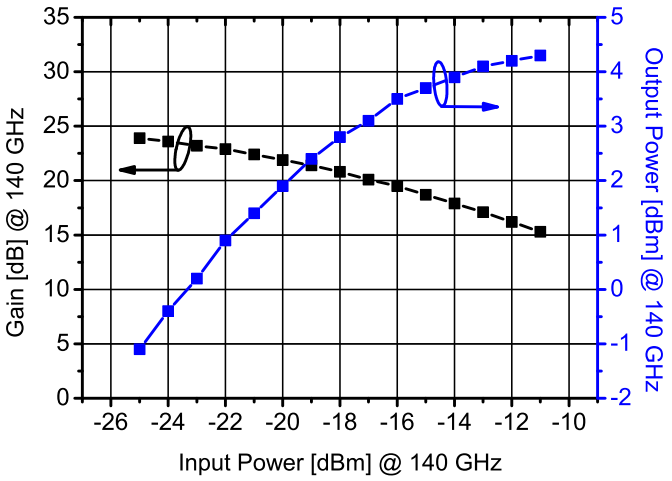

Figure 6.3: Measured output power and gain of the D-band LNA module 667.

Compared to other published work on LNAs in various technologies, this work achieves some outstanding figures of merit (FOM). Figure 6.4(a) shows the gain-bandwidth product of several published LNAs at their center frequencies. The gain-bandwidth product of the LNA of this work is marked with the red star. Since this figure presents the *absolute* bandwidth, similar FOM as in this work were achieved at higher frequencies. In D-band, however, the LNA of this work has a very prominent position in the FOM, especially because

it covers the *entire* band with a gain of around $20\,\mathrm{dB}$. Figure 6.4(b) shows the published noise figures of LNAs in several semiconductor technologies. Note that accurate noise figure measurements at these frequencies are challenging and not all published work can present their noise figures. Also, most of the noise figures in Figure 6.4(b) were measured on-wafer, neglecting the degradation associated with waveguide packaging. But most important, the other LNAs in this second FOM have typically a very narrow bandwidth, because their low-noise performance is optimized for a certain frequency region, depending on the intended application.

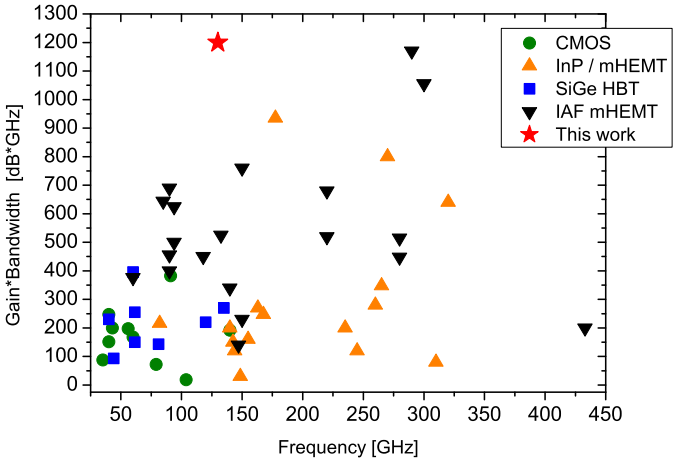

(a) Product of gain and bandwidth of published LNAs.

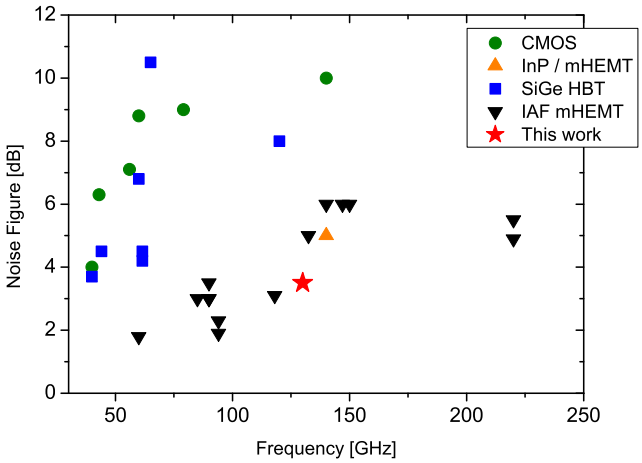

(b) Noise figures of published LNAs.

Figure 6.4: State-of-the art for LNAs.

6.2 Active Cold Load MMIC in D-Band

Having the LNA presented in the previous section available, the D-band ACL has been characterized using the setup described in Section 4.4. Due to the limitations thoroughly

elaborated in that section, no reliable results are expected in the lower part of the measured bandwidth. Therefore, this area in the following result figures is shaded, but still shown, to illustrate the effects discussed in Chapter 4. First, the noise temperature of the stand-alone ACL, as illustrated in the chip photograph in Figure 3.24(a), is shown. In Figure 6.5, the noise temperature at different bias conditions is plotted versus the frequency. An outstanding noise temperature of around $150\,\mathrm{K}$ is achieved, which is in fact similar to the results of the presented W-band ACLs. Also, as for the W-band loads, the resulting noise temperature is not very sensitive to different bias conditions. Merely at a high drain current density of $283\,\mathrm{mA/mm}$ (red curve), the noise temperature is noticeably increased.

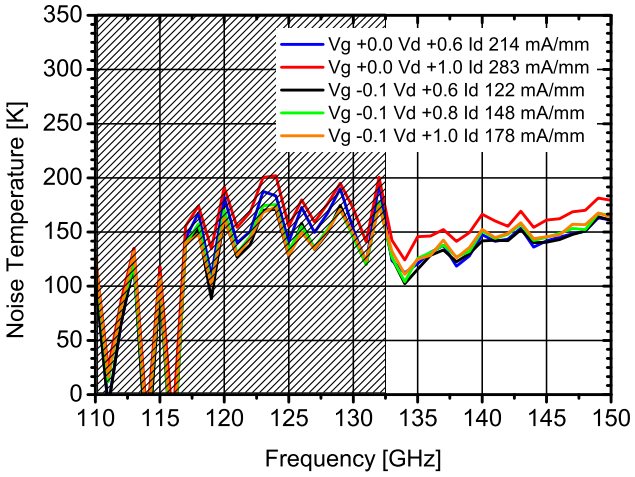

Figure 6.5: Measured noise temperatures of D-band ACL at different bias.

To better evaluate this bias dependency, Figure 6.6 depicts the noise temperature at $145\,\mathrm{GHz}$ versus the drain current density. At all measured points below $214\,\mathrm{mA/mm}$, the ACL achieves a noise temperature below $150\,\mathrm{K}$ and exhibits a very flat curve, proving a behavior not too sensitive to bias changes. As was repeatedly pointed out in the previous chapters, this is a crucial property of an ACL when it is intended to be used as a reference load.

For a deeper analysis of the influence of the bias conditions, Figure 6.7 shows the noise temperature for different drain voltages versus the gate voltage. Obviously, a higher drain voltage favors a noise temperature increase, even if the gate voltage controls the drain current to be low. The left measurement point at the red $1\,\mathrm{V}$ curve represents the temperature at a drain current density, regulated by the gate voltage, of $178\,\mathrm{mA/mm}$. For a drain voltage of $0.6\,\mathrm{V}$, however, even at a higher drain current density of $214\,\mathrm{mA/mm}$, a lower noise temperature is achieved (right measurement point at the blue curve). This is an important finding, because it confirms that the noise temperature exhibited by an ACL is not mainly dependent on the drain current, but that the appropriate bias setting of the transistor needs to chosen to assure the reflection coefficients on that the ACL design was based in the simulations. Less surprisingly, it can be seen, that within one fixed drain voltage setting, the noise temperature can be increased by increasing the drain current (controlled by the gate voltage).

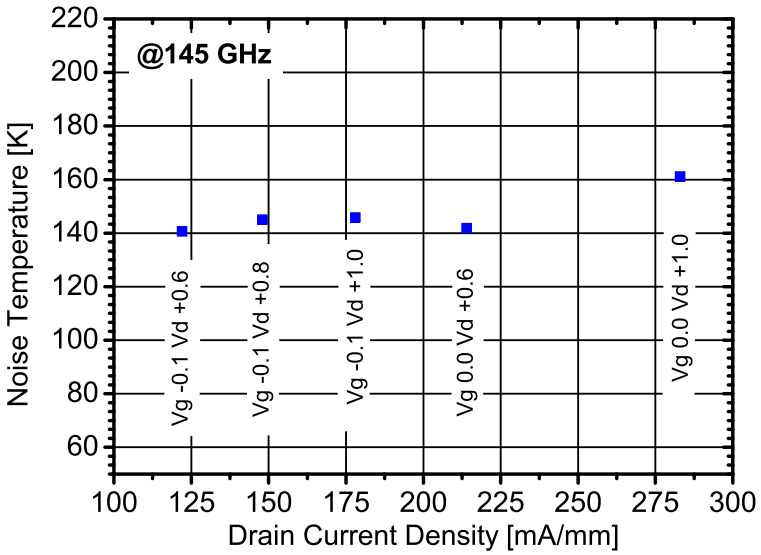

Figure 6.6: Measured noise temperatures of D-band ACL at $145\,GHz$ versus drain current density.

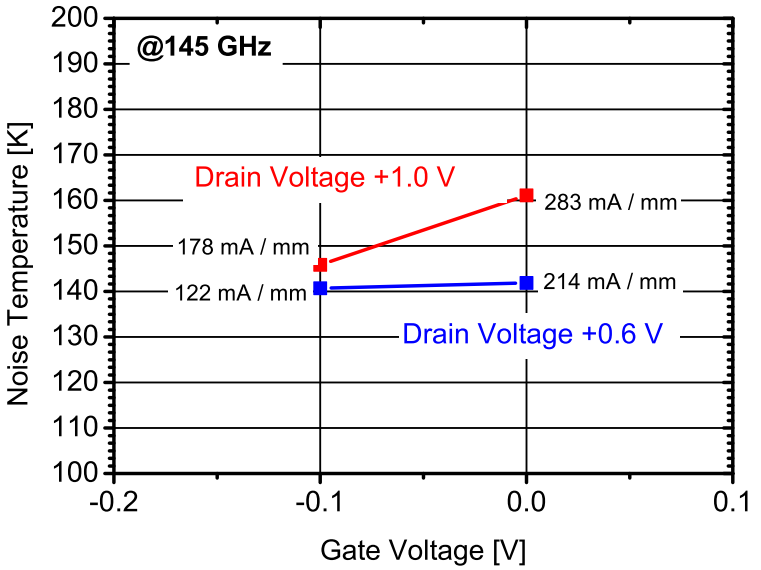

Figure 6.7: Measured noise temperatures of D-band ACL at $145\,GHz$ versus gate voltage.

Similar to the SCFE or the ACSS presented in Section 5.3, the stand-alone D-band ACL was integrated on one MMIC together with a SP2T and a matched load (ML), as illustrated in Figure 3.24(b). Figure 6.8 shows as a result the noise temperatures measured at the MMIC output during the two possible internal switching states. For comparison, the noise temperature of the stand-alone ACL is included into the graph (black curve). When switched to the internal matched load, the resulting noise temperature corresponds as expected to the ambient temperature, but only for frequencies above 140 GHz. This is explained by the fact, that the matching of the SP2T towards the two loads and towards the output is most critical. Reflected noise power will superimpose and cause noise peaks as seen at 133 GHz in both curves (red and blue). When switched to the internal ACL, the output noise temperature of the MMIC is reduced about 100 K. Due to the very low noise of the ACL core at 137 GHz (see black curve), the peak seen in the red curve at this frequency is even compensated, so that the noise temperature of the device when switched to the ACL (blue curve) is around 200 K and the noise temperature curve very flat from 135 GHz to 150 GHz. If now the noise temperature of the stand-alone ACL is compared to the ACL integrated with the SP2T, a mean difference of approximately 50 K can be observed. This increase is due to the losses of the switch and the internal lines for signal routing. To calculate the loss associated with this temperature increase, Equation 5.2 is applied again with the temperatures $T2 = 200$ K and $T1 = 150$ K, which roughly correspond to mean values of the blue and black curves. This results in a calculated loss of 1.8 dB. At 140 GHz, where the SP2T was originally centered and hence the difference in temperature between stand-alone ACL and the integrated version is the smallest ($T2 = 180$ K and $T1 = 145$ K), the calculated loss is as low as 1.1 dB. These are remarkable values for a D-band SP2T based on FETs and are also due to the very compact design of the integrated switch and ACL and the short internal transmission lines.

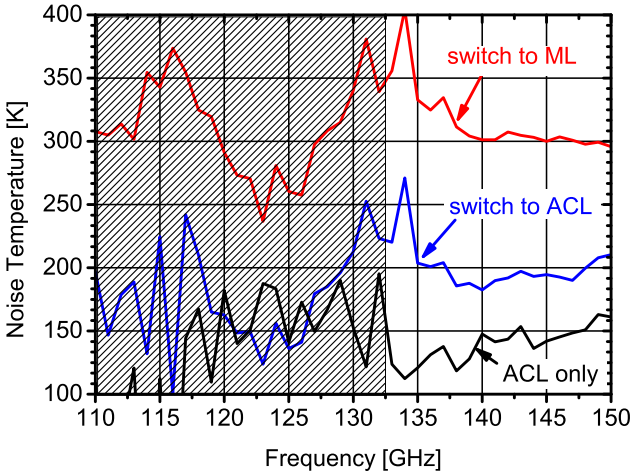

Figure 6.8: SP2T switch with integrated matched load and D-band ACL.

Summary and Conclusion

As mentioned in Section 3, ACL noise temperatures of 180 K on MMIC level were predicted at 100 GHz in [26] and assessed to be feasible for the use as reference loads in Post-EPS

context. The presented ACLs in this chapter were characterized up to $150\,\mathrm{GHz}$, yielding a state-of-the art noise temperature of below $150\,\mathrm{K}$ on MMIC level. Figure 6.9 compares the noise temperatures of all stand-alone ACLs, designed and characterized in the course of this work to all previously published ACLs in different technologies. It is notable, that a similarly low noise temperature in D-band was achieved, as with the best of the designed W-band loads.

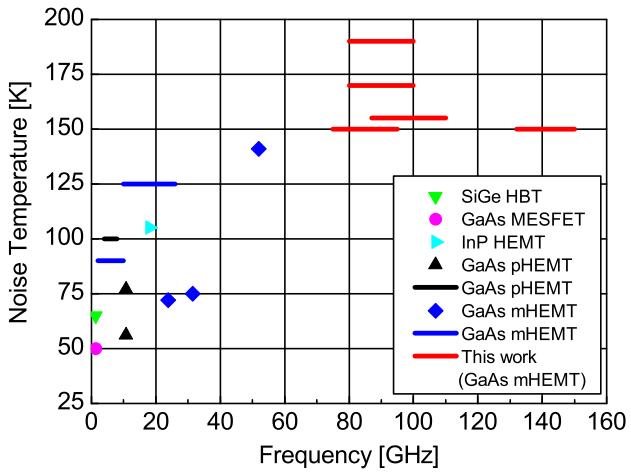

Figure 6.9: State of the Art of previously published ACLs compared to the ACLs of this work.

7 Conclusion

In summary, two goals are of particular importance for the calibration of radiometer systems: For the more scientific application of remote sensing it is to increase the radiometric accuracy, while for the more mass-market oriented application of PMMW imaging, e.g. in security scanners, it is the goal to increase the repetition rate of the calibration procedure. The first goal can be achieved by using references with noise temperatures in the vicinity of the expected target or measurement range. This not only avoids extrapolation errors and non-linear behavior of the receiver, but also improves the radiometric resolution, being an equally crucial parameter in radiometry. The second goal can be achieved by placing fast and reliably operating switches before the receiver, to switch between the references and the receiving antenna (or multiple receiving channels).
Consequently, this work has presented active electronic loads, that are covering a wide range of noise temperatures, encompassing the dominant measurement range in radiometric applications. In addition, for the first time such loads were integrated together with front-end switches on the same MMIC technology at frequencies as high as 150 GHz.
Even though the effect of a cold appearing transistor was described more than 30 years ago, only few such circuits were published since then. As a result, no established design guidelines were available at the beginning of this work, but only few publications - all with different simulation approaches. Therefore, part of this work was to compare and evaluate the known noise temperature calculation from previous work. It has been demonstrated with a 89 GHz ACL design, that several simplifications of the general calculation presented in [71] are allowed, if a deviation of 5% from the original temperature calculation is acceptable. A mandatory requirement for these simplifications is to design very good matching networks, to reduce the impact of reflections at the external terminals of the load. However, it was found, that even with the best realistically achievable matching networks, a remaining influence on the backward gain and thus on the generated noise at the transistor gate can not be avoided. This observation is of course based on the simulations with the available transistor model and passive components library.
No matter which of the previously known simulation methods are used, they require to iteratively design the output and input matching networks, before the resulting noise temperature can be simulated. If applicable, several re-design loops might be necessary to optimize the noise temperature result. The required design-flow is therefore very time-consuming. To overcome this, a novel one port noise temperature simulation method was presented in this work, which can directly calculate the resulting noise temperature, while modifications at the matching and supply networks are done. This allows to benefit from the possibilities of optimization algorithms which are part of modern numerical simulation tools.
More important, than the relatively small differences in simulated noise temperature between the different simulation methods, is the variation found during characterization of the active load circuits. Even more than regular noise measurements of amplifying two-port devices, the characterization of one-port low-noise loads was found out to be particularly challenging.

The results of the measurements were very sensitive to the utilized setup and a thorough analysis and selection of the crucial components was necessary to assure accurate results. It can be stated, that even if all measures are taken, to minimize the influence of the measurement system itself and to reduce all inherent errors, it is not safe to rely on the absolute accuracy of the measurement result. This was found out by cross-checking some selected results with independently designed measurement systems of other research facilities in that field. Also, for one of the two alternative measurement setups, a different calibration method (heated waveguide) was used. A comparison and discussion of the discrepant results lead to the conclusion, that none of utilized setups can be considered as superior to another. And in consequence, that a stated noise temperature of an active cold load is only accurate for the utilized setup, or, that it is only valid within a certain accuracy range. This was a major finding of this work.

Knowing this, the designed circuits were characterized and state-of-the-art results for active cold loads in W-band and D-band were presented. The lowest up to now published noise temperature of $50\,\mathrm{K}$ at a frequency of $1.4\,\mathrm{GHz}$ is only $100\,\mathrm{K}$ lower, than the noise temperature presented in this work at a frequency one hundred times higher ($140\,\mathrm{GHz}$)! For the highest previously reported frequency of an ACL ($52\,\mathrm{GHz}$), a temperature was achieved, which is only less than $10\,\mathrm{K}$ lower than the result of this work! It is remarkable, that the lowest achieved temperatures for the presented D-band loads are similar to the achieved temperatures for the W-band loads. Since the same technology, the same design-flow, and the same characterization method was applied, this might lead to the conclusion, that a similar noise performances might be reached even at higher frequencies. This might be one focus of future work.

In addition to the realized cold loads, an active hot load was presented for the first time. It does not achieve as high noise temperatures as noise diodes, which is in fact even a disadvantage of noise diodes in the context of radiometer calibration. The dynamic range of the by nature very sensitive radiometers is not suited for the calibration with noise diodes in general. Instead, the diode's relatively high noise power is reduced by implementing attenuators before feeding it to the radiometer input for calibration. The active hot load, however, provides a convenient noise temperature, which advantageously expands the hot-cold range for the two-point calibration, especially when combined with an active cold load. Furthermore, the AHLs can be manufactured with the same mHEMT technology as the cold loads, and, as a matter of fact, as existing multiple-throw FET switches. Consequently, integrated active hot-cold loads were developed, that allow to switch internally between the references. For this novel approach, a patent was granted. It should be noted, that the long-term stability and the bias dependency of active hot loads were not extensively investigated in this or previous work. This might be another topic for future studies.

To add a third reference to such a switching calibration front-end, an impedance-matched NiCr resistor was included, that exhibits a noise temperature equivalent to the physical temperature of the MMIC. By adding a third calibration reference, the error due to a non-linear behavior of the radiometer can be further reduced. By including a temperature sensor on the MMIC, not only the exact temperature of the passive load could be monitored, but also the possible influence on the active loads could be accounted for. This idea was also part of the granted patent. The sensitivity of the ACL to its physical temperature, however, was investigated as part of this work and found to be less than for a passive load.

If even more internal references are desired, another idea shall be presented as an outlook: Covering a certain temperature range with the active cold and hot load, respectively, it is possible to generate any arbitrary temperature in between. For that, several delay lines with different losses could be placed between the load and the output towards the radiometer and switches would select which delay line to loop into the reference path. By that, the noise temperature of the active load would be pulled towards the physical temperature of the lines and reduce (for an AHL) or increase (for an ACL) the temperature at the output by an amount equivalent to the loss of the correspondent line. Since the loss is only dependent on the physical length of the lines, the difference between the multiple generated references will always be stable, assuming all the lines are at the same physical temperature.
Another promising application of the developed calibration MMICs in this work, is the use as a reference in on-wafer noise-measurement systems. Once such a hot-ambient-cold MMIC is thoroughly characterized, it could be used similar to an impedance standard substrate. Typically the receiver is calibrated at waveguide level before the wafer-probe is connected, just as it was done in this work. The disadvantage is, that the probe is not part of the calibration loop and as it was clearly demonstrated in this work, especially on-wafer measurements are afflicted with large errors, because the poor matching on probe-side is greatly influencing the noise temperature measurement. With the proposed calibration on wafer-level, using a hot-cold reference MMIC, this error could be effectively reduced.

References

[1] R. H. Dicke, "The measurement of thermal radiation at microwave frequencies," *Review of Scientific Instruments*, vol. 17, pp. 268 –275, july 1946.

[2] M. Tiuri, "Radio astronomy receivers," *Antennas and Propagation, IEEE Transactions on*, vol. 12, pp. 930 – 938, dec 1964.

[3] N. Skou, *Microwave radiometer systems: design and analysis*. Artech House, 1989.

[4] B. Vowinkel, *Passive Mikrowellenradiometrie*. Friedr. Vieweg und Sohn Verlagsgesellschaft, 1988.

[5] F. T. Ulaby, R. K. Moore, and A. Fung, *Microwave Remote Sensing - active and passive*. Artech House, Norwood MA, 1981.

[6] S. Kazama, T. Rose, R. Zimmermann, and R. Zimmermann, "A precision autocalibrating 7 channel radiometer for environmental research applications," *Journal of Remote Sensing Society of Japan*, vol. 19, no. 3, pp. 265 – 273, 1999.

[7] T. Rose, S. Crewell, U. Löhnert, and C. Simmer, "A network suitable microwave radiometer for operational monitoring of the cloudy atmosphere," *Atmospheric Research*, vol. 75, pp. 183 – 200, May 2005.

[8] T. L. Wilson, K. Rohlfs, and S. Hüttemeister, *Tools of Radio Astronomy*. Springer-Verlag, fifth ed., 2009.

[9] R. Wilson, "The cosmic microwave background radiation," *Nobel Lecture*, December 1978.

[10] A. R. Thomson, J. M. Moran, and G. W. Swenson, *Interferometry and Synthesis in Radio Astronomy*. Wiley, second ed., 2001.

[11] A. Hulsmann, A. Tessmann, A. Leuther, I. Kallfass, E. Weissbrodt, M. Knelangen, M. Schlechtweg, and O. Ambacher, "Integrated circuits beyond 100 ghz for stand-off detection of concealed weapons," in *Fraunhofer VVS Future Security 2010 - 5th Security Research Conference*, pp. 74–77, 2010.

[12] M. Peichl, S. Dill, M. Jirousek, and H. Suess, "Passive microwave remote sensing for security applications," in *Radar Conference, 2007. EuRAD 2007. European*, pp. 32–35, 2007.

[13] A. Luukanen, L. Gronberg, T. Haarnoja, P. Helisto, M. Leivo, A. Rautiainen, J. Penttila, J. Bjarnason, C. Dietlein, and E. Grossman, "Passive broadband terahertz camera

for stand-off concealed threat identification using superconducting antenna-coupled microbolometers," in *Microwave Conference, 2008. EuMC 2008. 38th European*, pp. 943–946, 2008.

[14] L. Yujiri, M. Shoucri, and P. Moffa, "Passive millimeter wave imaging," *Microwave Magazine, IEEE*, vol. 4, pp. 39 – 50, sept. 2003.

[15] L. Gilreath, V. Jain, H.-C. Yao, L. Zheng, and P. Heydari, "A 94-ghz passive imaging receiver using a balanced lna with embedded dicke switch," in *Radio Frequency Integrated Circuits Symposium (RFIC), 2010 IEEE*, pp. 79 –82, may 2010.

[16] A. Luukanen, J. Ala-Laurinaho, M. Leivo, D. Gomes-Martins, M. Gronholm, J. Hakli, P. Koivisto, S. Makela, P. Pursula, P. Rantakari, M. Sipila, J. Saily, A. Tamminen, H. Toivanen, R. Tuovinen, A. Rautiainen, and A. Ra?isa?nen, "Developments towards real-time active and passive submillimetre-wave imaging for security applications," in *Microwave Symposium Digest (MTT), 2012 IEEE MTT-S International*, pp. 1–3, 2012.

[17] J. Richter, D. Notel, F. Kloppel, J. Huck, H. Essen, and L. Schmidt, "A multi-channel radiometer with focal plane array antenna for w-band passive millimeterwave imaging," in *Microwave Symposium Digest, 2006. IEEE MTT-S International*, pp. 1592–1595, 2006.

[18] W. G. . of the Joint Committee for Guides in Metrology (JCGM/WG 2), "International vocabulary of metrology - basic and general concepts and associated terms (vim)," tech. rep., Joint Committee for Guides in Metrology, 2008.

[19] ESA, "Calibration loads for radiometers," statement of work, European Space Agency, August 2009.

[20] P. Schlüssel, P. Phillips, C. Accadia, and R. Munro, "Post-eps mission requirements document," tech. rep., Eumetsat, June 2010.

[21] J. Randa, J. Lahtinen, A. Camps, A. Gasiewski, M. Hallikainen, D. Le Vine, M. Martin-Neira, J. Piepmeier, P. Rosenkranz, C. Ruf, J. Shiue, and N. Skou, "Recommended terminology for microwave radiometry," tech. rep., National Institute of Standards and Technology, 2008.

[22] J. Randa, "Traceability for microwave remote-sensing radiometry," tech. rep., National Institute of Standards and Technology, 2004.

[23] K. R. Lang, *A Companion to Astronomy and Astrophysics: Chronology and Glossary with Data Tables*. Springer, 2006.

[24] M. Schneebeli and C. Matzler, "A calibration scheme for microwave radiometers using tipping curves and kalman filtering," *Geoscience and Remote Sensing, IEEE Transactions on*, vol. 47, no. 12, pp. 4201–4209, 2009.

[25] M. Janssen, *Atmospheric Remote Sensing by Microwave Radiometry*. Wiley, 1993.

[26] J. Uusitalo, J. Charlton, and J. Lahtinen, "Advanced internal calibration techniques for post eps radiometers," tech. rep., Harp Technologies Ltd, July 2010.

[27] R. Frater and D. Williams, "An active "cold" noise source," *Microwave Theory and Techniques, IEEE Transactions on*, vol. 29, pp. 344 – 347, apr 1981.

[28] E. Weissbrodt, A. Tessmann, M. Schlechtweg, I. Kallfass, and O. Ambacher, "Active load modules for w-band radiometer calibration," in *Geoscience and Remote Sensing Symposium (IGARSS), 2012 IEEE International*, pp. 2945–2948, 2012.

[29] M. Kantanen, E. Weissbrodt, J. Varis, A. Leuther, M. Seelmann-Eggebert, M. Ro?sch, M. Schlecthweg, T. Poutanen, I. Sundberg, M. Kaisti, M. Altti, P. Jukkala, and P. Piironen, "Active cold load mmics for ka-, v-, and w-bands," *Microwaves, Antennas Propagation, IET*, vol. 9, no. 8, pp. 742–747, 2015.

[30] L. Dunleavy, M. Smith, S. Lardizabal, A. Fejzuli, and R. Roeder, "Design and characterization of fet based cold/hot noise sources," in *Microwave Symposium Digest, 1997., IEEE MTT-S International*, vol. 3, pp. 1293 –1296 vol.3, jun 1997.

[31] P. Buhles and S. Lardizabal, "Design and characterization of mmic active cold loads," in *Microwave Symposium Digest., 2000 IEEE MTT-S International*, vol. 1, pp. 29 –32 vol.1, 2000.

[32] W. Ciccognani, F. Giannini, E. Limiti, and P. Longhi, "Analysis, design and measurement of active low-noise terminations," in *Microwave Techniques, 2008. COMITE 2008. 14th Conference on*, pp. 1 –4, april 2008.

[33] N. Skou, S. Sobjaerg, and J. Balling, "Measurements on active cold loads for radiometer calibration," in *Microwave Radiometry and Remote Sensing of the Environment, 2008. MICRORAD 2008*, pp. 1 –4, march 2008.

[34] E. Leynia de la Jarrige, L. Escotte, J. Goutoule, E. Gonneau, and J. Rayssac, "Sige hbt-based active cold load for radiometer calibration," *Microwave and Wireless Components Letters, IEEE*, vol. 20, pp. 238 –240, april 2010.

[35] C. Bredin, D. Sanson, N. Mohamed, J. Orlhac, J. Goutoule, L. Escotte, and P. Piironen, "23.8 ghz and 36.5 ghz active cold loads for radiometer calibration," in *Microwave Technologies and Techniques Workshop*, 2010.

[36] J. Piironen, "personal communication," 2011.

[37] Agilent, "Understanding rf/microwave solid state switches and their applications." Application Note, 2010.

[38] J. Lemmetyinen, J. Uusitalo, J. Kainulainen, K. Rautiainen, N. Fabritius, M. Levander, V. Kangas, H. Greus, J. Pihlflyckt, A. Kontu, S. Kemppainen, A. Colliander, M. Hallikainen, and J. Lahtinen, "Smos calibration subsystem," *Geoscience and Remote Sensing, IEEE Transactions on*, vol. 45, no. 11, pp. 3691–3700, 2007.

[39] A. Colliander, L. Ruokokoski, J. Suomela, K. Veijola, J. Kettunen, V. Kangas, A. Aalto, M. Levander, H. Greus, M. Hallikainen, and J. Lahtinen, "Development and calibration of smos reference radiometer," *Geoscience and Remote Sensing, IEEE Transactions on*, vol. 45, no. 7, pp. 1967–1977, 2007.

[40] B. Lambrigtsen, "Calibration of the airs microwave instruments," *Geoscience and Remote Sensing, IEEE Transactions on*, vol. 41, no. 2, pp. 369–378, 2003.

[41] T. Misra, A. M. Jha, D. Putrevu, J. Rao, D. B. Dave, and S. S. Rana, "Ground calibration of multifrequency scanning microwave radiometer (msmr)," *Geoscience and Remote Sensing, IEEE Transactions on*, vol. 40, no. 2, pp. 504–508, 2002.

[42] E. Njoku, J. M. Stacey, and F. Barath, "The seasat scanning multichannel microwave radiometer (smmr): Instrument description and performance," *Oceanic Engineering, IEEE Journal of*, vol. 5, no. 2, pp. 100–115, 1980.

[43] C. Ruf, S. Keihm, and M. Janssen, "Topex/poseidon microwave radiometer (tmr). i. instrument description and antenna temperature calibration," *Geoscience and Remote Sensing, IEEE Transactions on*, vol. 33, no. 1, pp. 125–137, 1995.

[44] S. Brown, S. Desai, W. Lu, and A. Tanner, "On the long-term stability of microwave radiometers using noise diodes for calibration," *Geoscience and Remote Sensing, IEEE Transactions on*, vol. 45, no. 7, pp. 1908–1920, 2007.

[45] P. Pingree, M. Janssen, J. Oswald, S. Brown, J. Chen, K. Hurst, A. Kitiyakara, F. Maiwald, and S. Smith, "Microwave radiometers from 0.6 to 22 ghz for juno, a polar orbiter around jupiter," in *Aerospace Conference, 2008 IEEE*, pp. 1–15, 2008.

[46] S. Brown, B. Lambrigtsen, R. Denning, T. Gaier, P. Kangaslahti, B. Lim, J. Tanabe, and A. Tanner, "The high-altitude mmic sounding radiometer for the global hawk unmanned aerial vehicle: Instrument description and performance," *Geoscience and Remote Sensing, IEEE Transactions on*, vol. 49, no. 9, pp. 3291–3301, 2011.

[47] I. Corbella, A. Gasiewski, M. Klein, V. Leuski, A. Francavilla, and J. Piepmeier, "Onboard accurate calibration of dual-channel radiometers using internal and external references," *Microwave Theory and Techniques, IEEE Transactions on*, vol. 50, no. 7, pp. 1816–1820, 2002.

[48] A. Tanner, "A high stability ka-band radiometer for tropospheric water vapor measurements," in *Aerospace Conference, 2001, IEEE Proceedings.*, vol. 4, pp. 4/1849–4/1863 vol.4, 2001.

[49] M. Lapinoja, V.-H. Kilpiä, V. Kangas, and P. Jukkala, "Active cold load technology trade-off study," tech. rep., Elektrobit Microwave, July 2005.

[50] D. Sanson and J.-M. Goutoule, "Active calibration for radiometer - final report," tech. rep., EADS Astrium, June 2010.

[51] X. Mei, C. Lin, L. J. Lee, Y. M. Kim, P. H. Liu, M. Lange, A. Cavus, R. To, M. Nishimoto, and R. Lai, "A w-band ingaas/inalas/inp hemt low-noise amplifier mmic with 2.5db noise figure and 19.4 db gain at 94ghz," in *Indium Phosphide and Related Materials, 2008. IPRM 2008. 20th International Conference on*, pp. 1–3, 2008.

[52] K. Elgaid, H. McLelland, C. Stanley, and I. Thayne, "Low noise w-band mmmic amplifier using 50nm inp technology for millimeterwave receivers applications," in *Indium Phosphide and Related Materials, 2005. International Conference on*, pp. 523–525, 2005.

[53] P. Riemer, B. Buhrow, J. Hacker, J. Bergman, B. Brar, B. Gilbert, and E. Daniel, "Low-power w-band cpwg inas/alsb hemt low-noise amplifier," *Microwave and Wireless Components Letters, IEEE*, vol. 16, no. 1, pp. 40–42, 2006.

[54] P. Kangaslahti, B. Lim, T. Gaier, A. Tanner, M. Varonen, L. Samoska, S. Brown, B. Lambrigtsen, S. Reising, J. Tanabe, O. Montes, D. Dawson, and C. Parashare, "Low noise amplifier receivers for millimeter wave atmospheric remote sensing," in *Microwave Symposium Digest (MTT), 2012 IEEE MTT-S International*, pp. 1–3, 2012.

[55] A. Leuther, A. Tessmann, I. Kallfass, R. Losch, M. Seelmann-Eggebert, N. Wadefalk, F. Schafer, J. Gallego Puyol, M. Schlechtweg, M. Mikulla, and O. Ambacher, "Metamorphic hemt technology for low-noise applications," in *Indium Phosphide Related Materials, 2009. IPRM '09. IEEE International Conference on*, pp. 188 –191, May 2009.

[56] A. Leuther, A. Tessmann, I. Kallfass, H. Massler, R. Loesch, M. Schlechtweg, M. Mikulla, and O. Ambacher, "Metamorphic hemt technology for submillimeter-wave mmic applications," in *Indium Phosphide Related Materials (IPRM), 2010 International Conference on*, pp. 1–6, 2010.

[57] A. Leuther, A. Tessmann, H. Massler, R. Losch, M. Schlechtweg, M. Mikulla, and O. Ambacher, "35 nm metamorphic hemt mmic technology," in *Indium Phosphide and Related Materials, 2008. IPRM 2008. 20th International Conference on*, pp. 1 –4, May 2008.

[58] A. Leuther, S. Koch, A. Tessmann, I. Kallfass, T. Merkle, H. Massler, R. Loesch, M. Schlechtweg, S. Saito, and O. Ambacher, "20 nm metamorphic hemt with 660 ghz ft," in *Compound Semiconductor Week (CSW/IPRM), 2011 and 23rd International Conference on Indium Phosphide and Related Materials*, pp. 1–4, 2011.

[59] M. Seelmann-Eggebert, F. Schäfer, A. Leuther, and H. Massler, "A versatile and cryogenic mhemt-model including noise," in *Microwave Symposium Digest (MTT), 2010 IEEE MTT-S International*, pp. 501 –504, may 2010.

[60] E. Leynia de la Jarrige, L. Escotte, E. Gonneau, and J.-M. Goutoule, "Long-term stability of an sige hbt-based active cold load," in *Geoscience and Remote Sensing Symposium (IGARSS), 2011 IEEE International*, pp. 3839 –3842, july 2011.

[61] E. de la Jarrige, L. Escotte, E. Gonneau, and J. Goutoule, "Sige hbt-based active cold load: Design, characterization and stability measurements," in *Noise and Fluctuations (ICNF), 2011 21st International Conference on*, pp. 332 –335, june 2011.

[62] E. de la Jarrige, L. Escotte, E. Gonneau, and J. Goutoule, "Stability analysis of an sige hbt-based active cold load," *Microwave Theory and Techniques, IEEE Transactions on*, vol. 59, pp. 354 –359, feb. 2011.

[63] E. de la Jarrige, *Sources de bruit actives ultra stables a faible temperature de bruit pour la radiometrie micro-onde*. PhD thesis, Universite Paul Sabatier Toulouse III, 2011.

[64] J. Randa, L. Dunleavy, and L. Terrell, "Stability measurements on noise sources," *Instrumentation and Measurement, IEEE Transactions on*, vol. 50, pp. 368 –372, apr 2001.

[65] S. Sobjaerg, N. Skou, and J. Balling, "Measurements on active cold loads for radiometer calibration," *Geoscience and Remote Sensing, IEEE Transactions on*, vol. 47, pp. 3134 –3139, sept. 2009.

[66] V.-H. Kilpiä and P. Jukkala, "Active cold load for radiometer calibration," tech. rep., DA Design Electronics, March 2010.

[67] H.-J. Michel, *Zweitor-Analyse mit Leistungswellen*. B.G. Teubner, 1981.

[68] F. Ellinger, *Radio Frequency Integrated Circuits and Technologies*. Springer-Verlag, 2007.

[69] U. Tietze, C. Schenk, and E. Gamm, *Halbleiter-Schaltungstechnik*. Springer-Verlag, thirteenth ed., 2008.

[70] H. Rothe and W. Dahlke, "Theory of noisy fourpoles," *Proceedings of the IRE*, vol. 44, no. 6, pp. 811–818, 1956.

[71] M. Weatherspoon and L. Dunleavy, "Experimental validation of generalized equations for fet cold noise source design," *Microwave Theory and Techniques, IEEE Transactions on*, vol. 54, pp. 608 – 614, feb. 2006.

[72] D. Wait and G. F. Engen, "Application of radiometry to the accurate measurement of amplifier noise," *Instrumentation and Measurement, IEEE Transactions on*, vol. 40, no. 2, pp. 433–437, 1991.

[73] S. Diebold, E. Weissbrodt, H. Massler, A. Leuther, A. Tessmann, and I. Kallfass, "A w -band monolithic integrated active hot and cold noise source," *Microwave Theory and Techniques, IEEE Transactions on*, vol. 62, pp. 623–630, March 2014.

[74] E. Weissbrodt, M. Schlechtweg, O. Ambacher, and I. Kallfass, "W-band active loads and switching front-end mmics for radiometer calibration," *International Journal of Microwave and Wireless Technologies*, vol. 5, pp. 293–299, 6 2013.

[75] M. Thumm, W. Wiesbeck, and S. Kern, *Hochfrequenzmesstechnik*. B.G. Teubner, 1998.

[76] M. Edwards and J. Sinsky, "A new criterion for linear 2-port stability using a single geometrically derived parameter," *Microwave Theory and Techniques, IEEE Transactions on*, vol. 40, no. 12, pp. 2303–2311, 1992.

[77] I. Kallfass, S. Diebold, H. Massler, S. Koch, M. Seelmann-Eggebert, and A. Leuther, "Multiple-throw millimeter-wave fet switches for frequencies from 60 up to 120 ghz," in *Microwave Conference, 2008. EuMC 2008. 38th European*, pp. 1453–1456, 2008.

[78] E. Weissbrodt, I. Kallfass, and S. Diebold, "Radiometrische kalibrationseinrichtung mit monolithisch integriertem mehrfachschalter." patent, april 2011. 102011016732.

[79] E. Weissbrodt, I. Kallfass, A. Tessmann, H. Massler, A. Leuther, M. Schlechtweg, and O. Ambacher, "A broadband low-noise d-band amplifier module in 35 nm mhemt technology," in *6th ESA Workshop on Millimetre-Wave Technology and Applications*, may 2011.

[80] E. Weissbrodt, A. Hulsmann, A. Massler, H.and Leuther, I. Kallfass, M. Schlechtweg, and O. Ambacher, "Integrated d-band mmics for receiver front-ends," in *Microwave Technology and Techniques Workshop*, pp. 1–6, 2012.

[81] E. Weissbrodt, I. Kallfass, R. Weber, A. Tessmann, H. Massler, and A. Leuther, "Low-noise amplifiers in d-band using 100 nm and 50 nm mhemt technology," in *German Microwave Conference, 2010*, pp. 55–58, 2010.

[82] H. Friis, "Noise figures of radio receivers," *Proceedings of the IRE*, vol. 32, pp. 419 – 422, july 1944.

[83] Agilent, "Fundamentals of rf and microwave noise figure measurements." Application Note 57-1, 2006.

[84] Agilent, "Noise figure measurement accuracy - the y-factor method." Application Note 57-2, 2004.

[85] L. Belostotski, "A calibration method for rf and microwave noise sources," *Microwave Theory and Techniques, IEEE Transactions on*, vol. 59, no. 1, pp. 178–187, 2011.

[86] Agilent, "Practical noise figure measurement and analysis for low-noise amplifier designs." Application Note 1354, 2000.

[87] Agilent, "10 hints for making successful noise figure measurements." Application Note 57-3, 2009.

[88] Elva, "Precision calibrated noise sources." Data Sheet, 2015.

[89] Noisecom, "Precision calibrated millimeter-wave wave guide noise sources." Data Sheet, 2015.

[90] "Answer from semic rf electronic to support request." email, november 2010.

[91] J. L. Cano, E. Villa, D. Ortiz, and E. Artal, "Transición en guía wr-28 de acceso al criostato para la medida de sistemas enfriados," in *Actas del XXIV Simposium Nacional de la Unión Científica Internacional de Radio (URSI 2009)*, sept 2009.

[92] "Cuming microwave technical bulletin 390-1." C-RAM SFC Data Sheet, 2011.

[93] J. Saily and A. V. Raisanen, "Studies on specular and non-specular reflectivities of radar absorbing materials (ram) at submillimetre wavelengths," February 2003.

Patents and Personal Publications

[P-1] **E. Weissbrodt**, I. Kallfass, S. Diebold, "Radiometrische Kalibrationseinrichtung mit monolithisch integriertem Mehrfachschalter," *German Patent*, 102011016732 , April 2011.

[P-2] **E. Weissbrodt**, R. Lenz, W. Wiesbeck, W. Albright, J.Nicoll, "The role of point targets in spaceborne L-Band polarimetric SAR calibration," *EUSAR 2006 - 6th European Conference on Synthetic Aperture Radar*, VDE Verlag GmbH, 2006.

[P-3] **E. Weissbrodt**, I. Kallfass, R. Weber, A. Tessmann, H. Massler, A. Leuther, "Low-noise amplifiers in D-band using 100 nm and 50 nm mHEMT technology," *German Microwave Conference*, pp. 55 – 58, 2010.

[P-4] **E. Weissbrodt**, I. Kallfass, A. Tessmann, H. Massler, A. Leuther, M. Schlechtweg, O. Ambacher, "A Broadband Low-Noise D-Band Amplifier Module in 35 nm mHEMT Technology," *6th ESA Workshop on Millimetre-Wave Technology and Applications*, 2011.

[P-5] **E. Weissbrodt**, I. Kallfass, A. Hulsmann, A. Tessmann, A. Leuther, H. Massler, O. Ambacher, "W-band radiometer system with switching front-end for multi-load calibration," *Geoscience and Remote Sensing Symposium (IGARSS), 2011 IEEE International*, pp. 3843 – 3846, July 2011.

[P-6] **E. Weissbrodt**, A. Hulsmann, H. Massler, A. Leuther, I. Kallfass, M. Schlechtweg, O. Ambacher "Integrated D-Band MMICs for Receiver Front-Ends," in *Microwave Technology and Techniques Workshop*, Mar. 2012, pp. 1 – 6.

[P-7] **E. Weissbrodt**, A. Tessmann, M. Schlechtweg, I. Kallfass, O. Ambacher, "Active load modules for W-band radiometer calibration," *Geoscience and Remote Sensing Symposium (IGARSS), 2012 IEEE International*, pp. 2945 – 2948, 2012.

[P-8] **E. Weissbrodt**, A. Leuther, M. Schlechtweg, I. Kallfass, O. Ambacher, "Highly integrated switching calibration front-end MMIC with active loads for w-band radiometers," in *Microwave Integrated Circuits Conference (EuMIC), 2012 7th European*, 2012, pp. 203 – 206.

[P-9] **E. Weissbrodt**, M. Schlechtweg, O. Ambacher, I. Kallfass, "W-band active loads and switching front-end MMICs for radiometer calibration," *International Journal of Microwave and Wireless Technologies*, vol.5, pp. 293 – 299, 6 2013.

[P-10] R. Weber, V. Hurm, H. Massler, **E. Weissbrodt**, A. Tessmann, A. Leuther, T. Narhi, I. Kallfass, "An H-band low-noise amplifier MMIC in 35 nm metamorphic HEMT technology,"in *Microwave Integrated Circuits Conference (EuMIC), 2012 7th European*, 2012, pp. 187 – 190.

[P-11] A. Hulsmann, A. Tessmann, A. Leuther, I. Kallfass, **E. Weissbrodt**, M. Knelangen, M. Schlechtweg, O. Ambacher, "Integrated circuits beyond 100 GHz for stand-off detection of concealed weapons," in *Fraunhofer VVS Future Security 2010 - 5th Security Research Conference*, 2010, pp. 74 – 77.

[P-12] I. Kallfass, A. Hulsmann, A. Tessmann, A. Leuther, **E. Weissbrodt**, M. Schlechtweg, O. Ambacher, "W-band direct detection radiometers using metamorphic HEMT technology," in *SPIE - The International Society for Optical Engineering: Passive Millimeter-Wave Imaging Technology XIV*, vol. 8022, 2011, pp. 80220O – 80220O-5.

[P-13] S. Diebold, **E. Weissbrodt**, H. Massler, A. Leuther, A. Tessmann, I. Kallfass, "A W-Band Monolithic Integrated Active Hot and Cold Noise Source," *Microwave Theory and Techniques, IEEE Transactions on*, vol. 62, no. 3, pp.623-630, March 2014.

[P-14] M. Kantanen, **E. Weissbrodt**, J. Varis, A. Leuther, M. Seelmann-Eggebert, M. Rösch, M. Schlecthweg, T. Poutanen, I. Sundberg, M. Kaisti, M. Altti, P. Jukkala, P. Piironen "Active Cold Load MMICs for Ka-, V-, and W-Bands," *IET Microwaves, Antennas and Propagation*, vol.9, issue 8, June 2015, pp. 742 – 747.

Acknowledgments

This doctoral thesis is a result of my work as a scientist at the Fraunhofer Institute for Applied Solid-State Physics (IAF) in Freiburg, Germany, where I not only got the support from an excellent scientific and technical staff, but also had access to IAF's worldwide leading III/V semiconductor technology process and its outstanding measurement facilities. Therefore, I would like to thank Professor Dr. Oliver Ambacher, head of the institute and Dr. Michael Schlechtweg, head of the department for High Frequency Devices and Circuits, who gave me this unique opportunity.

I am deeply grateful to my advisor Professor Dr. Ingmar Kallfass, head of the Institute of Robust Power Semiconductor Systems at the University of Stuttgart for his enduring scientific and personal guidance. Moreover, for his confidence in my capabilities from the first day on and his encouragement and unlimited patience throughout the years of this research.

I also want to thank Professor Dr. Gilles Dambrine, deputy director of the Institute of Electronics, Microelectronics and Nanotechnology (IEMN) at the University of Lille, and a distinguished scientist in the field of noise theory, for taking the position of second reviewer.

Furthermore, I would like to acknowledge the basic funding of my general research by the German Federal Ministry of Defence (BMVg) and the Bundeswehr Technical Center for Information Technology and Electronics (WTD 81) and in particular the support by the European Space Agency (ESA) for funding and supporting the very successful *Calload* project. In this context I would like to express my gratitude to my colleague Dr. Matthias Seelmann-Eggebert who acquired this project, introduced me into noise theory and modeling and provided accurate simulation models - as well as to Dr. Petri Piironen, ESA's project coordinator, for his feedback and suggestions for improvement. During the course of the project, I gained valuable knowledge in the field of calibration thru fruitful discussions with the Finnish project partners, namely: Dr. Jussi Varis and Mikko Kantanen from Millilab and Torsti Poutanen from DA-Design. The good atmosphere in the project team and the always constructive cooperation during the project facilitated its success.

As mentioned above, the support of many colleagues facilitated my daily work. Therefore, I want to thank Hermann Massler for sharing his profound measurement experience and Sandrine Wagner and Roger Lozar for supporting my measurement activities. Furthermore, I thank Dr. Arnulf Leuther, in representation of all the staff members of the technology and processing group for providing excellent mHEMT MMICs , Dr. Axel Tessmann for constant consulting in almost every field and always thoroughly reviewing my papers, and Rainer Weber for the constant support in ADS libraries and introduction to LNA design. Moreover, I thank Dr. Beatriz Aja, for sharing her extensive knowledge on radiometer instruments, noise modeling and network analysis, and my fellow (former) PhD students Dr. Daniel Bruch, Dr. Daniel Lopez-Diaz, Daniel Müller, and Dr. Sebastian Diebold for many fruitful discussions. The constant support from the mechanical hardware shop and the IT department was also much appreciated.

For the always good atmosphere in the office and for the continuous motivation special thanks go to Sibylle Hämmerle and to my roommates Dr. Jutta Kühn, Dr. Dirk Schwantuschke, Dr. Robert Makon, and Dr. Vincenzo Carruba.

On many occasions, I had the chance to exchange my recent research progress with experienced scientists in that field, from whom I gained valuable knowledge and got new impulses for my work. For that I am very grateful to:
Professor Dr. Steven C. Reising, professor at the Colorado State University and Dr. Axel Murk from the University of Bern for the feedback to my presented work and discussions on several conferences.
Dr. Frank Schaefer and Sener Türk from the Max-Planck-Institute for Radioastronomy for suggestions concerning the Hot-Cold measurement-setup, low-noise measurements and for feedback on radioastronomy requirements.
Achim Walber and Martin Philipp from Radiometer Physics GmbH for their interest in my work and for the opportunity to cross-check the ACL and AHL module measurements in their laboratories.
Dr. Markus Peichl and Dr. Matthias Jirousek from the National Aeronautics and Space Research Centre (DLR) for their advice on system requirements in passive millimeter wave imaging, security applications, and radiometry in general.
The scientists from the meteorology institute, campus nord, of the Karlsruhe Institute of Technology, for demonstrating their radiometer and calibration procedure.

I also would like to thank my friend Dr. Oliver Pink, who always stands by my side if I need advice - not only limited to scientific questions.
All the necessary energy to stay the course thru the years of research I gained from the people closest to me. Therefore I am deeply grateful to Julia and my whole family, especially to Maria and Waldemar who always support me and believe in me.

Für das Können gibt es nur einen Beweis:
Das Tun.
(Marie von Ebner-Eschenbach)